NASA Technical Memorandum 100046

Characteristics of a Separating Confluent Boundary Layer and the Downstream Wake

D. Adair
W. C. Horne, Ames Research Center, Moffett Field, California

December 1987

National Aeronautics and
Space Administration

Ames Research Center
Moffett Field, California 94035

CHARACTERISTICS OF A SEPARATING CONFLUENT BOUNDARY LAYER AND THE DOWNSTREAM WAKE

D. Adair* and W. C. Horne
Ames Research Center

SUMMARY

Detailed measurements of pressure and velocity characteristics are presented and analyzed for flow over and downstream of a NACA 4412 airfoil equipped with a NACA 4415 single-slotted flap at high angle of attack and close to maximum lift. The flow remained attached over the main element while a large region of recirculating flow occurred over the aft 61% of the flap. The airfoil configuration was tested at a Mach number of 0.09 and a chord Reynolds number of 1.8×10^6 in the NASA Ames Research Center 7- by 10-Foot Wind Tunnel. Measurements of mean and fluctuating velocities were obtained in regions of recirculation and high turbulence intensity using 3-D laser velocimetry. In regions where the flow had a preferred direction and relatively low turbulence intensity, hot-wire anemometry was used. Emphasis was placed on obtaining characteristics in the confluent boundary layer, the region of recirculating flow, and in the downstream wake. Surface pressure measurements were made on the main airfoil, flap, wind tunnel roof and wind tunnel floor. It is thought likely that because the model is large when compared to the wind tunnel cross section, the wind tunnel floor and ceiling interference should be taken into account when the flow field is calculated.

In addition to the presentation of pressure and velocity characteristics, the near-wall results inside the separated region are analyzed as are the relative importance of terms in the momentum and turbulence kinetic energy equations in the confluent separated boundary layer and the recirculating region of the near wake.

---

*NRC Research Associate.

NOMENCLATURE

c	main airfoil reference chord, 0.9 m
C_D	drag coefficient
C_L	lift coefficient (airfoil lift)/$(1/2)\rho U_\infty^2 c$
C_M	moment coefficient, around x/c of 0.25, (moment around quarter chord)/$(1/2)\rho U_\infty^2 c$
C_p	pressure coefficient, $(P - P_\infty)/(1/2)\rho U_\infty^2$
C_f	skin friction coefficient
H	Shape factor, δ^*/θ
n,s	boundary-layer coordinate system over the flap (normal and tangential to local surface)
P	static pressure
R_e	reference chord Reynolds number, $\rho U_\infty c/\mu$
U_∞	reference free-stream velocity
U,W,V	mean velocities (in boundary-layer coordinate system and tunnel coordinates downstream)
$\langle u^2 \rangle$	U-component of turbulence energy
$\langle -uv \rangle$	Reynolds shear stress
$\langle -uw \rangle$	Reynolds shear stress
$u'/U_\infty, v'/U_\infty, w'/U_\infty$	Turbulence intensities
$\langle v^2 \rangle$	V-component of turbulence energy
$\langle w^2 \rangle$	W-component of turbulence energy
$\langle k^2 \rangle$	turbulence kinetic energy
X,Z,Y	wind tunnel coordinate system (horizontal, vertical, spanwise), with origin at the main airfoil leading edge
α	angle of attack, deg

β_p	pressure parameter
δ	boundary-layer thickness
δ_f	flap deflection, deg
δ^*	boundary-layer displacement thickness, $\int_0^\infty (1 - U/Ue)dz$
θ	boundary-layer momentum thickness, $\int_0^\infty (1 - U/Ue)dz$, or flap normal angle to vertical
ρ	fluid density
ν	kinematic viscosity
ν_e	eddy viscosity
γ_{pu}	probability of downstream velocity
$\langle\rangle$	time average or ensemble average

Subscripts

e	edge of boundary layer
∞	reference free-stream quantity

Superscripts

'	perturbation from mean value

I. INTRODUCTION

The multielement wing is essential to generating sufficient lift for modern aircraft during takeoff and landing. The flow around such a configuration, however, is complex, involving significant pressure gradients, nonequilibrium turbulent boundary layers, streamline curvature, and merging asymmetric shear layers. Pressure gradients across the wake are significantly larger than those encountered for single-element airfoils. The presence of a flap amplifies the adverse pressure gradients in the streamwise direction, which affects wake-profile development, turbulent transport, and wake entrainment. It also considerably increases the interaction between viscous and inviscid flows in the vicinity of the flap trailing edge. The severe adverse pressure gradients over the aft portion of multielement airfoil arrangements usually cause rapid thickening of the boundary layer on the flap suction side leading to boundary-layer separation. In addition, the flow field

is complicated by the merging of an airfoil wake with a boundary layer of the downstream element.

Present computational methods can accurately predict the lift (but not drag) of the multielement airfoils at low to moderate angles of attack, providing the flow remains attached. At high angles of attack or when separation occurs, neither lift nor drag can be accurately predicted. An appropriate method for calculating flow over multielement arrangements at high angles of attack has not yet been established. The methods being developed are generally those which solve a Reynolds-averaged form of the Navier-Stokes equations and those which solve potential-flow and boundary-layer equations. For the latter, the main difficulties in prediction have been attributed to inadequacies of boundary-layer approximations, especially in accounting for the cross-stream pressure-gradient term, to deficiencies in turbulence modeling (ref. 1), and to the inability to model strong viscous-inviscid interactions successfully (ref. 2). For a Reynolds-averaged Navier-Stokes approach, two of the major needs are the ability to close the equations with appropriate turbulence model assumptions and the skill to construct computational grids that are compatible with the multielement surface while meeting stringent requirements for smoothness and grid clustering (ref. 3). The calculation of confluent boundary layers is still a problem for both methods, as turbulence models adequate for the analysis of merging shear layers have not as yet proved sufficiently general. As the adverse pressure gradients become more severe, both techniques face the extra complication of separation. In order to contribute to a reduction in the foregoing deficiencies, a comprehensive set of measurements will be presented which will be used to analyze the structure of the flow in strong adverse pressure gradients and in evaluating the accuracy of computational methods.

The present work was preceded by a series of experiments carried out in the NASA Ames 7- by 10-Foot Wind Tunnel. A test of the multielement airfoil arrangement used in this study at a lower angle of attack and with no flow separation is reported in reference 4, and the single-element NACA 4412 airfoil was also tested with trailing-edge separation (ref. 5). Progress has been made elsewhere (refs. 6-8) in the provision of mean and turbulence flow-field data for single-element trailing-edge flows experiencing separation. Similar progress (with the notable exception of ref. 3), however, is not evident for multielement arrangements. In general, data available for multielement airfoils includes static pressure measurements, flap optimization, and mean velocity characteristics (refs. 9,10). Turbulence quantities are not reported to any extent in these studies. Basic studies of a confluent boundary layer and the initial region of boundary-layer separation have been reported in references 11 and 12, respectively.

In the following sections the surface static pressure and detailed flow-field measurements of mean velocity and components of the Reynolds normal and shear stresses of a turbulent flow in the vicinity of an airfoil equipped with a single slotted flap are reported and analyzed. The measurements will focus on the confluent boundary layer over the flap, including the separation region in the vicinity of the flap trailing edge and in the downstream wake. The measurements were made using hot-wire anemometry and a 3-D backscatter laser Doppler anemometer.

II. EXPERIMENTAL ARRANGEMENT

Wind Tunnel

The test was conducted in the 7- by 10-Foot Wind Tunnel at NASA Ames Research Center, Moffett Field, California. The closed-circuit wind tunnel has a working section 4.57 m long a constant height of 2.13 m, and a width which varies linearly from an initial value of 3.05 m to a final value of 3.09 m. There are no turbulence-reducing screens in the wind tunnel circuit, and test section RMS turbulence levels u'/U_∞, v'/U_∞, and w'/U_∞ were equal to 0.0025, 0.0085, and 0.0085, respectively, for the chosen test conditions.

Model

A cross section of the airfoil/flap configuration as installed in the wind tunnel is shown in figure 1. The model comprises a NACA 4412 main airfoil section equipped with a NACA 4415 flap airfoil section. The chord length (c) of the main airfoil is 0.90 m and that of the flap is 0.36 m. The geometric location of the flap relative to the main airfoil was specified by the flap gap (FG), the flap overlap (FO), and the flap deflection (δ_f) as defined in figure 1. For all the velocity characteristics presented in this paper, FG = 0.035 c, FO = 0.028 c, and δ_f = 26.8°. The main airfoil angle of attack (α) was set at a value of 8.2° throughout the experiment, and references to chord length in the following sections will refer to the main airfoil unless otherwise specified. The coordinate system used in the present work is shown in figure 1. Upstream of the flap trailing edge profiles were taken normal to the model surface, whereas in the downstream wake, tunnel coordinates were used. All streamwise distances were referenced to the main airfoil leading edge, and the cross-stream (vertical) origin used for the wake profiles was the flap trailing edge.

The model wind tunnel installation is shown in figure 2. It has a span of 3.05 m and was mounted horizontally in the test section. This slightly limited the optical access of the laser velocimeter in that part of the flow field immediately adjacent to the trailing edge of the flap when compared with a vertically orientated model. An important advantage is achieved with the horizontal arrangement in that optical flare is reduced when one works close to the surface. The intersections between wall and airfoil sections were sealed using felt pads to eliminate leakage between the pressure and suction flows. Boundary-layer trips were mounted on the suction and pressure surfaces of the main airfoil to ensure uniform flow transition across the span at x/c values of 0.025 and 0.10, respectively, from the pressure minimum. A trip was also mounted on the suction side of the flap at an x/c value of 0.01, which was downstream of the flap pressure minimum. Each of the trips had a uniform width of 5.6 mm, a thickness of 0.18 mm, and a sawtooth leading edge.

Surface static pressures were measured at 66 orifices located on the centerline of the main airfoil and at 42 static pressure orifices located on the centerline of the flap. Two additional chordwise rows of 56 orifices each on the main airfoil and

42 orifices each on the flap were located at 0.35-span and at 0.65-span. In addition, a spanwise row of 22 upper-surface orifices was located at the 0.25-chord of the main airfoil and two spanwise rows of 12 upper-surface orifices each were located at the 0.25-chord and 0.85-chord locations on the flap. The static pressure at these 350 orifices was measured using eight 48-port scanivalves equipped with ± 7 kN/m^2 pressure transducers. The transducer voltages were digitized and recorded on magnetic tape with the data reduced to coefficient form. Repeatability in surface pressure data proved to be good at all test conditions, with a maximum change in Cp of 0.6% noted between test runs. Integration of the pressure coefficients produced the section lift and moment coefficients C_L and C_M.

Test Conditions

All of the data presented in this paper are for a Mach number of 0.09, and a chord Reynolds number of 1.8×10^6, corresponding to a tunnel velocity (U_∞) of 30.0 m/sec monitored using a Pitot-static probe located at 1.4 chord lengths upstream of the main airfoil leading edge and 0.61 m from the wind tunnel floor. The test conditions resulted in a steady flow field with an absence of flow separation on with main airfoil but with boundary-layer separation, over the aft 61% of the flap. Extensive probing of the tunnel wall boundary layers was conducted using tufts and surface oil visualization. No evidence of boundary-layer separation could be found in those regions. Streamwise flow fences encircling the main airfoil were installed at 0.175-span and 0.825-span locations to shield the central airfoil section from tunnel wall boundary-layer interference. Studies using tufts and surface oil visualization showed the flow to be two-dimensional over the central 65% of the main airfoil's span. The two-dimensionality of the flow over the airfoil flap was also investigated. Over a stalled airfoil it has been shown (ref. 13) that the flow can depart significantly from two-dimensionality. An effort was made to alleviate this using adjustable flow fences on the flap. The fences, shown in figure 2, extended along 30% of chord length on the upper and lower sides of the flap. It was not possible to use fences which ran the full length of the flap since the laser velocimeter required optical access. The final position occupied by the flow fences were 0.39-span and 0.63-span locations. Two-dimensional flow in the vicinity of the flap trailing edge was found to extend over the center 20% of flap span.

In addition to surface oil and tuft visualization, two-dimensionality of the flow was quantified using pressure and velocity characteristics. Spanwise pressure profiles along the model centerline and at 482 mm to each side of the centerline are shown in figure 3. The agreement between the three rows of measurements is good except over the initial 30% of flap where it is thought the proximity of the flow fences influenced the measurements at the $Y/c = \pm 0.55$ locations. Figure 4(a) presents the spanwise mean velocity at the model centerline upstream of and within the separated region and at two locations downstream of the flap trailing edge. Spanwise velocities can be seen to be generally less than 2% of the free-stream velocity. Shown in figure 4(b) are Reynolds stresses measured in the merging shear

layers upstream of separation and at two locations in the wake, with the Reynolds shear stress seen to be close to zero in all three profiles (fig. 4(c)).

For the mean velocity and turbulence measurements, profiles were made normal to the main airfoil or flap surfaces upstream of the flap trailing edge as described in table 1 and figure 5. In the downstream wake, profiles were made using wind tunnel coordinates. Table 2 presents the orientation of the profiles relative to the vertical, the development of the boundary-layer edge velocity, and the physical thickness of the boundary layers and free shear layers. The edge velocity for stations 1 through 3 is for the boundary layer on the suction side of the main airfoil, and for stations 4 though 21 it is for the upper edge of the main airfoil wake. Up to and including x/c of 0.989, δ is the width of the boundary layer on the main airfoil whereas for $1.003 \leq x/c \leq 1.289$ it represents the distance from the flap surface to the upper edge of the main airfoil wake. Downstream δ represents the total physical distance across the wake.

Instrumentation

Pressure characteristics were obtained using surface static pressure taps as reported in an earlier section. A sting-mounted Pitot-static tube with an outside diameter of 6.35 mm was used to obtain pressure measurements in the tunnel floor and roof boundary layers, respectively. Vertical surveys using the Pitot-static tube were made at the mid-span location in the plane of the reference Pitot-static probe and at 1.5 chord lengths downstream of the flap trailing edge.

Upstream of separation in the region of merging shear layers and for most of the wake, the flow had a preferred direction and comparatively low turbulence intensities. For these reasons it was possible to quantify the velocity characteristics with stationary hot-wire anemometry. The sensors were first orientated to measure U, W, u', w', and $\langle -uw \rangle$, and then to obtain V, v', and $\langle -uv \rangle$, where U, W, and V indicate streamwise, cross-stream and spanwise velocities, respectively. Straight-wire (DISA 55P10) and cross-wire (DISA 55P64) probes were operated with constant-temperature anemometers (DISA 55M10), and the instantaneous voltages were recorded digitally using an HP 1000 computer prior to analysis. The wires were operated at an overheat ratio of 1.8 and amplifiers were used in the processing of the signal. The bandwidth of the data-acquisition system was 20 kHz. The nonlinearized signals were sampled simultaneously at a rate of 10 samples/sec over a minimum period of 100 sec. Calibration for both flow velocity and flow angle was performed using a DISA hot-wire calibration rig, with the resulting linearizations stored in the computer.

In regions of reversed flow and high turbulence intensity, a 3-D laser velocimeter (LV) as described by references 14 and 15 was used. A schematic of the LV system is shown in figure 6 and its position in relation to the model is shown in figure 7. The LV was used to measure the mean velocities U, W, and V and the turbulence quantities u', w', and $\langle -uw \rangle$. The system is capable of measuring all three velocity components (U,W,V) simultaneously by means of three independent dual-beam channels that operate in backscatter mode. To improve the sampling rate the

method of coupling the three channels as reported in reference 14 was modified. The colors violet (476.5 nm) and green (514.5 nm) of an 8-W argon-ion laser were coupled to obtain samples of streamwise and cross-stream components of the mean velocity and the components of the stress tensor. This was followed by a second sample using the blue (488.0 nm) and green colors to obtain the spanwise mean velocity. Vertical and streamwise motions of the focal volume were accomplished by moving the entire LV on a digitally controlled platform. The repeatable positioning of the focal volume was better than 0.5 mm. The support platform was slightly yawed by 2° with respect to tunnel coordinates, and was pitched downwards by 2.75° to allow grazing contact of the focal volume at the semi-span of the wing. The small pitch and yaw angles of the optical table result in slight coupling of all three velocity components. Neglecting the spanwise coupling component led to an estimated decrease in U, W, u', and w' of 0.6%, 0.54%, 1.1%, and 0.92%, respectively.

An inherently poor signal-to-noise ratio is common to LVs using backscatter. To alleviate the problem it is desirable to minimize the processing bandwidth. However, this can lead to biasing of the incoming data. The present LV incorporates programmable frequency synthesizers that generate mixing frequencies for each channel that can be varied under program control to maintain the mean signal frequency at the center of the bandwidth. Frequency shifting by Bragg cells was employed to resolve directional ambiguity in the measured velocities.

The laser was operated at a power of between 1.75 and 2 W and the effective probe volume length for each channel was found to be 5 mm for the green and violet beams and 2.5 mm for the blue. Each beam had a waist diameter of 0.3 mm. A mineral oil aerosol with a nominal particle diameter of 5 μm was introduced into the diffuser of the wind tunnel to provide nearly uniform seeding in the test section. In general, 1000 samples were taken at each measurement point, although this was increased in difficult areas of the flow.

Comparison was made between the hot-wire and LV measuring techniques by comparing mean velocity and turbulence characteristics at two streamwise locations, $x/c = 1.084$ (over the flap) and 1.539 (in the downstream wake). Both locations had regions of intermittent backflow present which affected the hot-wire signal. At $x/c = 1.084$ intermittent boundary layer separation was present close to the surface while at $x/c = 1.539$ in the wake some backflow occurred in the inner layer. Good agreement was found between the two measuring techniques in the regions where backflow was not present (fig. 8). The agreement between the two measurement techniques is poor for $n/\delta < 0.2$ for the profile over the flap and for $0.15 > Z/\delta > -0.2$ for the station in the wake where rectification of the hot-wire signal is evident.

III. EXPERIMENTAL RESULTS

The pressure and velocity measurements are presented below for flow both on and downstream of the flap. The results presented in this section were obtained on the centerline of the tunnel. Particular attention is paid to the regions of the

boundary-layer separation, merging shear layers, recirculating flow, and the downstream wake.

Mean Flow Results—Pressure

Static pressure measured over the main airfoil and flap surfaces at mid-span are presented in figures 9 and 10. Distributions are shown for a range of geometries obtained by varying the flap deflection angle and flap gap. Flap overlap was held at a constant 0.028 c for all settings. For the case of δ_f of 26.8° and flap gap of 0.035 c (fig. 9), the existence of separation on the upper flap surface is recognized by the appearance of a constant pressure region extending over 61% of flap chord length. A localized increase in the flap suction is noted at 20% of flap chord, i.e., just downstream of the main airfoil trailing edge. This increase occurred for all the flap settings and was more pronounced when the flap gap was decreased.

The location of the flap boundary-layer separation could be controlled by both the flap deflection and gap width. Taking the conditions of figure 9 as a baseline, a 5° reduction of flap deflection moved the separation point downstream (fig. 10(a)). The separated region then occupied only the aft 7% of flap chord. Increasing the flap deflection by 5° caused the separation to extend over 70% of the flap chord (fig. 10(b)). The effect of flap gap is shown on figure 10(c). By reducing the gap to 0.015 c and with $\delta_f = 26.8°$, the separation was reduced to 30% of the flap chord. Integration of the pressure coefficients produced the section force and moment coefficients C_L and C_M for the six model settings, the uncorrected results of which are shown in figure 11. Maximum lift coefficient for α equal to 8.2° is seen to be bounded by the results, but to locate the exact $C_{L_{max}}$ much finer adjustments of δ_f and FG would be required. The values of C_L and C_M are comparable in magnitude to those reported in references 3 and 16. The drag coefficient, C_D, was estimated to be 0.073 for the settings $\delta_f = 26.8°$, FO = 0.035 c, and FG = 0.028 c. It was estimated by integrating the measured velocity defect 0.5 chord length downstream of the flap trailing edge.

Wind Tunnel Wall Interaction

Static pressure measurements were made along the tunnel centerline close to the roof and floor of the test section. These measurements are shown in figure 12 and are for the case $\delta_f = 26.8°$, FG = 0.035 c, and FO = 0.028 c. The pressure signature on the tunnel walls extended upstream to the plane of the reference Pitot-static probe and downstream into the diffuser. Velocity profiles in the roof and floor boundary layers at the centerline of the tunnel in the plane of the flap trailing edge were obtained to give an indication of the displacement effect of the tunnel wall boundary layers. For the roof boundary layer, δ, δ^*, and θ were found to be 132 mm, 16 mm, and 13 mm, respectively, and for the floor the same quantities were 146 mm, 18 mm, and 14 mm, respectively. Also presented in figure 12 are static pressure measurements taken along vertical traverses. These tranverses were located

at 1.4 chord lengths upstream of the main airfoil leading edge and at 1.5 chord lengths downstream of the flap trailing edge. Total pressure was found to be a constant 601 N/m^2 in the plane of the reference Pitot-static tube. Flow angularity, measured using a five-tube Pitot probe proved to be within ±0.2° from the horizontal.

To characterize the effect of tunnel wall interference, calculations with and without tunnel walls were made using the method of reference 17. At the flap deflection angle of 21.8°, when no extensive flow separation occurred, C_L and C_M were estimated to be decreased by 7% and increased by 4.5%, respectively, when no walls were present. The correction for C_L is in close agreement to that found the method for two-dimensional boundary corrections found in reference 18 was used. For the present arrangement, with $\delta_f = 26.8°$, the method of reference 17 was not appropriate for correcting lift and pitching moment because of the presence of extensive boundary-layer separation. Thus, because the wall interference effects are expected to be significant and because it is not possible to correct the data reliably for their effects, it is recommended that account should be taken of the presence of wall interference when calculating this flow.

Mean Flow Results—Velocity

The following mean velocity results are for the flap setting $\delta_f = 26.8°$, FO = 0.035 c, and FG = 0.028 c. The characteristic boundaries and general organization of the flow domains are shown in figure 13 where γ_{pu} is the fraction of LV samples having a positive value of streamwise velocity, U. Evidence of boundary-layer separation was first noted 228 mm upstream of the flap trailing edge, where a region of intermittent separation, over 4% of flap chord in length, occurred just upstream of boundary-layer detachment. This confirms earlier observations in oil and tuft studies of the location of boundary-layer separation. A region of intermittent backflow is seen to envelop the recirculating flow, and negative flow was found to persist to about 180 mm beyond the trailing edge. The maximum height of the fully reversed region was found to be 148 mm normal to the flap surface.

The mean velocity vectors are plotted in figure 14(a); the backflow was relatively strong compared to previous studies (refs. 6,8,12). Close to the top of the recirculating flow, a thin strip of almost zero velocity existed. Profiles downstream of the flap indicate the flow developed into an asymmetric wake. The mean flow streamlines in the region of the flap and in the near wake are shown in figure 14(b). The negative mean velocity region is bounded by the zero streamline. In common with the flows of reference 8, the present boundary layer separated under the action of adverse pressure gradients with convex curvature present. The curvature of the streamlines was less than that of the surface. This gave a streamline pattern different from that of reference 12, in which streamlines show more curvature near mean streamline detachment when separation was caused by adverse pressure gradient with no surface curvature present.

Integral parameters for flow in the vicinity of the flap trailing edge are shown in figure 15. Up to the flap trailing edge, these parameters were obtained by

integrating the velocity profiles from the flap surface in a direction normal to the local surface. The integration was terminated at the upper edge of the main airfoil wake. For locations downstream of the trailing edge, the integration was carried out across the entire wake in a vertical direction. The values of the integral quantities are of limited use in that the terms in the cross-stream momentum equation are important in this region and the main airfoil wake has merged with the flap suction-side boundary layer. Large values of δ^* and θ were found in the vicinity of the flap trailing edge, with the maximum found 8% upstream of the flap trailing edge.

Integration of velocity profiles was also performed for the inner flap boundary layer. Just upstream of separation the flap boundary layer was found to grow rapidly before merging with the main airfoil wake. At 36% of flap chord, where intermittent separation was known to occur, the values of δ^* and θ found by integrating across this inner boundary layer were 4.95 mm and 1.60 mm, respectively. This gave a shape factor H of 3.09.

The skin friction coefficient distributions near the wing trailing edge and on the flap upper surface are shown in figure 16. The skin friction was obtained from Clauser plots. Figure 16(b) indicates mean streamline detachment at 39% of the flap chord ($C_f = 0.0$). This is in agreement with the static pressure measurements and flow visualization.

Profiles of streamwise mean velocity are shown in figure 17 for all 21 stations of table 1. The profiles over the main airfoil are consistent with those of a boundary layer in an adverse pressure gradient. Just downstream of the main airfoil trailing edge, the turbulent boundary layer on the flap was found to be extremely thin. At survey station No. 6, the wake of the main airfoil and boundary layer on the upper side of the flap were beginning to merge. By station No. 7 only a remnant of the strong inviscid jet through the slot between main airfoil and flap remained. Backflow, which was first noted close to the surface at station No. 6, strengthened under the influence of the streamwise adverse pressure gradient, to an observed maximum value of 14% of the upper edge velocity at station No. 7. This very strong backflow was also found downstream at stations No. 8 and 9. The strongest recirculating flow was noted at station No. 10, where its value reached 28% of the upper edge velocity. This is a much stronger backflow than has been reported previously for trailing-edge flows and indicates the presence of severe adverse pressure gradients.

Closure of the wake around the downstream end of the separation bubble occurred because of the interaction of the energetic lower pressure side flow with the separated shear layer on the suction side. No evidence of a double wake was found downstream of the flap trailing edge, showing the main airfoil wake to have fully merged with the flap wake ahead of this location. The pressure side boundary layer had a thickness of 13.5 mm at the trailing edge of the flap. It had a small logarithmic region which gave a C_f value of 0.004. Values of δ^* and θ for the pressure side boundary layer at the flap trailing edge were found to be 2.53 mm and 1.82 mm. Downstream of the flap trailing edge the wake was seen to be asymmetric and up to about $x/c = 0.8$ the pressure and suction edge velocities were unequal.

Further downstream the velocity defect gradually decreased and the shap factor asymptotically approached 1.0.

The mean streamwise velocities in the near-wall region of the attached boundary layer and reversed-flow regions were examined. The conventional law-of-the-wall was found to adequately represent the near-wall flow until just before intermittent separation. After separation there does not appear to be a log-linear region as shown in figure 18.

The cross-stream velocity at the 21 stations is presented in figure 19. Generally its value over the main airfoil and initial flap surfaces intended to zero. At station No. 6, close to intermittent separation, flow towards the flap surface of 20% of edge velocity was noted near the surface. Strong variations in cross-stream velocity were found in the wake close to the flap trailing edge and in the vicinity of recirculating flow. For example, at stations No. 12 and 16 cross-stream velocities of up to 30% of free-stream velocity are evident, showing the presence of large cross-stream pressure gradients. This variation tends to diminish with streamwise distance until an almost constant cross-stream velocity profile is noted at x/c of 2.789 (station No. 21).

The LV gave information on the probability of downstream flow, γ_{pu} in the vicinity of separation. As shown in figure 20, intermittent reversed flow started at 35% (station No. 6) of flap chord and the γ_{pu} values decreased with downstream distance. Also, with downstream distance the instantaneous flow reversals gradually spread cross-stream from the flap surface. In the near wake, it can be seen that γ_{pu} of less than 1 was still found at x/c of 0.25 (station No. 16) downstream of the flap trailing edge. γ_{pu} was never found to be zero, indicating no constant, fully reversed flow in any part of the recirculating region, but values as low as 0.02 were found in the vicinity of the flap trailing edge. This is a lower value than was found for stalled, single-element airfoils. At the trailing edge, instantaneous flow reversals were observed to occur over the inner 42% of the boundary layer, whereas the average mean flow was negative for only 28% of the boundary layer thickness.

Turbulence Results

The development of Reynolds stresses over the main airfoil and flap suction surfaces and in the downstream wakes are shown in figures 21-23. Comparison of the data obtained at station No. 3 with that obtained at station No. 4 in figures 21 and 22 shows that, initially, there was a significant change in the level of turbulence energy near the centerline of the wake as the boundary layer on the upper surface of the wing moved into the near wake and streamwise normal stresses locally increased by 50%. A downstream increase of some 2.6 times in the peak cross-stream normal stresses, as shown by profiles at stations No. 5 and 6 in figure 22, was noted as the shear layer entered a region of increasing adverse pressure gradient, whereas the peak streamwise normal stresses increased only slightly. In the initial regions of jet flow, between the main airfoil and flap, the turbulence was

remarkably low. Up to and including station No. 6, the flap boundary layer either cannot be detected or was extremely thin.

The Reynolds shear stress profile (fig. 23) just downstream of the trailing edge of the main element (station No. 4) shows a four-fold increase in peak value compared to the profile at station No. 3. The measured positive peak value of $\langle -uw \rangle / U_e^2$ was 0.012 for the wake of the main airfoil compared to the 0.005 reported in reference 4. The negative peak was only about 50% of the value reported in reference 4 at this location. A decline in the Reynolds shear stress is noted near the wall in the wake of the main airfoil in the region of merging shear layers as shown by profiles No. 4-6, and the shear stress goes through zero at station No. 6, further confirming earlier observations that separation first occurs close to this location.

At station No. 7 the flap boundary layer has fully separated and an abrupt change is noted in figures 21 and 22 in the near-wall Reynolds normal stress profiles. This is consistent with the rapid growth of the separated boundary layer and the disappearance of the low-turbulence jet flow. Downstream of station No. 7 the distributions of streamwise Reynolds normal stresses in the flap suction-side boundary layer show the well accepted trends of those in strong adverse pressure gradients, i.e., increasing turbulent stresses with maximum stress points moving away from the walls with streamwise distance. The cross-stream Reynolds normal stress profiles followed this trend in the initial region of the separated boundary layer, but for $1.220 \leq x/c \leq 1.289$ the increase in peak value and movement away from the wall was minimal and the profiles showed similarity except close to the flap surface. Over the region $1.129 \leq x/c \leq 1.289$ (stations No. 7-11) the maximum values of streamwise and cross-stream Reynolds normal stresses increased by two and four times respectively because of extra turbulence production and destabilizing curvature. The value of the cross-stream Reynolds normal stresses are generally 40% of the streamwise Reynolds normal stresses in the flap trailing-edge region. It is interesting to note within the recirculating flow and close to the flap surface the appearance of a second maximum in the streamwise normal stress profiles and some of the cross-stream Reynolds normal stress profiles. This may be due to the presence of a thin but fairly strong reversed boundary layer close to the model surface. No suppression of turbulence in the outer part of the separated boundary layer was indicated by the Reynolds normal stress profiles, and in fact increased turbulence activity in this outer region was noted in profiles No. 10 and 11, causing an equivalent increase in Reynolds shear stress. Both cross-stream and streamwise normal stresses peaked at about the same location in the layer, and the cross-stream Reynolds normal stresses show broad maxima, especially in the vicinity of the flap trailing edge, indicating that turbulent diffusion plays an important role here.

Inside the separated region, the Reynolds shear stress gradually develops a double maxima, one close to the surface and the other moving slowly away from the surface with downstream distance. Both positive and negative maxima increase streamwise, and the locations of the Reynolds shear stress zero values seem to correspond to that of the minimum in the mean velocity distributions.

In the region just downstream of the flap trailing edge (stations No. 12-16), the Reynolds normal and shear stresses exhibit rapid changes near the wake centerline while changes are gradual towards the outside of the shear layer. It is interesting to note the remnant of the near-wall normal stress peak persisting into the wake at station No. 12. The profiles show double maxima in the initial Reynolds normal stress profiles until the end of the recirculating flow region, where the cross-stream Reynolds normal stresses became single peaked. As found by previous investigations (refs. 6,19), the streamwise Reynolds normal stresses were slower to decay and it was not until about x/c of 2.039 that the mixing process smooths out the smaller pressure-side peak and a single maximum occurred. Generally, in the near wake the turbulence energy in the pressure-side shear layer increased, whereas on the suction-side layer it remained fairly constant. In the wake (up to x/c of 1.789), the streamwise turbulence intensities showed only small variations with streamwise direction, whereas the cross-stream turbulence intensities showed peaks which both increased in magnitude and spread across the layer, showing turbulent diffusion to be dominant as opposed to stabilizing curvature. On the suction side (up to x/c of 1.427), the streamwise turbulence intensity slightly decayed, whereas the cross-stream turbulence intensity peak remained fairly constant and spread across the shear layer, again showing turbulent diffusion to be present. The location of minimum turbulence intensity in the near wake did not coincide with that of the minimum velocity, indicating a departure from equilibrium.

Downstream of the recirculating flow region, the present results are consistent with the measurements of references 19 and 20 and indicate that $\langle u^2 \rangle / U_\infty^2 > \langle v^2 \rangle / U_\infty^2 > \langle w^2 \rangle / U_\infty^2$. Two chord lengths downstream of the main element's trailing edge the turbulence was found to be essentially isotropic.

In the near wake, the Reynolds shear stress remained fairly constant in the suction-side shear layer, even under the combined influence of adverse pressure gradient and destabilizing streamline curvature. There was a slight increase in its value in the vicinity of intermittent backflow and slightly beyond at about x/c of 1.539 (station No. 16), after which there was a gradual decay. The Reynolds shear stress in the pressure-side shear layer exhibited rapid growth just downstream of the flap trailing edge, then remained constant up to about x/c of 1.539, after which a gradual decay was noted.

IV. DISCUSSION

The flow just described is now discussed with an emphasis on the relative importance of the terms in the momentum and turbulence kinetic energy equations in the confluent boundary layer and the recirculation region of the near wake. Implications for calculation methods will also be discussed.

The calculation of the start of separation in any computational method is important. One question to be addressed is whether standard criteria for the prediction of the onset of separation can be used for the thin boundary layer on the

surface of the flap or does the presence of the initially inviscid and later low turbulence jet, and the main airfoil wake affect these criteria. The simple relationship given by reference 21 where

$$H = 1 + (1 - \delta^*/\delta_{0.995})^{-1} \tag{1}$$

was tested as a necessary criteria just upstream of intermittent separation. The measured shape factor showed a discrepancy of 12% when compared to that found by the above equation. Other proposals involve the use of the pressure gradient to predict separation. For example, reference 22 requires that the parameter $\beta_p > 0.004$ where

$$\beta_p = \frac{\theta}{\rho U_e^2} \frac{dP}{dx} \tag{2}$$

Using this criteria, separation was predicted at 34% of flap chord, slightly upstream of known intermittent separation. Because the flow is rapidly changing in this region, the above two results seem to indicate that standard methods of predicting separation can be accurate provided the main airfoil wake has not fully merged with the flap boundary layer.

Downstream of intermittent separation, reference 12 shows the existence of similarity in γ_{pu} distributions by normalizing and plotting $(\gamma_{pu} - \gamma_{pu_{min}})/(1 - \gamma_{pu_{min}})$ vs. n/D where D is the distance of the peak in the u' distribution from the wall. The present data were compared to a curve which approximately satisfied their data (fig. 24). Similarity can be seen in the present profiles, but at a different location to that previously found. This may be primarily due to the change in location of the maxima in the u' distribution by the presence of curvature and/or the contribution to the turbulence field by the main element wake. Similar plots drawn with D being taken as the distance from the wall to the location where peaks are observed in the w' and $\langle -uw \rangle$ distributions show similar results.

The momentum and energy balance equations were examined in light of the experimental measurements. The locations examined included regions in the separated flow, one in the separated boundary layer and the other downstream in the recirculating flow of the near wake. The momentum equations in two dimensions are

$$\begin{aligned} U \frac{\partial U}{\partial x} + W \frac{\partial U}{\partial z} &= -\frac{1}{\rho} \frac{\partial P}{\partial x} + \frac{\partial \langle -uw \rangle}{\partial z} - \frac{\partial \langle u^2 \rangle}{\partial x} \\ U \frac{\partial W}{\partial x} + W \frac{\partial W}{\partial z} &= -\frac{1}{\rho} \frac{\partial P}{\partial z} + \frac{\partial \langle -uw \rangle}{\partial x} - \frac{\partial \langle w^2 \rangle}{\partial z} \end{aligned} \tag{3}$$

with the terms on the left-hand side being inertia or convective terms and those on the right-hand side being pressure gradient, the Reynolds shearing-stress gradient, and the Reynolds normal-stress gradient, respectively. For both momentum equations the viscous terms were neglected as they proved to be much smaller than the above

terms, and the symbols used for each of the terms in figures 25-27 are shown in table 3.

The cross-stream pressure gradient, as shown in figure 25(b) is important in the vicinity of the trailing edge when it is compared to the corresponding streamwise pressure gradient (fig. 25(a)). Both terms are generally an order of magnitude larger than those reported for single-element airfoils (refs. 6-8). This suggests that the interaction between the viscous separated boundary layer and the inviscid flow above was strong and that the possibility of successfully applying simple approximations for $\partial P/\partial y$ in the boundary layer equations is remote. Just in front of the trailing edge and in the region of separated flow, over the inner 35% of the layer, the shear and normal stress components became dominant and tended to balance the pressure term with convection tending to zero. In the outer region of the layer, convection became the dominant term. In the recirculating flow of the downstream wake, also shown in figure 26, the shear normal stress gradient terms were again dominant and balanced the streamwise pressure gradient.

For the normal momentum equation, the terms of which are shown in figures 25(b) and 26(b), the pressure gradient was large and exhibited a large variation across the layer. The Reynolds normal stress term played a large role in the recirculating flow close to the flap wall, as also found by reference 12, and the shear term was less prominent. Around the periphery of the recirculation region, the important quantity was found to be the normal stress term and, to a lesser extent, the convection term.

The turbulence energy equation is

$$\frac{U}{2}\frac{\partial \langle k^2 \rangle}{\partial x} + \frac{W}{2}\frac{\partial \langle k^2 \rangle}{\partial z} = -\frac{\partial}{\partial z}\nu\left(\frac{P}{\rho} + \frac{k^2}{2}\right) - \langle uw \rangle \frac{\partial U}{\partial z} - (\langle u^2 \rangle - \langle w^2 \rangle)\frac{\partial U}{\partial x} + \varepsilon \qquad (4)$$

where the terms on the left-hand side are advection and on the right-hand side are turbulent diffusion, turbulent-shear-stress production turbulent-normal-stress foundation, and dissipation, respectively. The turbulence energy equation components for the present flow are shown for flow over the flap surface in the vicinity of the trailing edge and in the downstream near wake. Dissipation was not measured and appears in the imbalance of figure 27. In the region of recirculating flow over the surface, all three terms—advection, shear production, and normal stress production—show large variations in the lower 50% of the layer. This would indicate that turbulence energy reaches the backflow region by a combination of turbulence diffusion and, to a lesser extent, by convection. In the downstream wake the shear production term is dominant in the backflow region, whereas normal stress production is evident in the pressure side shear layer. In the upper suction-side layer, advection and shear production are the dominant terms.

The distribution of the shear stress correlation coefficient is shown in figure 28 at several x/c locations. The correlation coefficient is a measure of the extent of the relationship between the instantaneous u' and w' fluctuations. Some similarity was found in the profiles, especially close to the flap trailing edge. Values found in the outer region of the layer were comparable to those found in the

fully separated boundary layer of reference 12. High negative correlation was noted close to the model surface.

Eddy viscosity distributions are shown in figure 29 for five locations in the separated boundary layer; one with intermittent flow reversal present and the others in the separated boundary layer. The minimum noted in the profile at x/c of 1.084 is due to the presence of the low-turbulence jet, and in the separated region ν_e was defined everywhere except where $\partial U/\partial n = 0$. Some similarity was noted in the profiles except in those close to the flap wall. In the outer layer ($n/\delta > 0.4$), the present results show good agreement with those of reference 22, which were measured in adverse pressure gradient equilibrium boundary layers (especially for the flow denoted by the similarity exponent $a = -0.15$). The regression function describing the flow labeled as $a = -0.225$ could be thought of as the upper boundary for the present results. The eddy viscosity derived from the measurements in the present flow are high compared with reference 12, which reported ν_e to be driven down in the presence of separation. The profile at x/c of 1.084 shows good agreement in the inner region of the boundary layer compared with profiles measured in reference 23 and with the eddy viscosity model proposed in reference 24. For profiles downstream, however, eddy viscosity models are physically meaningless near the wall as the value tends to infinity.

The Prandtl mixing length does not seem to be helpful inside the recirculating region as its use requires taking the square root of a negative term. However, if the modulus of this term was used, similar remarks can be made about the mixing-length profiles as were made for the eddy viscosity inside the separated boundary layer.

V. CONCLUDING REMARKS

Measurements of the mean values of pressure and velocity have been presented for the flow over and in the downstream wake of a single-slotted airfoil/flap combination. The results indicate rapid growth of the boundary layer in the vicinity of the separation. The mean velocity profiles in the near-wall region agree with the logarithmic law-of-the-wall in the region approaching separation, but not in the recirculating region. In the vicinity of separation, there is a notable increase in the Reynolds shear stress. The distributions of Reynolds stresses are complex in the very near wake and are affected by streamline curvature and the presence of a significant layer of turbulence. In the vicinity of the trailing edge, the turbulence field is dominated by shear layers encompassing the separated region. The cross-stream gradient is important in the vicinity of the flap trailing edge and simple approximations for the cross-stream momentum equation do not seem possible. Simple turbulence models are not helpful within the recirculating flow region.

It should be noted that the model was relatively large when compared to the wind tunnel cross section. Thus, it is recommended that the effects of wind tunnel wall interference be included when the flow field is calculated.

REFERENCES

1. Spaid, F. W.; and Hakkinen, R. J.: On the Boundary Layer Displacement Effect Near the Trailing-Edge of an Aft-Loaded Aerofoil. J. Appl. Math. Phys., vol. 28, 1977, p. 941.

2. Melnik, R. E.; and Grossman, B.: On the Turbulent Viscous-Inviscid Interaction at a Wedge Shaped Trailing-Edge. Symposium on Numerical and Physical Aspects of Aerodynamic Flows, Springer Verlag, 1981.

3. Braden, J. A.; Whipkey, R. R.; Jones, G. S.; and Lilley, D. E.: Experimental Study of the Separating Confluent Boundary-Layer. NASA CR-3655, 1983.

4. Olson, L. E.; and Orloff, K. L.: On the Structure of Turbulent Wakes and Merging Shear Layers of Multielement Airfoils. AIAA Paper 81-1238, June 1981.

5. Wadcock, A. J.: Investigation of Low-Speed Turbulent Separated Flow Around Airfoils. NASA CR 177450, 1987.

6. Nakayama, A.: Measurements of Attached and Separated Turbulent Flows in the Trailing-Edge Regions of Airfoils. Second Symposium at the Calif. State Univ., Long Beach, Jan. 1983.

7. Young, W. H.; Meyers, J. F.; and Hoad, D. R.: A Laser Velocimeter Flow Survey above a Stalled Wing. NASA TP 1266, 1978.

8. Adair, D.: Characteristics of a Trailing Flap Flow with Small Separation. Expts. in Fluids, vol. 5, 1987, pp. 114-128.

9. Foster, D. N.; Irwin, H. P.; and Williams, B. R.: The Two Dimensional Flow Around a Slotted Flap. RAE Tech Report 70164, Royal Aircraft Establishment, Farnborough, England, Sept. 1970.

10. Olson, L. E.; McGowan, P. R.; and Guest, C. J.: Leading-Edge Slat Optimization for Maximum Airfoil Lift. NASA TM 78566, 1979.

11. Pot, P. J.: Measurements in a 2-D Wake and in a 2-D Wake Merging into a Boundary Layer. NLR Report TR-79063U, National Aerospace Laboratory, The Netherlands, 1979.

12. Simpson, R. L.; Chew, Y. T.; and Shivaprasad, B. G.: The Structure of a Separating Boundary Layer, Parts 1-3. J. Fluid Mech., vol. 113, 1981, pp. 23-90.

13. Winklemann, A. E.: Flow Field Surveys of Separated Flow on a Rectangular Planform Wing. AIAA 19th Aerospace Sciences Meeting, St. Louis, MO, Jan. 1981.

14. Orloff, K. L.; Snyder, P. K.; and Reinath, M.S.: Laser Velocimetry in the Low-Speed Wind Tunnels at Ames Research Center. NASA TM 85885, 1984.

15. Snyder, P. K.; Orloff, K. L.; and Reinath, M. S.: Reduction of Flow-Measurements Uncertainties in Laser Velocimeters with Nonorthogonal Channels. AIAA J., vol. 22, no. 8, 1984, pp. 1115-1124.

16. Ljungstrom, B.: Wind Tunnel High Lift Optimization of a Multiple Element Airfoil. FFA Tech. Note AU-778, The Aeronautical Research Institute of Sweden, 1976.

17. Maskew, B.: Program VSAERO, A Computer Program for Calculating the Nonlinear Aerodynamic Characteristics of Arbitrary Configurations. NASA CR-166476, 1982.

18. Rae, W. H.; and Pope, A.: Low-Speed Wind Tunnel Testing. Wiley, 1984.

19. Hah, C.; and Lakshminarayana, B: Measurement and Prediction of Mean Velocity and Turbulence Structure in the Near Wake of an Airfoil. J. Fluid Mech., vol. 115, 1982, pp. 251-282.

20. Chevray, R.; and Kovasznay, L. S. G.: Turbulence Measurements in the Wake of a Thin Flat Plate. AIAA J., vol. 7, no. 8, 1969, pp. 1641-1643.

21. Sandborn, V. A.; and Kline, S. J.: Flow Models in Boundary-Layer Stall Inception. ASME (J. Basic Eng.), vol. 83, no. 3, 1961, pp. 317-327.

22. Alber, I. E.: Similar Solutions of a Family of Separated Turbulent Boundary Layers. AIAA Paper 71-203, Jan. 1971.

23. Bradshaw, P.: The Turbulence Structure of Equilibrium Boundary Layers. J. Fluid Mech., vol. 29, no. 4, 1967, pp. 625-645.

24. Cebeci, T.; and Smith, A. M. O.: Momentum Transfer in Boundary Layers. Hemisphere, 1974.

TABLE 1.- LOCATION AND ORIENTATION OF SHEAR-LAYER MEASURING STATIONS

Station no.	x/c	Type of shear layer	Orientation of survey line
1	0.495	Boundary layer	Normal to airfoil surface
2	0.742	Boundary layer	Normal to airfoil surface
3	0.989	Boundary layer	Normal to airfoil surface
4	1.003	Wake	Normal to flap surface
5	1.038	Wake and boundary layer	Normal to flap surface
6	1.084	Confluent boundary layer with intermittent separation	Normal to flap surface
7	1.129	Separated boundary layer	Normal to flap surface
8	1.175	Separated boundary layer	Normal to flap surface
9	1.220	Separated boundary layer	Normal to flap surface
10	1.266	Separated boundary layer	Normal to flap surface
11	1.289	Separated boundary layer	Normal to flap surface
12	1.316	Wake with recirculating flow	Tunnel coordinates
13	1.372	Wake with recirculating flow	Tunnel coordinates
14	1.427	Wake with recirculating flow	Tunnel coordinates
15	1.483	Wake with recirculating flow	Tunnel coordinates
16	1.539	Wake with intermittent backflow	Tunnel coordinates
17	1.622	Wake	Tunnel coordinates
18	1.789	Wake	Tunnel coordinates
19	2.039	Wake	Tunnel coordinates
20	2.289	Wake	Tunnel coordinates
21	2.789	Wake	Tunnel coordinates

TABLE 2.- FREE-STREAM MAIN VELOCITY AND SHEAR-LAYER THICKNESS

SUCTION-SIDE SURFACE

Station no.	x/c	U_e, m/sec	$\delta_{0.995}$, mm	θ, deg
1	0.495	49.56	20	13
2	0.742	43.94	25	17
3	0.989	38.00	38	23
4	1.003	37.40	76	13
5	1.038	36.86	82	19
6	1.084	36.50	95	33
7	1.129	34.71	145	38
8	1.175	32.52	178	41.8
9	1.220	31.20	204	48
10	1.266	31.12	240	48.7
11	1.289	31.00	310	49.0

WAKE

Station no.	x/c	U_e (upper), m/sec	U_e (lower), m/sec	$\delta_{0.995}$, mm
12	1.316	33.09	31.70	310
13	1.372	31.60	30.29	312
14	1.427	31.10	28.80	320
15	1.483	31.00	27.52	330
16	1.539	30.98	27.76	335
17	1.622	30.84	28.50	343
18	1.789	30.79	30.94	362
19	2.039	30.75	30.38	381
20	2.289	30.00	29.98	358
21	2.789	29.96	29.83	355

TABLE 3.- TERMS IN THE MOMENTUM AND TURBULENCE KINETIC ENERGY TRANSPORT EQUATIONS

MOMENTUM TRANSPORT	
Streamwise	Symbol[a]
$(\delta^*/U_e^2)\ \langle U\rangle \frac{\partial\langle U\rangle}{\partial x} + \langle W\rangle \frac{\partial\langle U\rangle}{\partial z}$	— — —
$(\delta^*/U_e^2)\ \frac{\partial\langle u^2\rangle}{\partial x}$	———
$(\delta^*/U_e^2)\ \frac{\partial\langle uw\rangle}{\partial z}$	—·—
$(\delta^*/U_e^2)\ \frac{\partial\langle P\rangle}{\partial x}$	●
Cross-Stream	
$(\delta^*/U_e^2)\ \langle U\rangle \frac{\partial\langle W\rangle}{\partial x} + \langle W\rangle \frac{\partial\langle W\rangle}{\partial z}$	— — —
$(\delta^*/U_e^2)\ \frac{\partial\langle w^2\rangle}{\partial z}$	———
$(\delta^*/U_e^2)\ \frac{\partial\langle uw\rangle}{\partial x}$	—·—
$(\delta^*/U_e^2)\ \frac{\partial\langle P\rangle}{\partial z}$	●

TURBULENCE KINETIC ENERGY TRANSPORT	
$(\delta^*/U_e^3)\ \langle U\rangle \frac{\partial\langle k^2\rangle}{\partial x} + \langle W\rangle \frac{\partial\langle k^2\rangle}{\partial z}$	———
$(\delta^*/U_e^3)\ \langle u^2\rangle - \langle w^2\rangle \frac{\partial\langle U\rangle}{\partial x}$	—·—
$(\delta^*/U_e^3)\ \langle uw\rangle \frac{\partial\langle U\rangle}{\partial z}$	— — —
Imbalance	●

[a]See figures 25, 26, and 27.

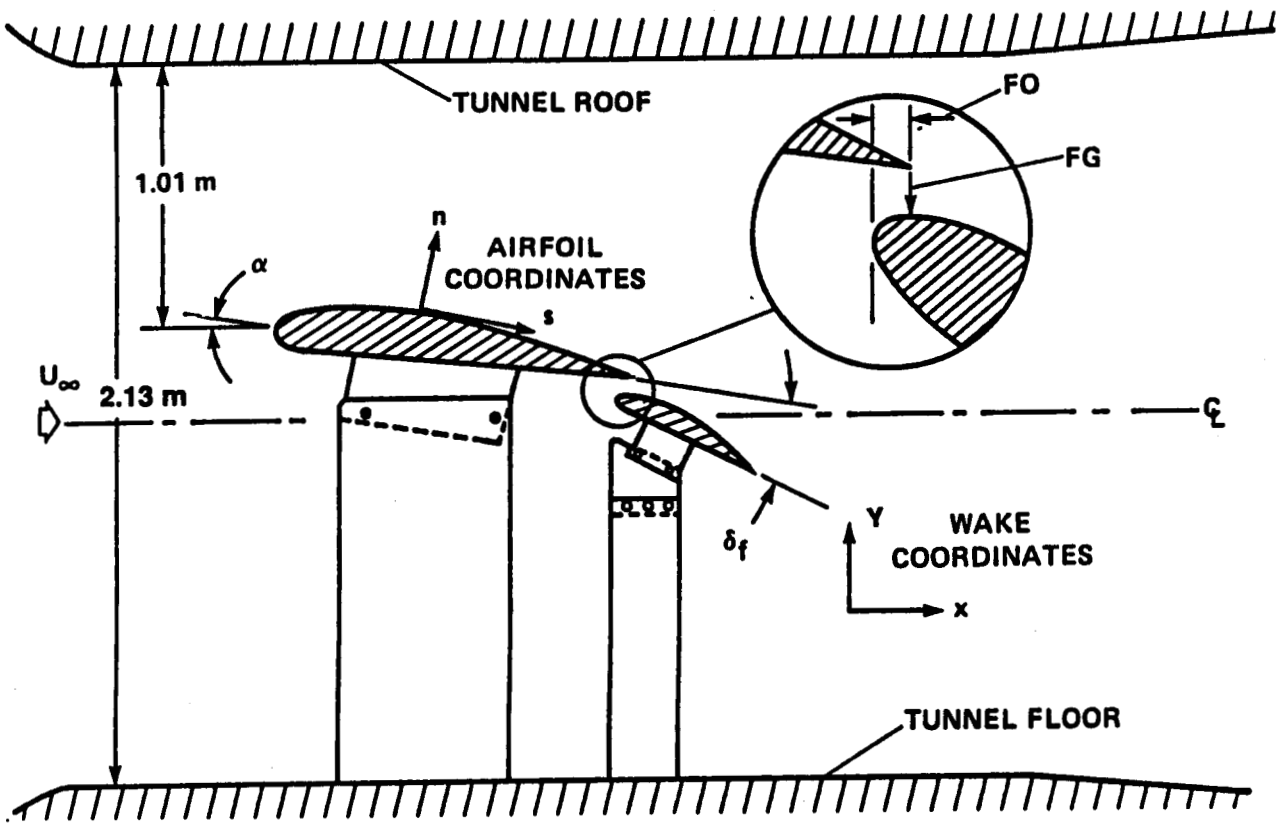

Figure 1.- Installation of airfoil in the Ames 7- by 10-Foot Wind Tunnel.

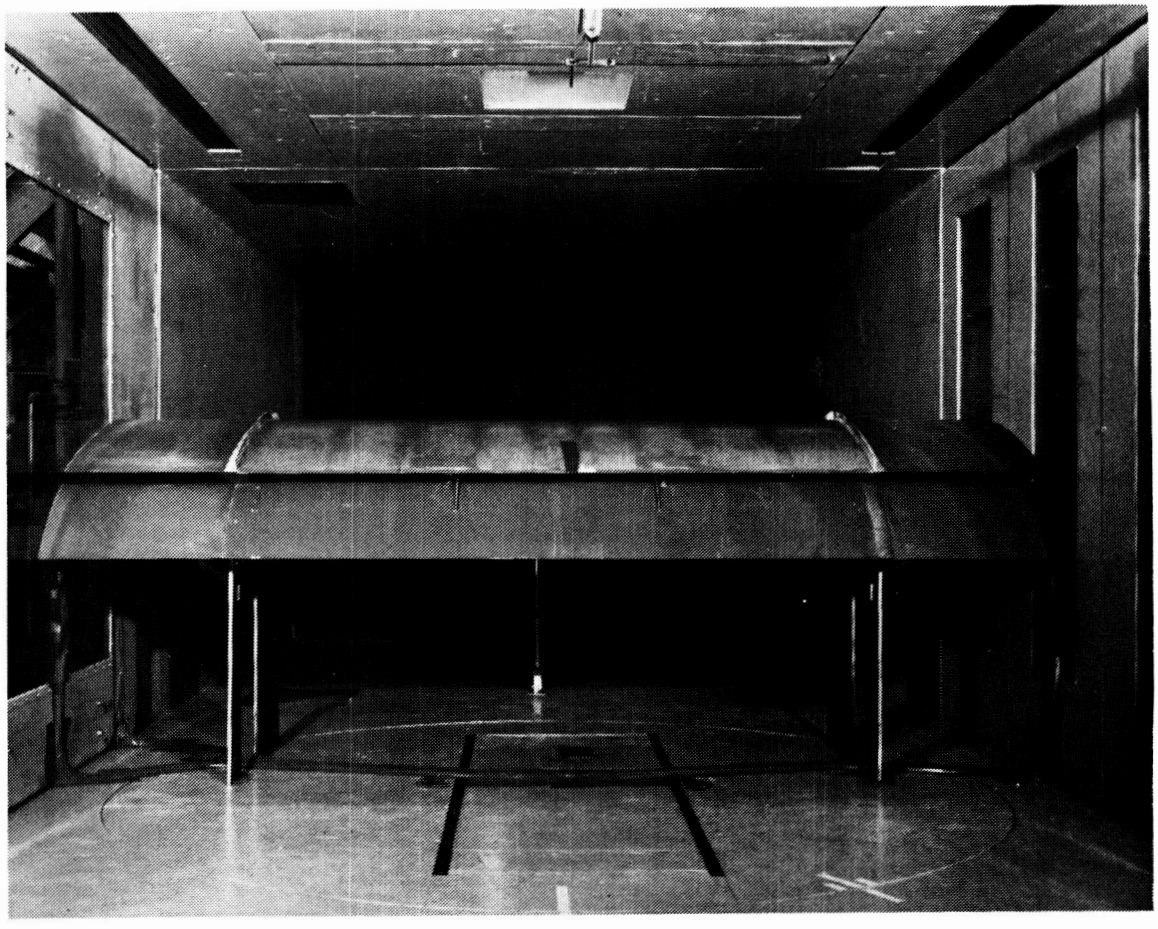

Figure 2.- Model installation in the Ames 7- by 10-Foot Wind Tunnel.

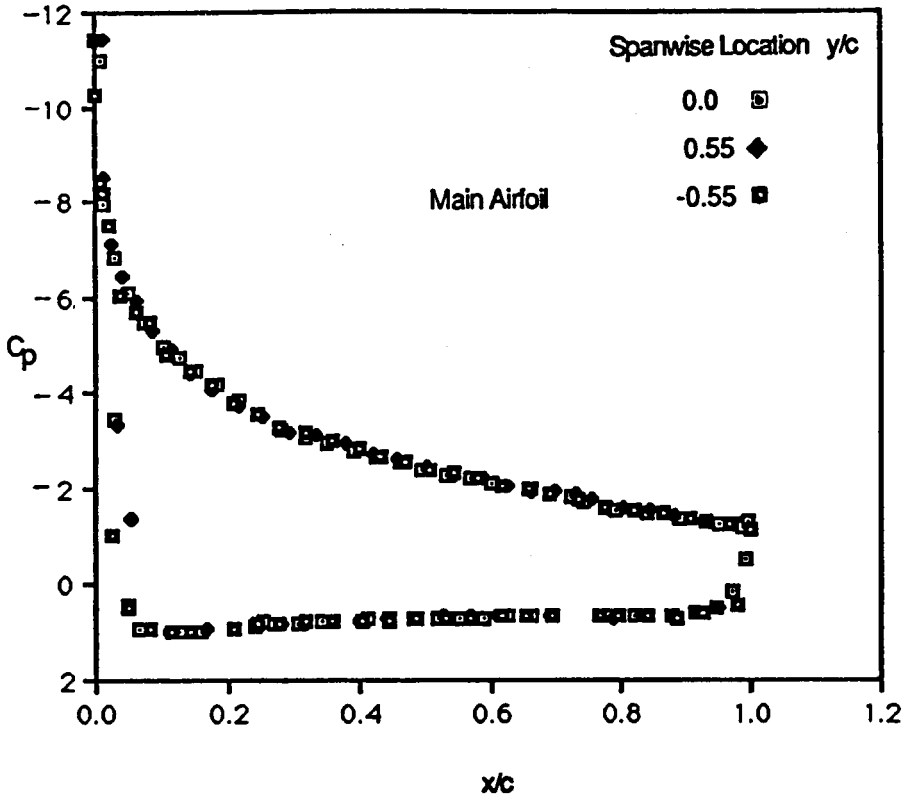

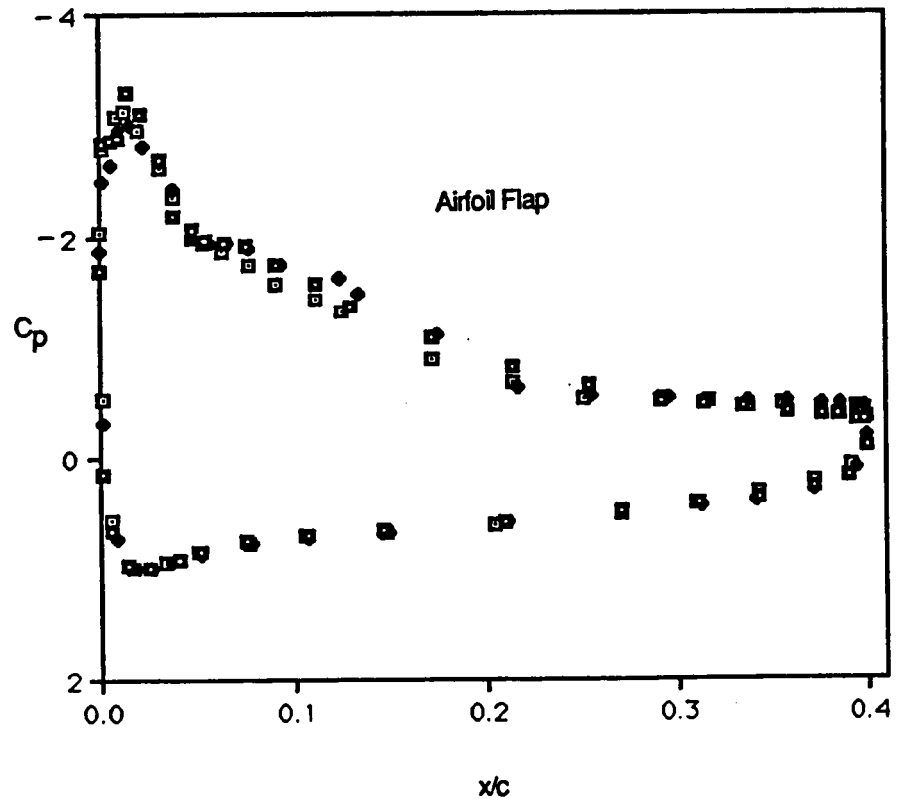

Figure 3.- Comparison of measured airfoil pressure distribution at three spanwise locations. α = 8.2°, δ_f = 26.8°, FG = 0.035 c, FO = 0.028 c.

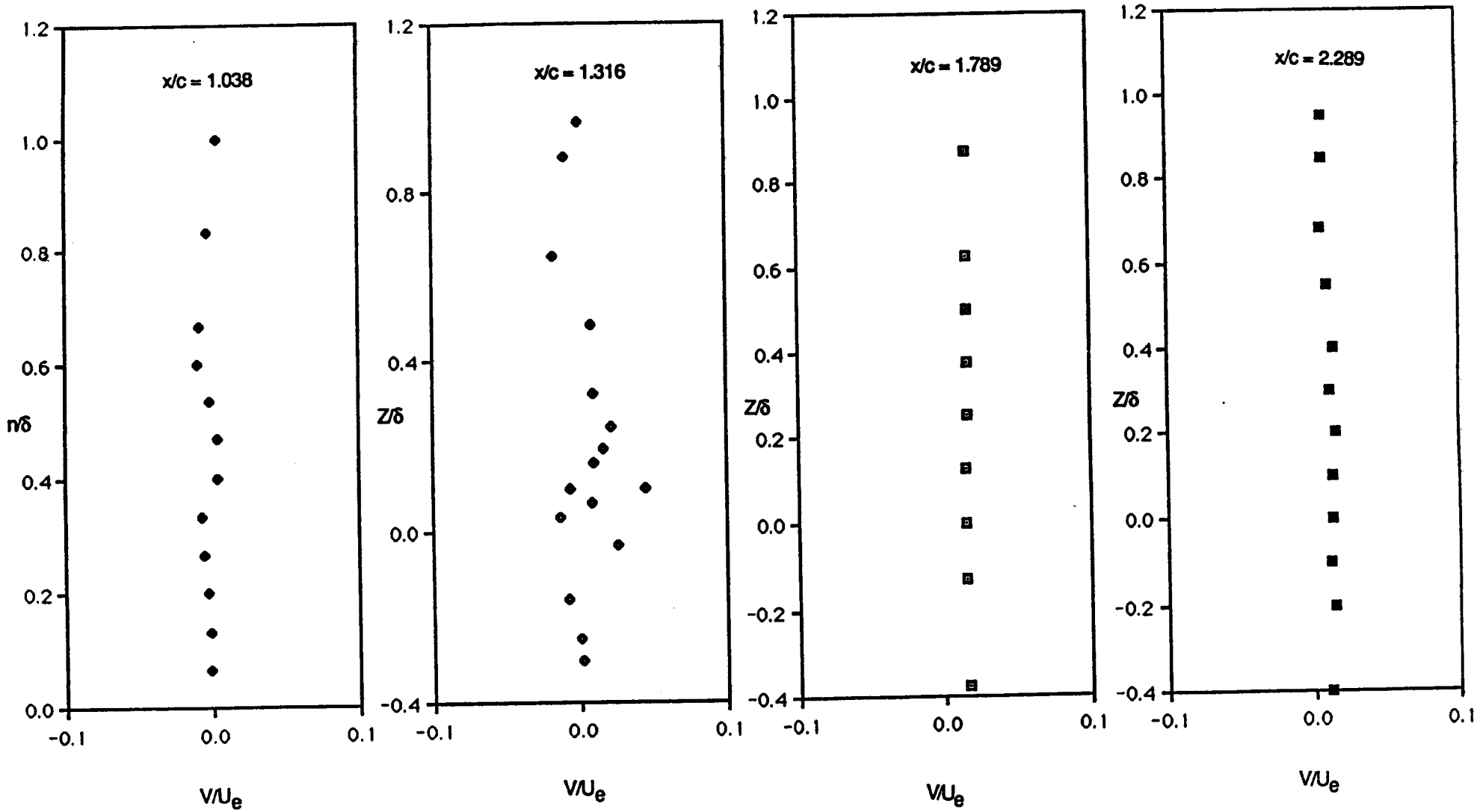

Figure 4(a).- Spanwise mean velocity measurements in the vicinity of separation and in the downstream wake.

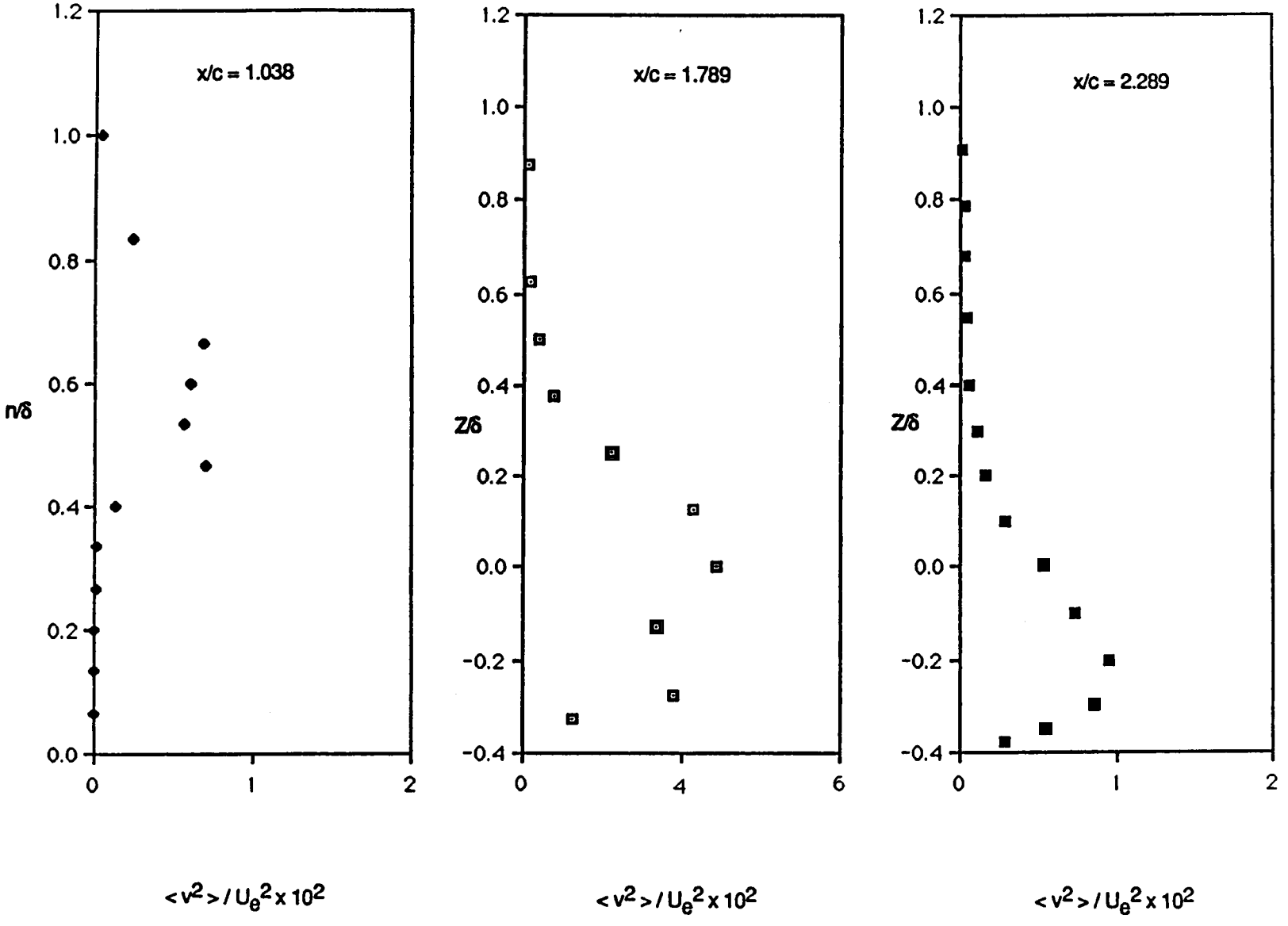

Figure 4(b).- Spanwise Reynolds normal stress distributions in the vicinity of separation and in the downstream wake.

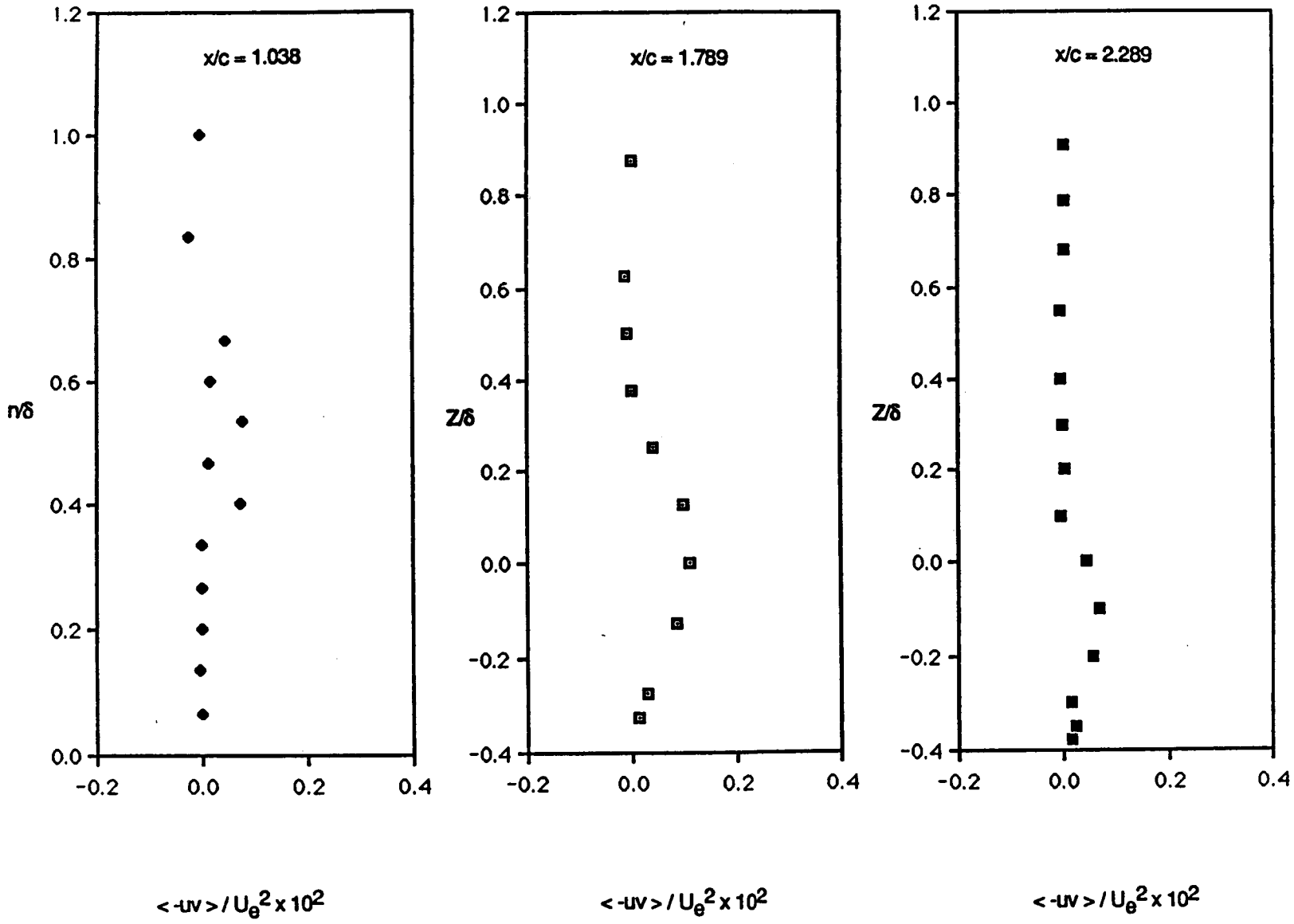

Figure 4(c).- Spanwise Reynolds shear stress distributions in the vicinity of separation and in the downstream wake.

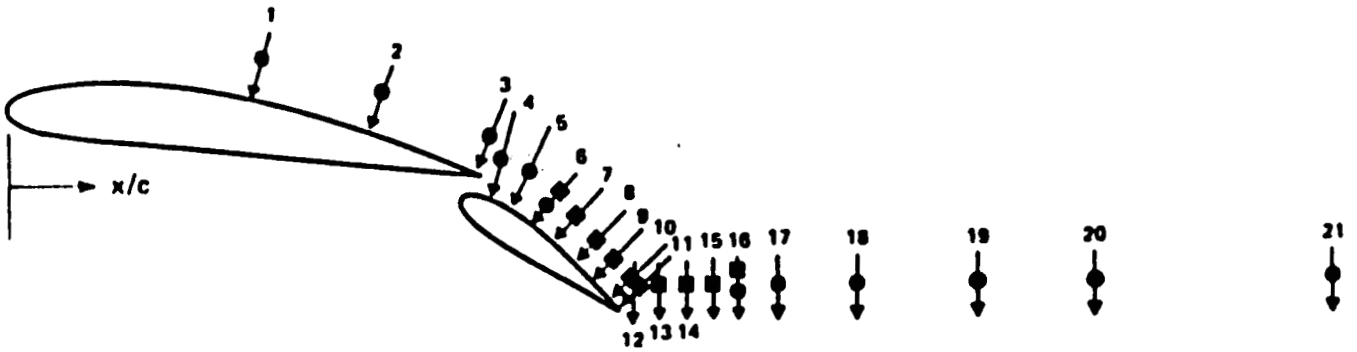

EXPERIMENTAL PROFILES

- HOT-WIRE
- LDV

Figure 5.- Orientation and location of velocity profiles.

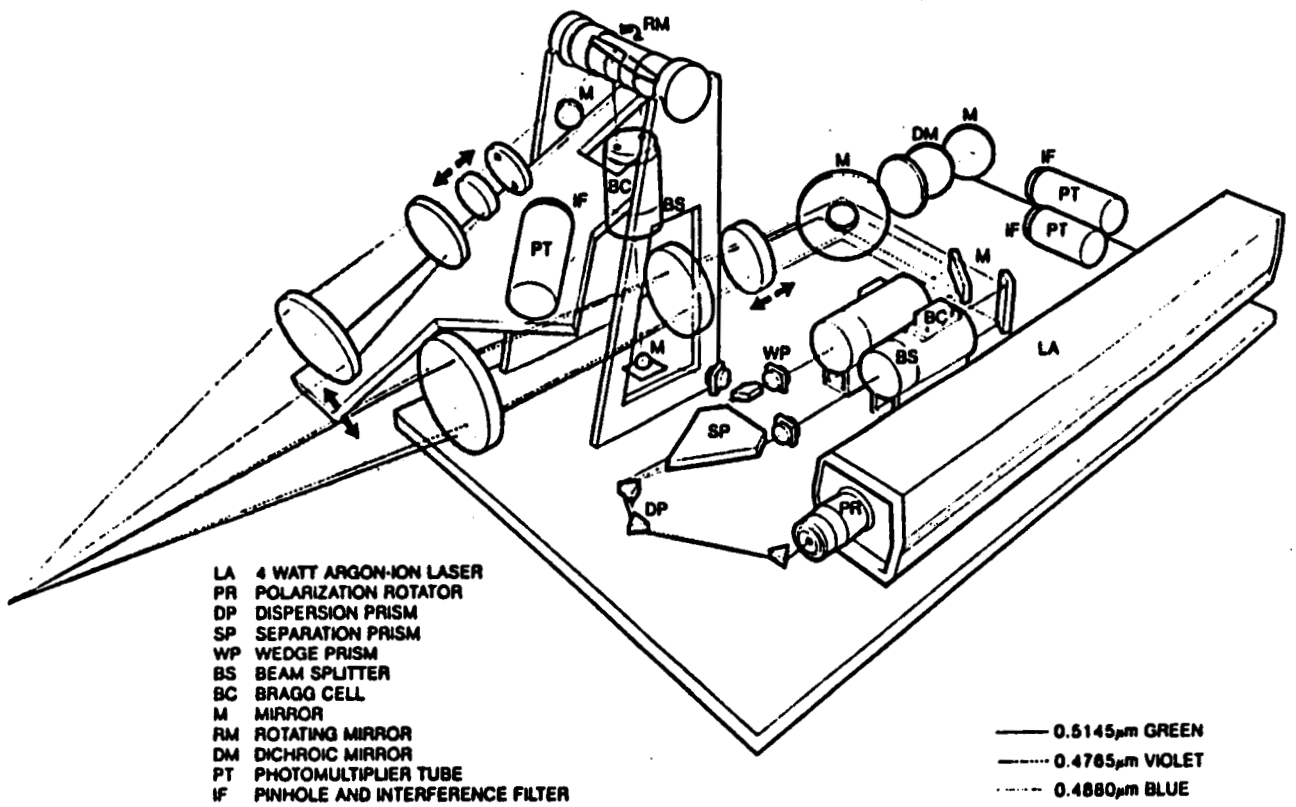

Figure 6.- 3-D LV.

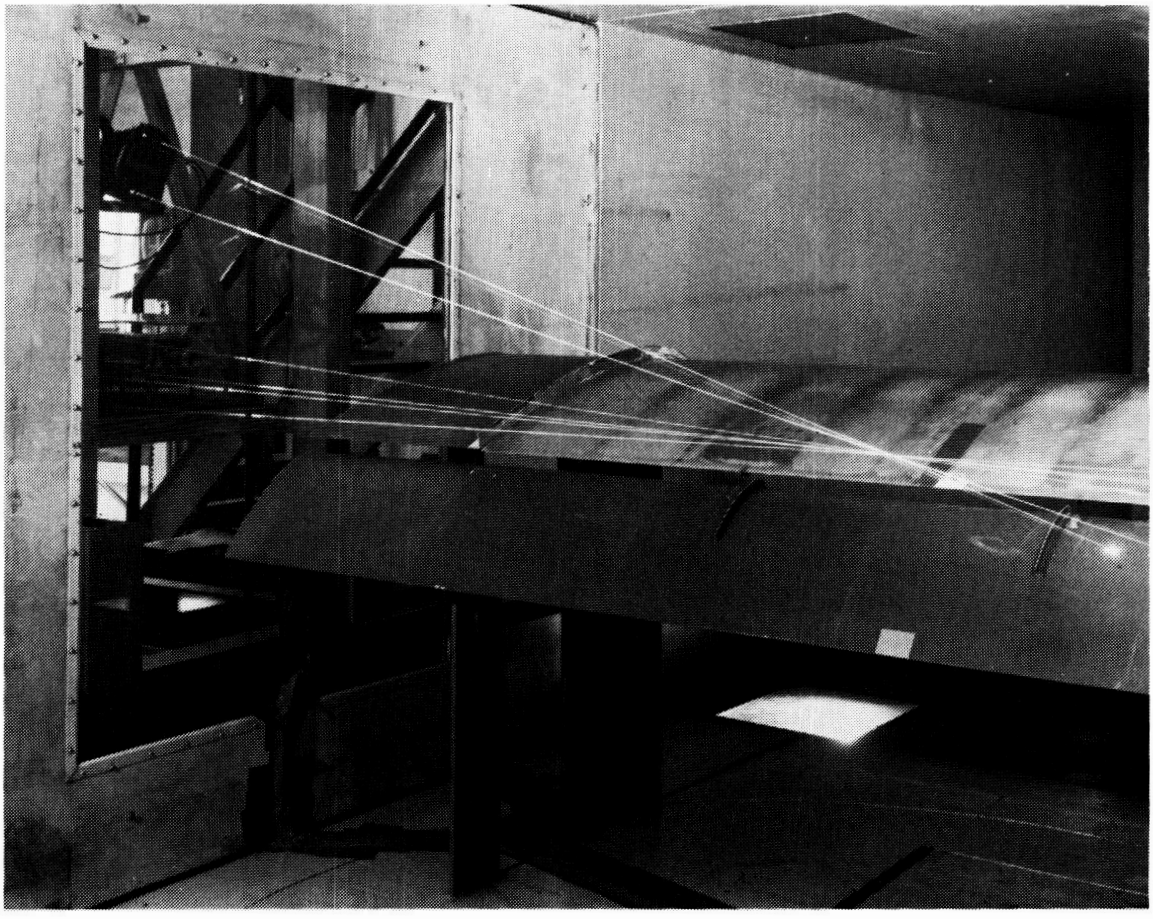

Figure 7.- 3-D LV in relation to wind tunnel and model.

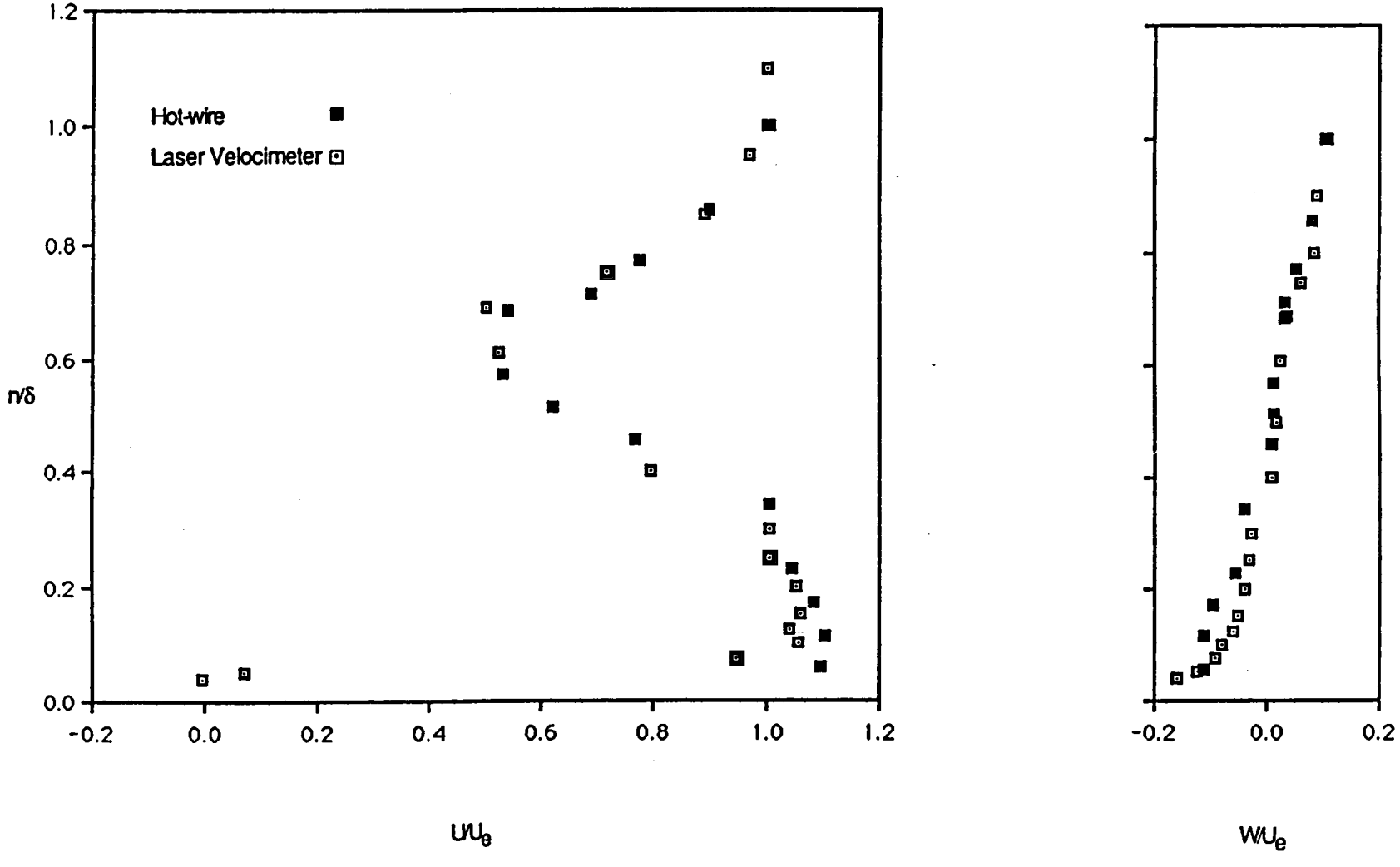

(a) Mean velocity at x/c = 1.084.

Figure 8.- Comparison of hot-wire and LV velocity results.

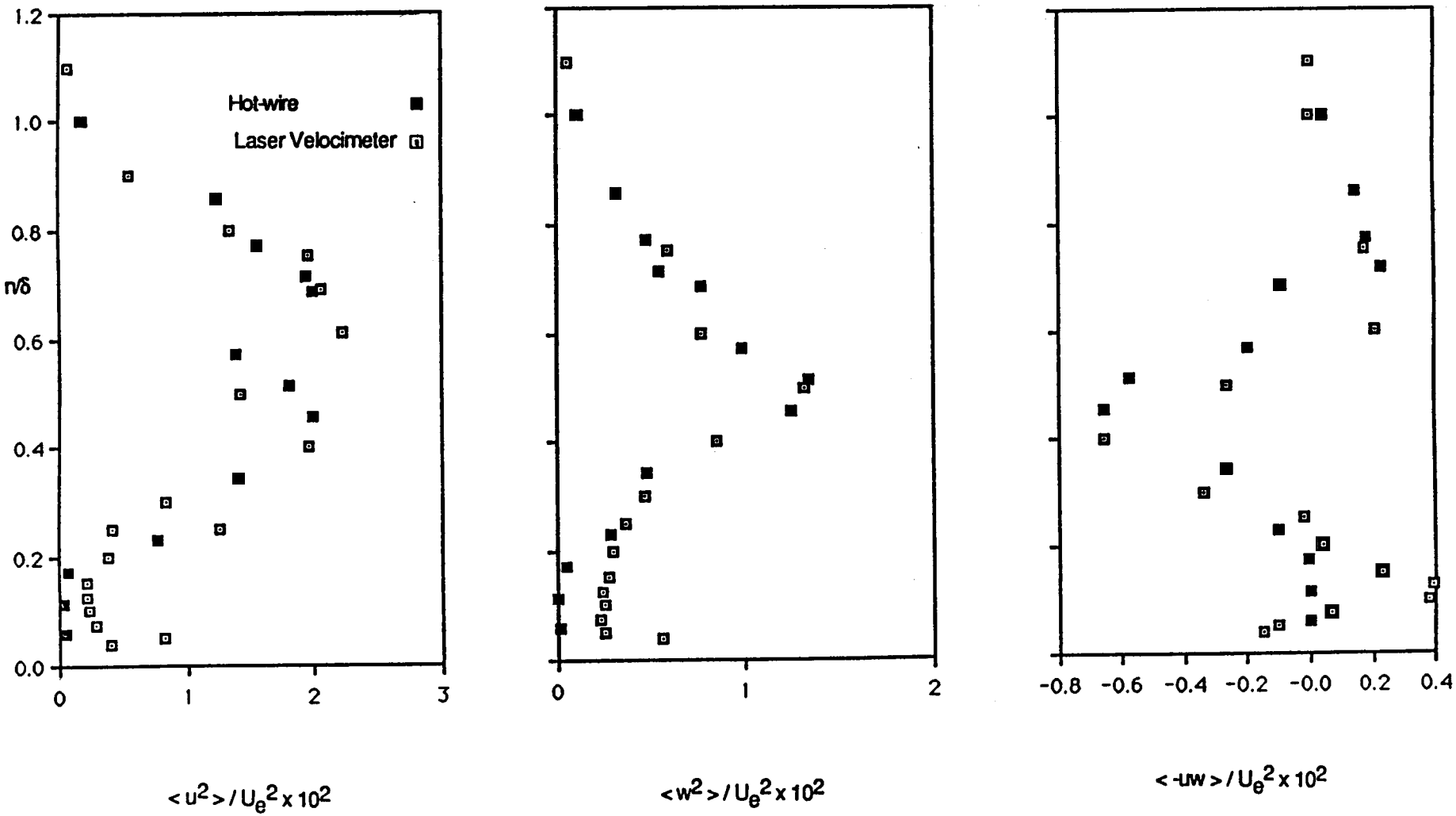

(b) Turbulence results at x/c = 1.084.

Figure 8.- Continued.

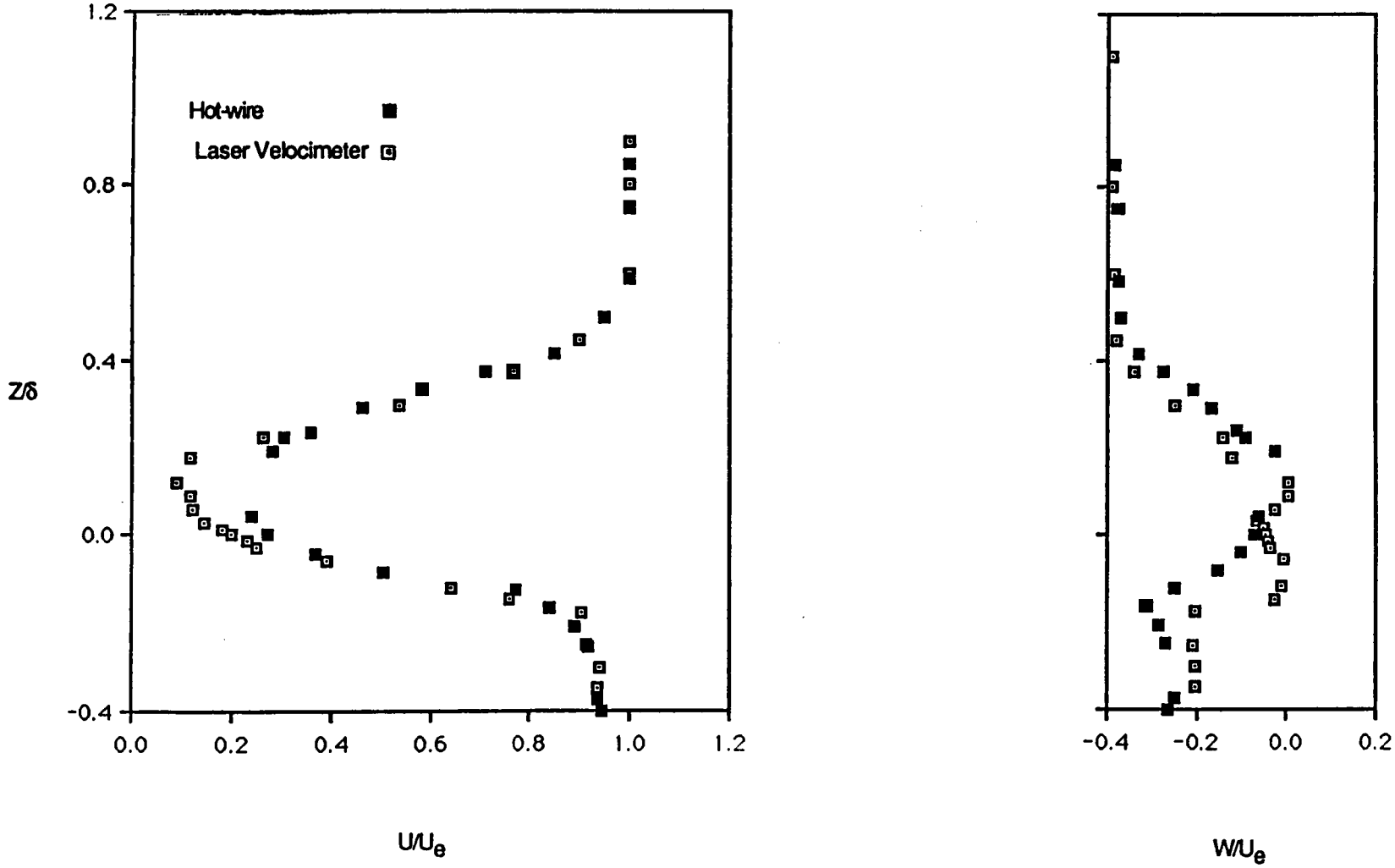

(c) Mean velocity at x/c = 1.539.

Figure 8.- Continued.

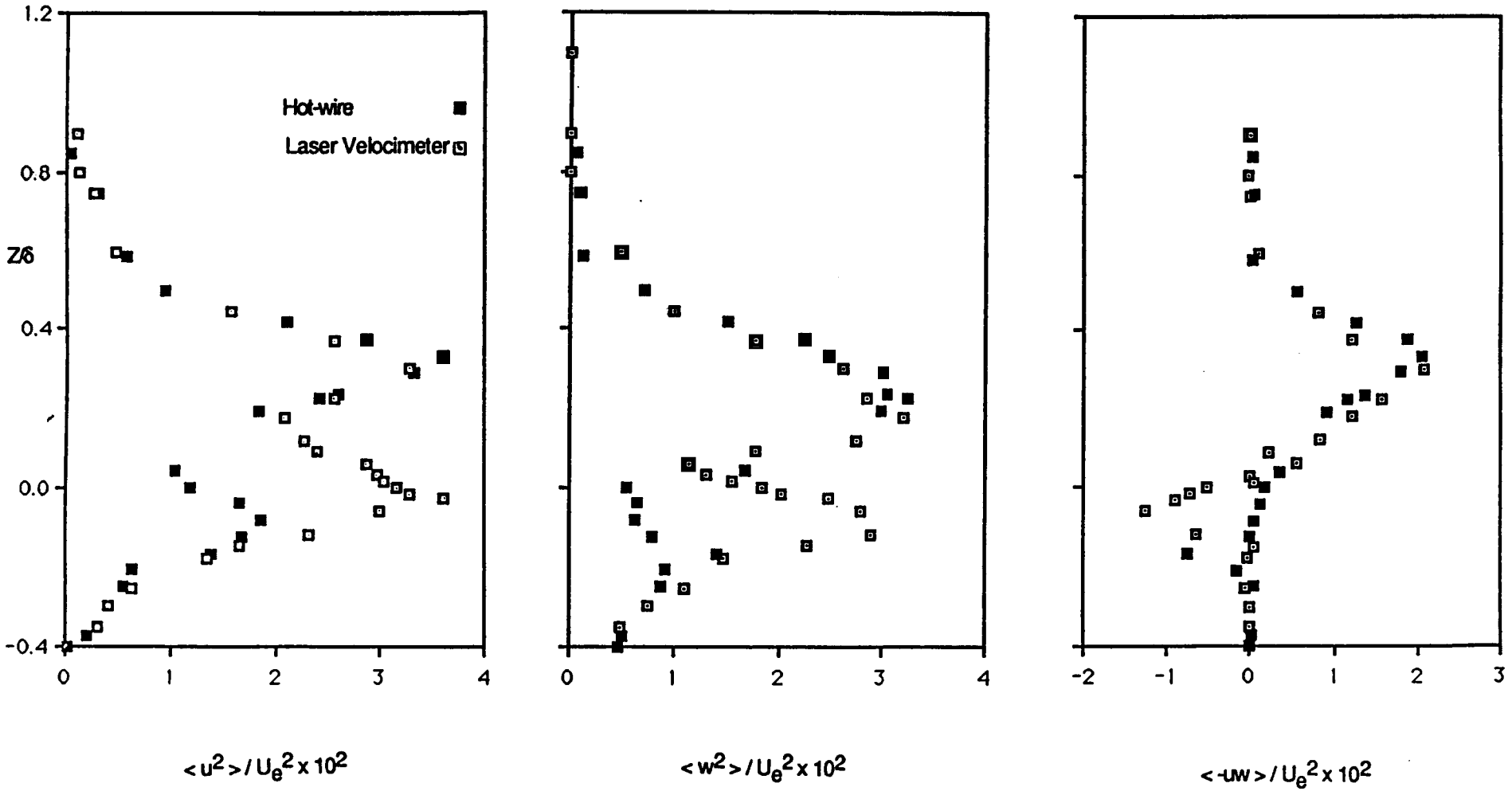

(d) Turbulence results at x/c = 1.539.

Figure 8.- Concluded.

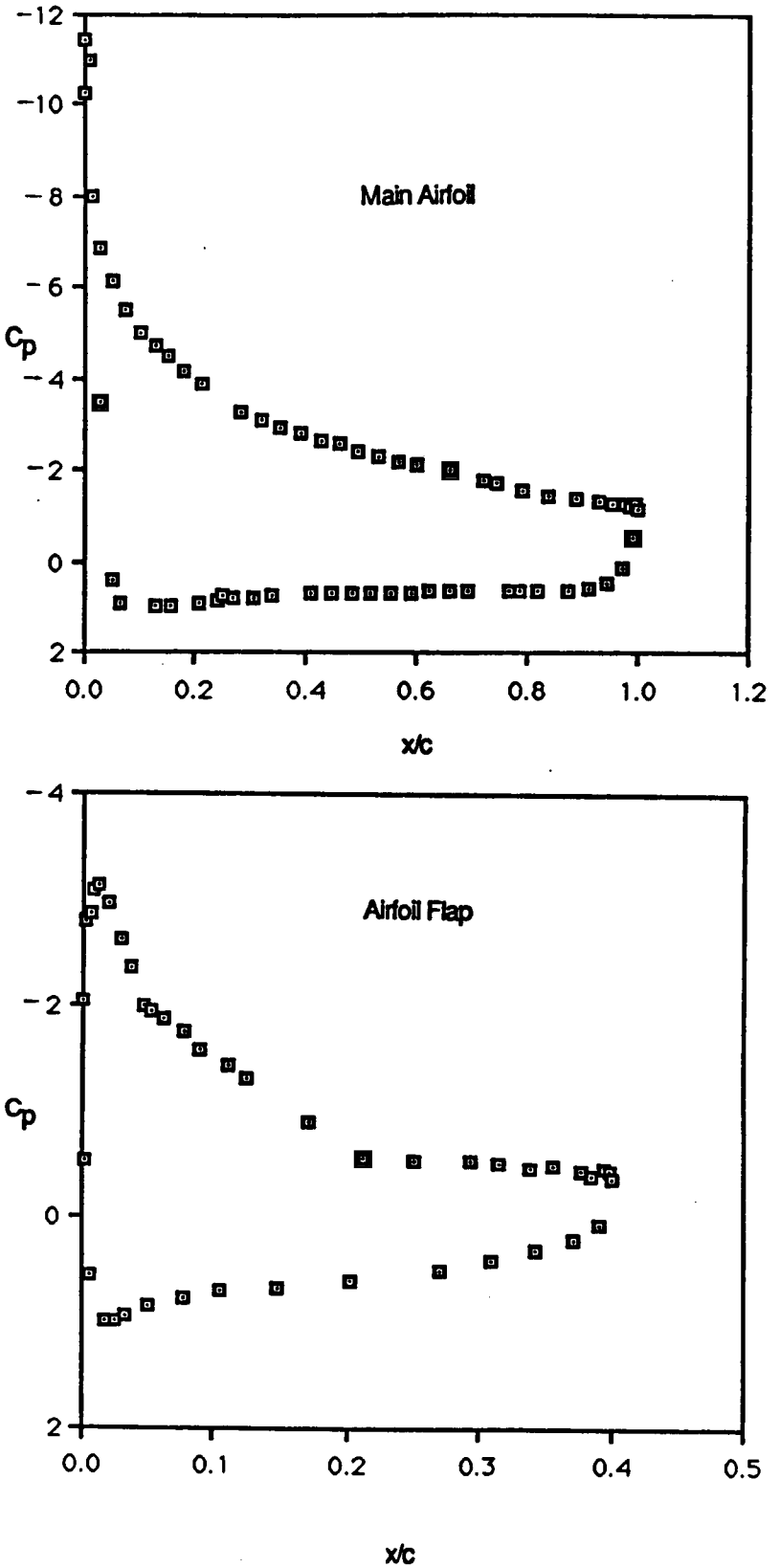

Figure 9.- Centerline surface pressure distributions for the present configuration; $\alpha = 8.2°$, $\delta_f = 26.8°$, FG = 0.035c, FO = 0.028c.

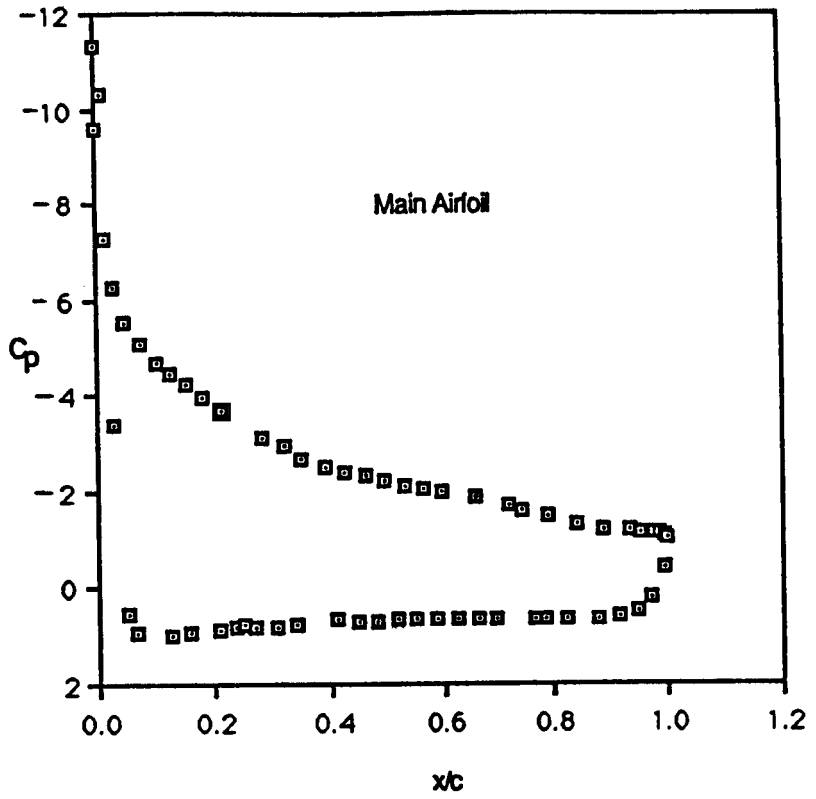

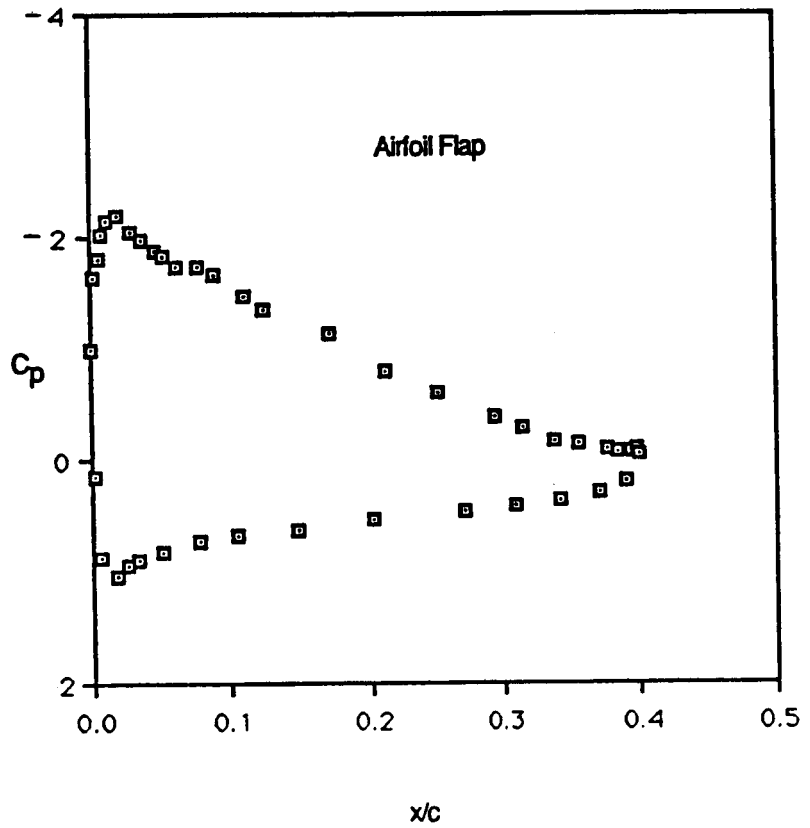

(a) α = 8.2°, δ_f = 21.8°, FG = 0.035c, FO = 0.028c.

Figure 10.- Surface pressure distributions.

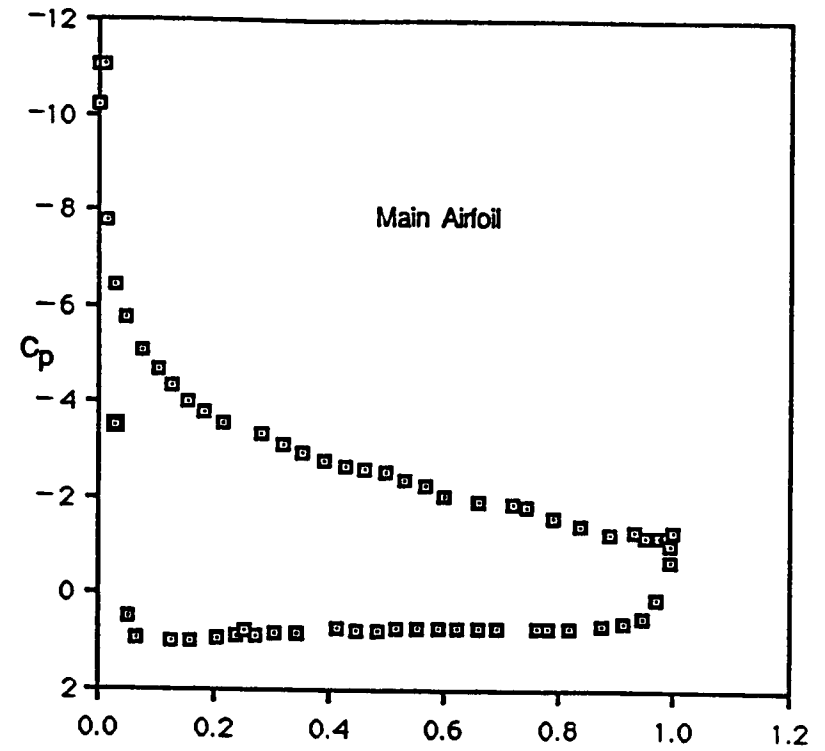

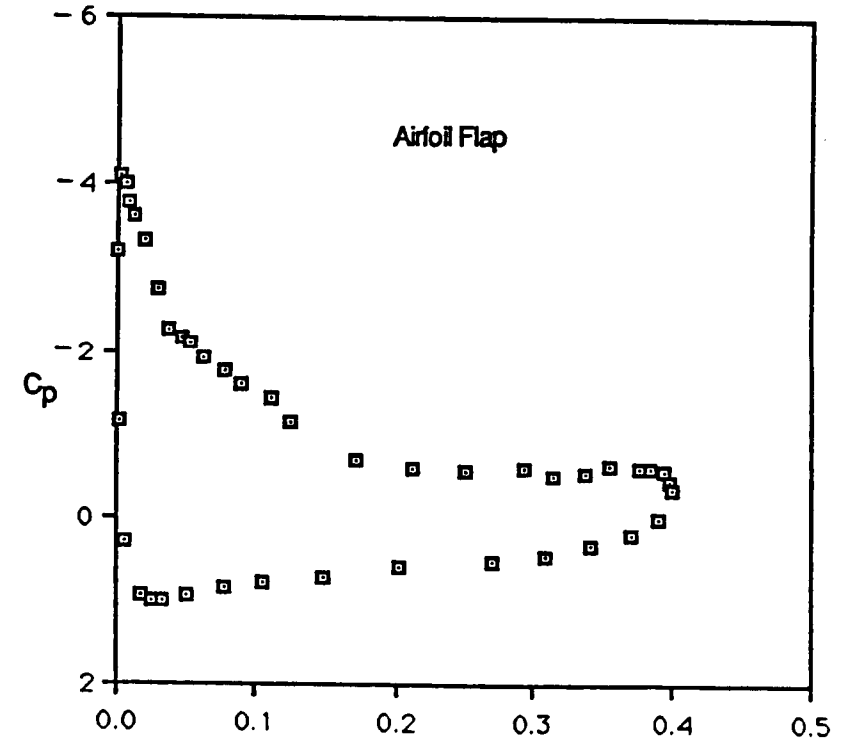

(b) α = 8.2°, δ_f = 31.8°, FG = 0.35c, FO = 0.028c.

Figure 10.- Continued.

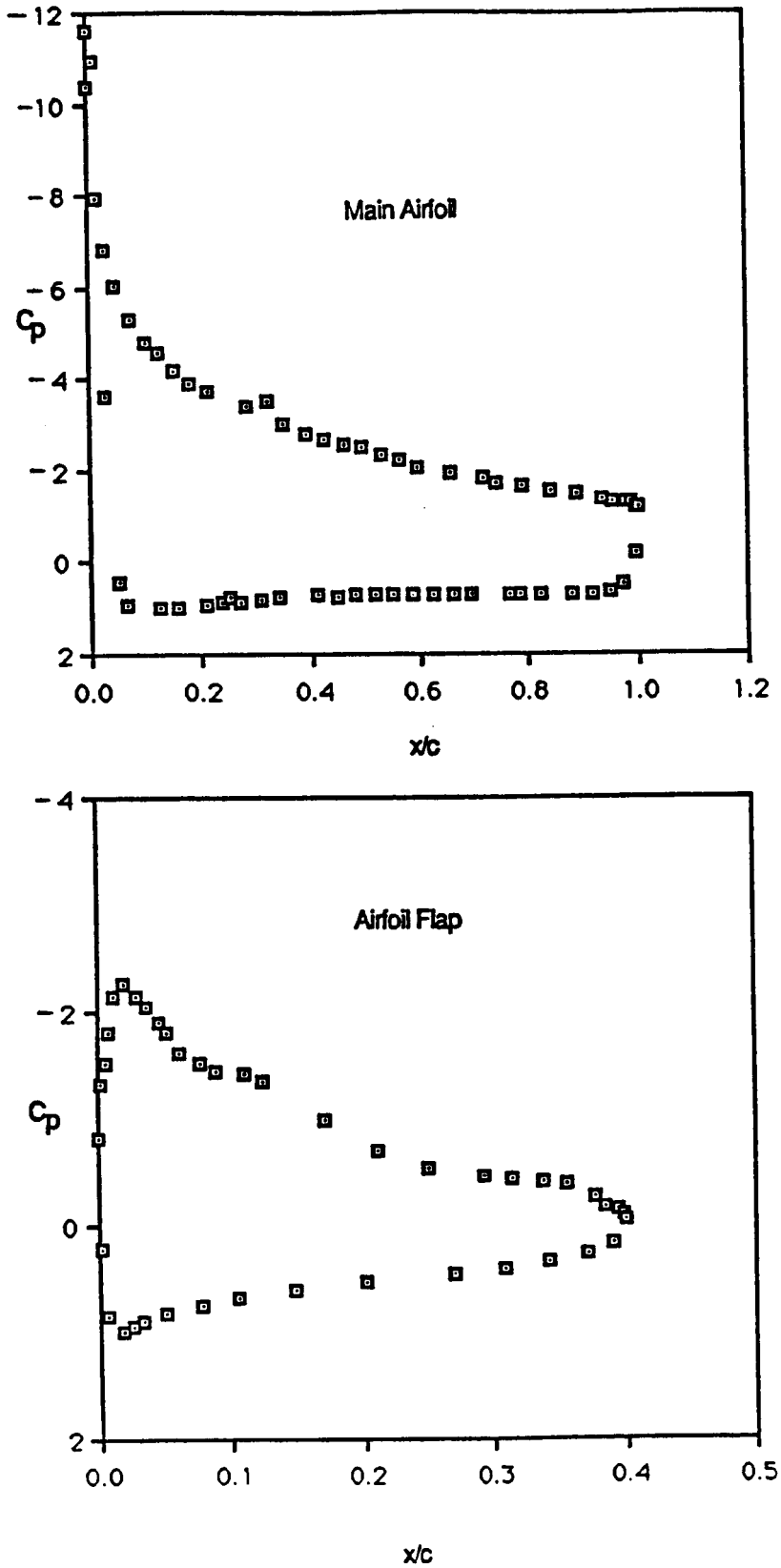

(c) α = 8.2°, δ_f = 26.8°, FG = 0.0156c, FO = 0.028c.

Figure 10.- Concluded.

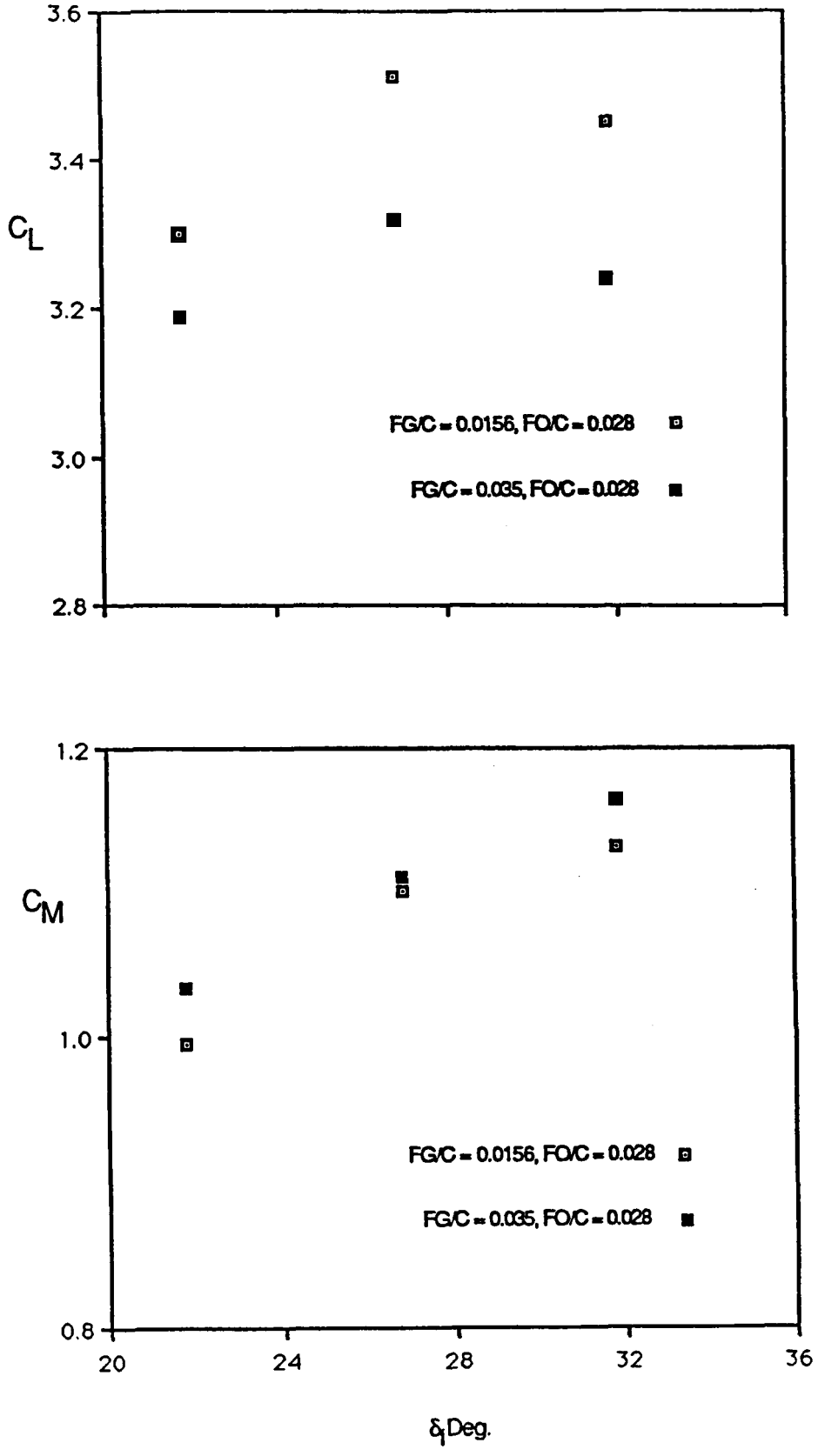

Figure 11.- Airfoil section characteristics.

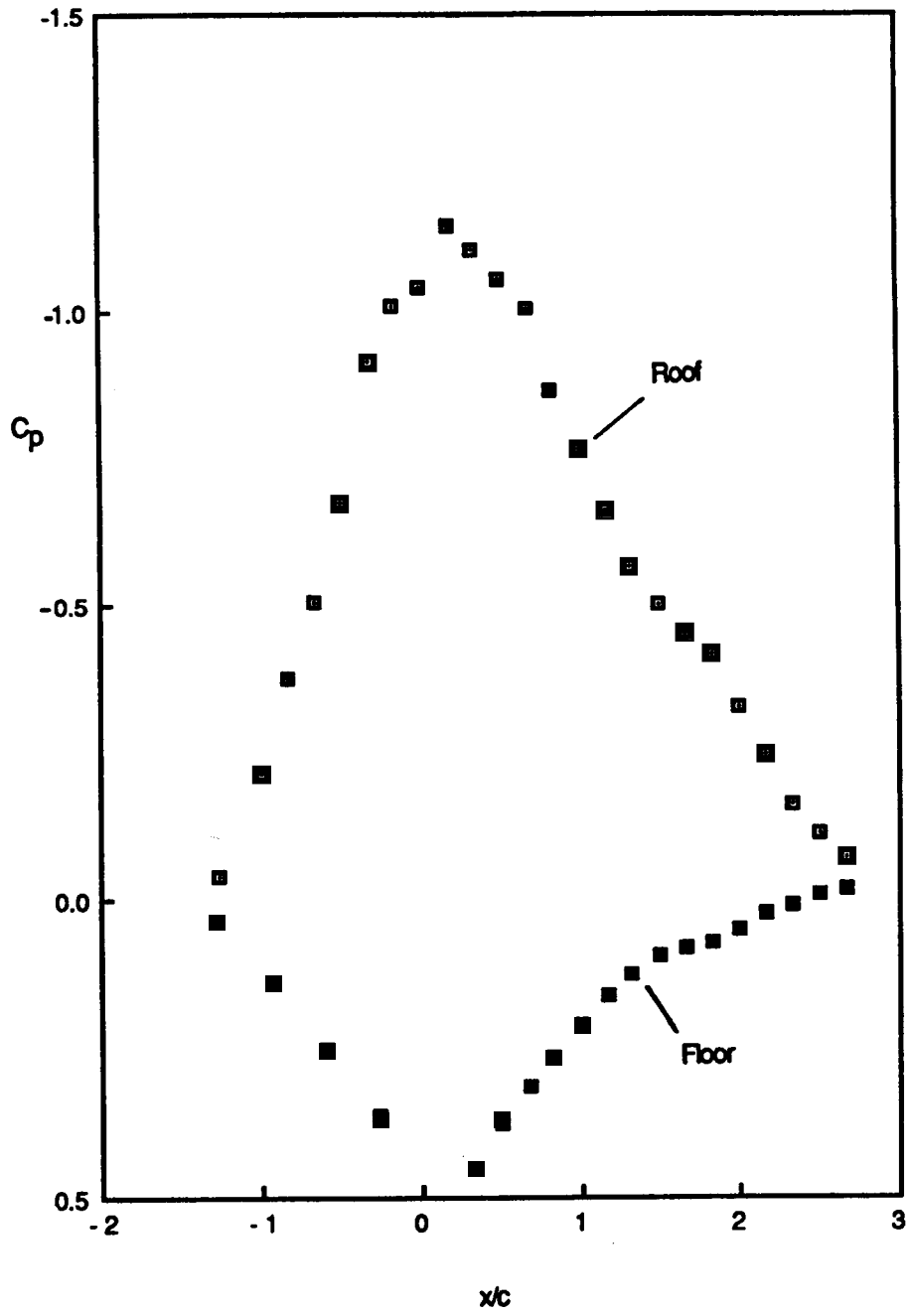

Figure 12(a).- Tunnel wall pressure measurements.

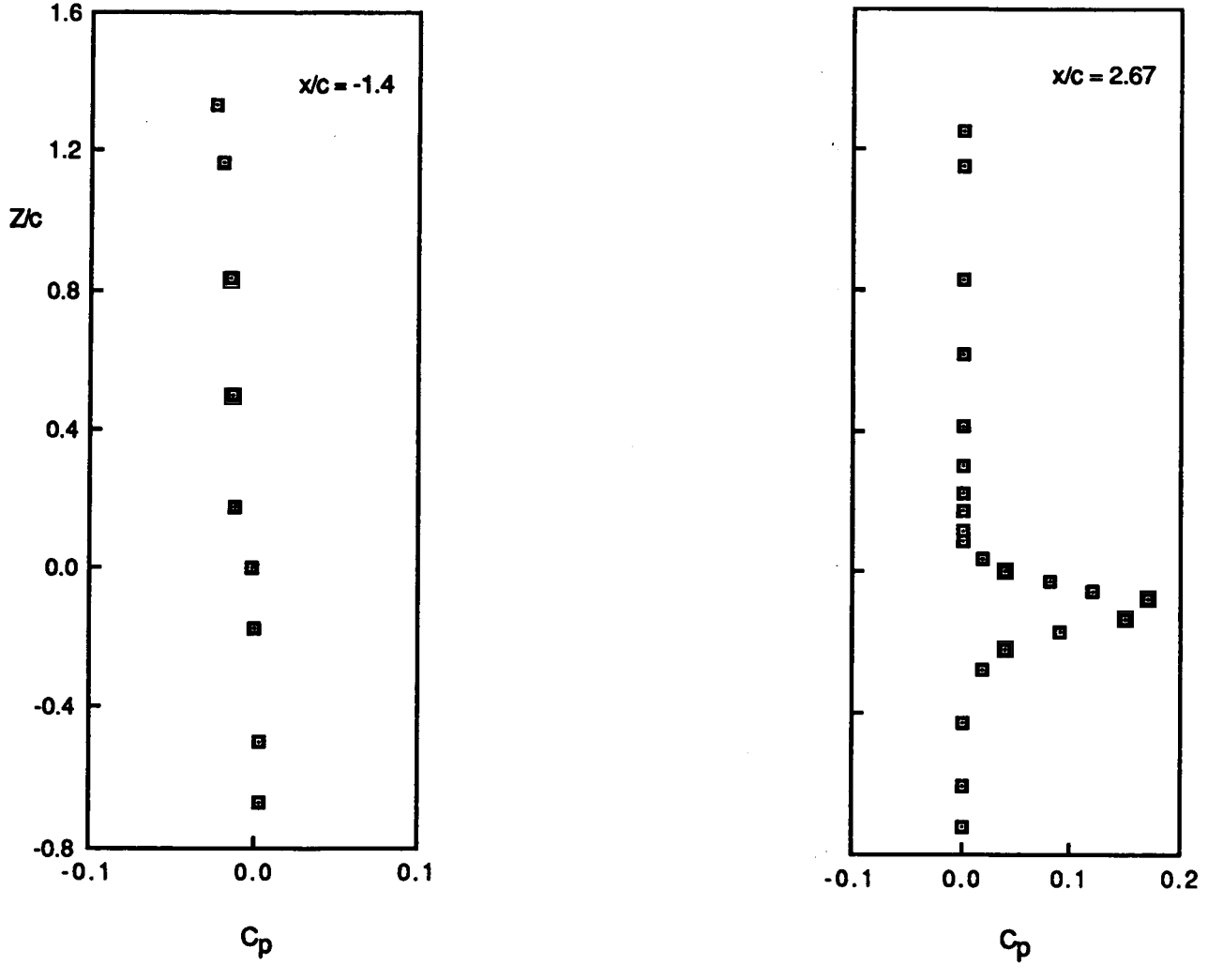

Figure 12(b).- Static pressure surveys upstream and downstream from airfoil.

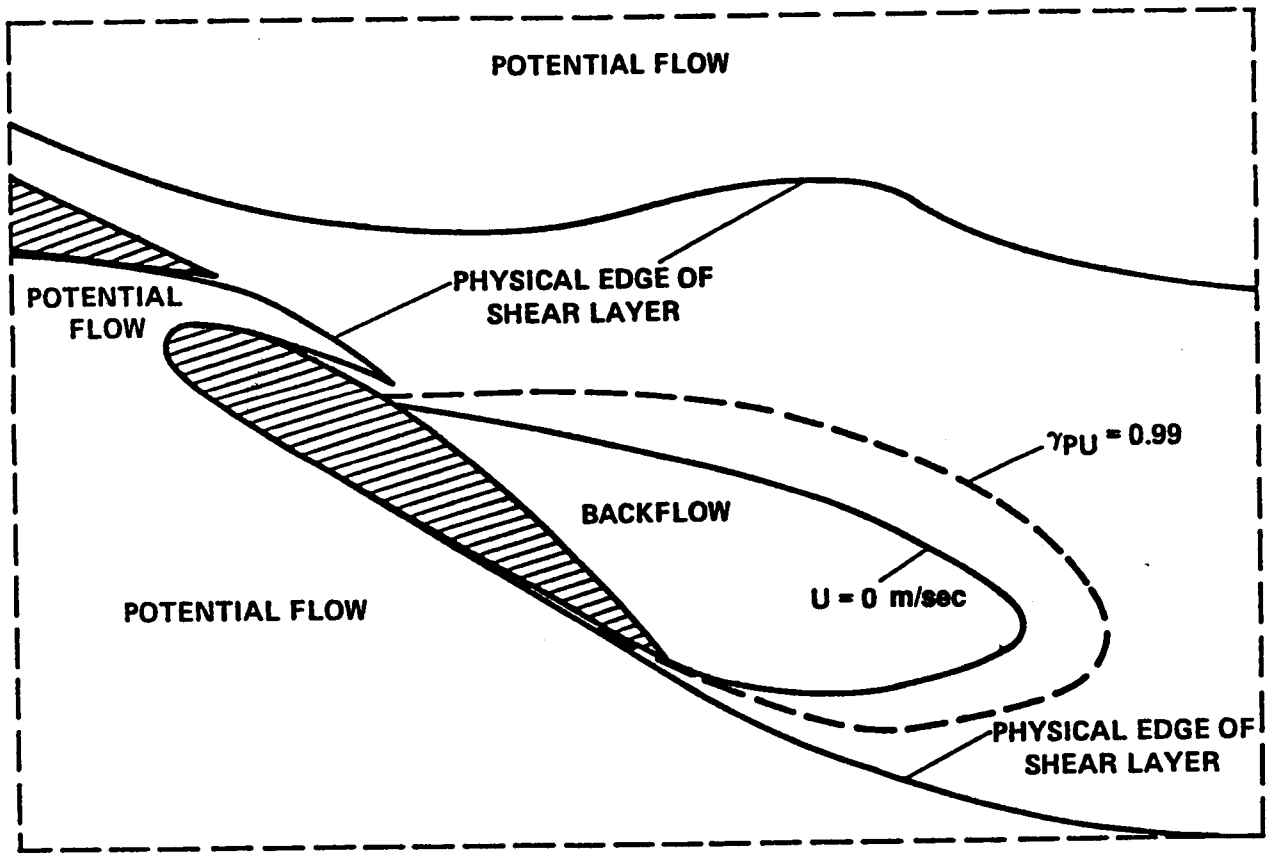

Figure 13.- Flow domains in the vicinity of the airfoil flap trailing edge.

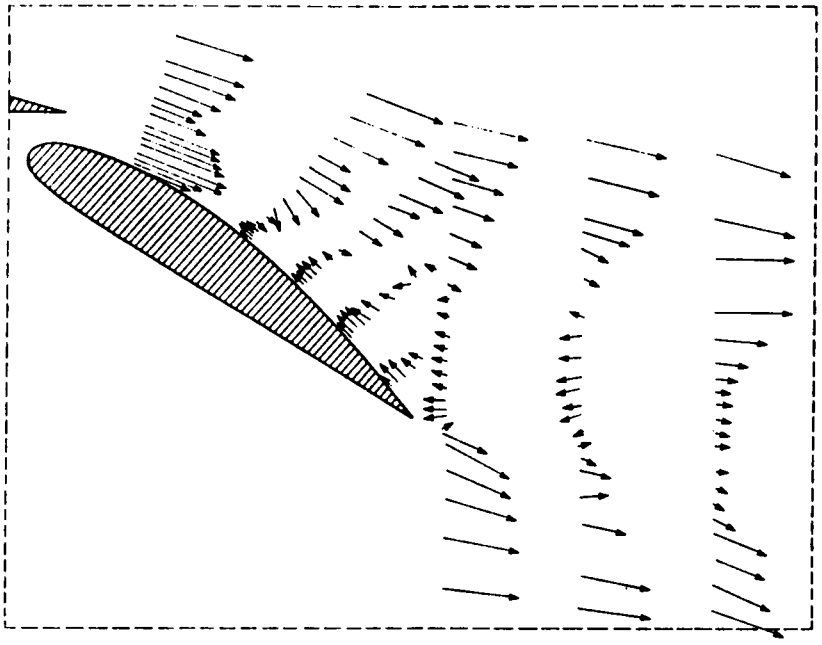

Figure 14(a).- Vectors representing mean velocity.

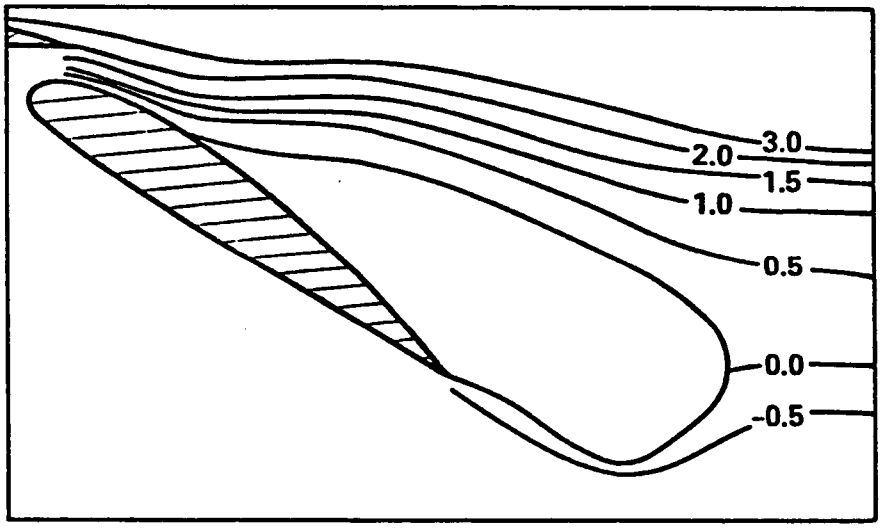

Figure 14(b).- Streamlines in the vicinity of recirculation.

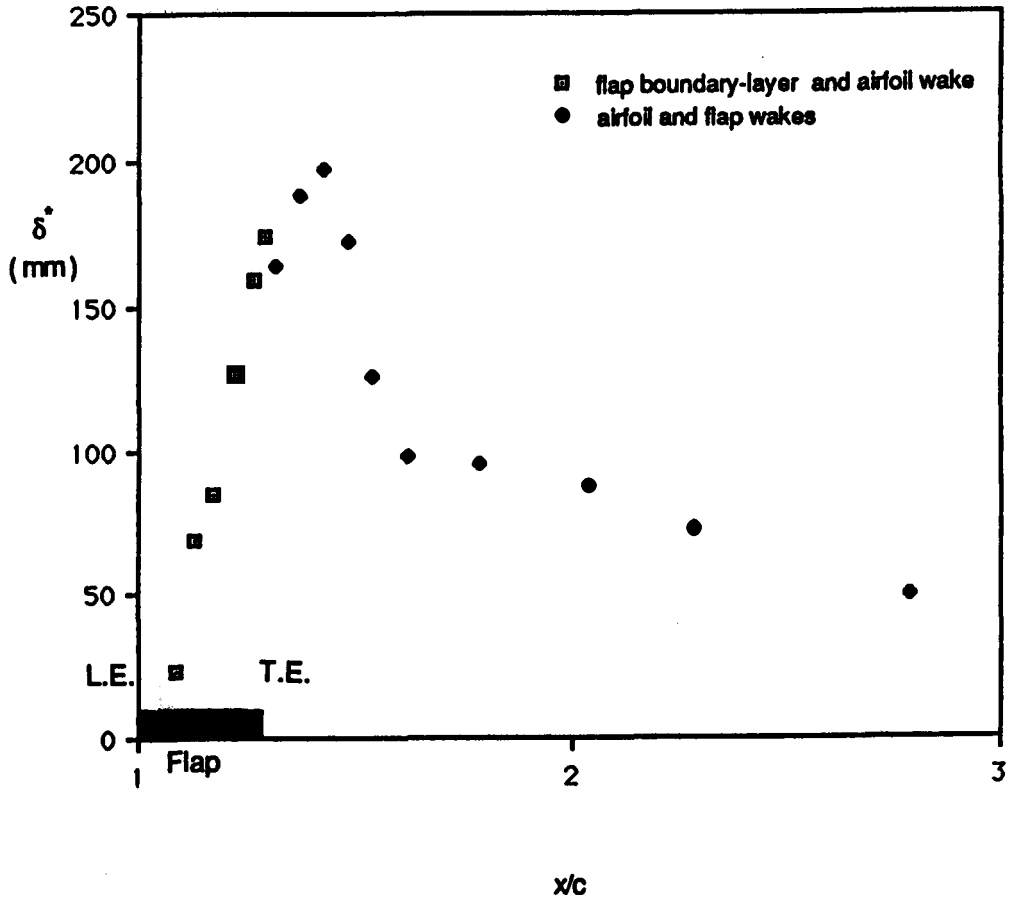

Figure 15(a).- Integral parameters of mean-flow development.

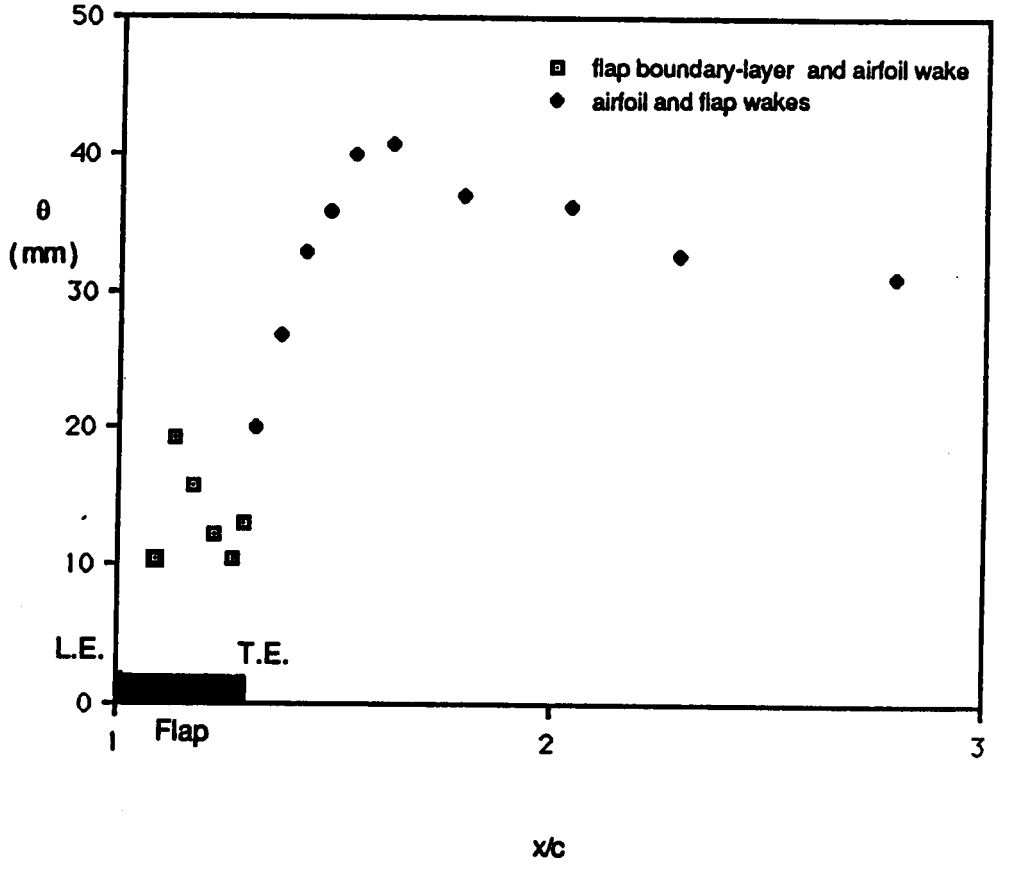

Figure 15(b).- Integral parameters of mean-flow development.

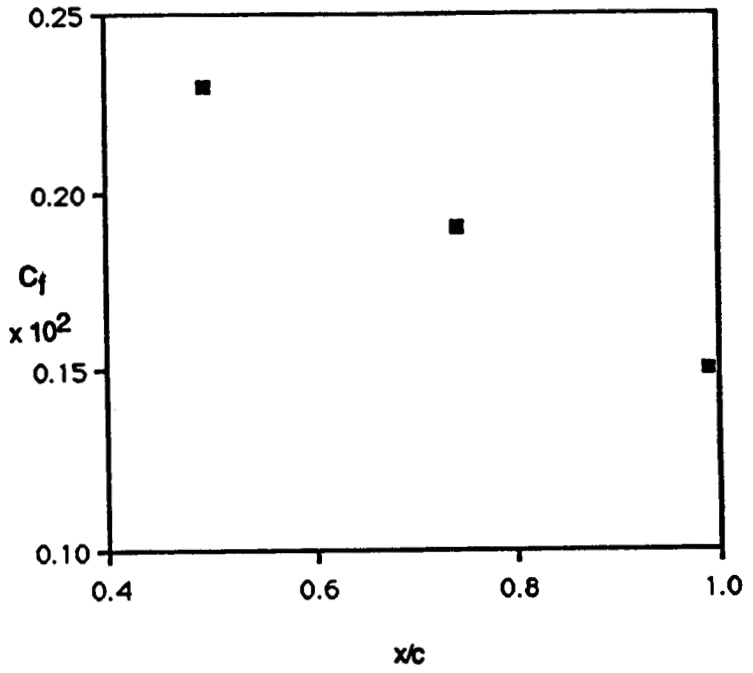

(a) On the main airfoil.

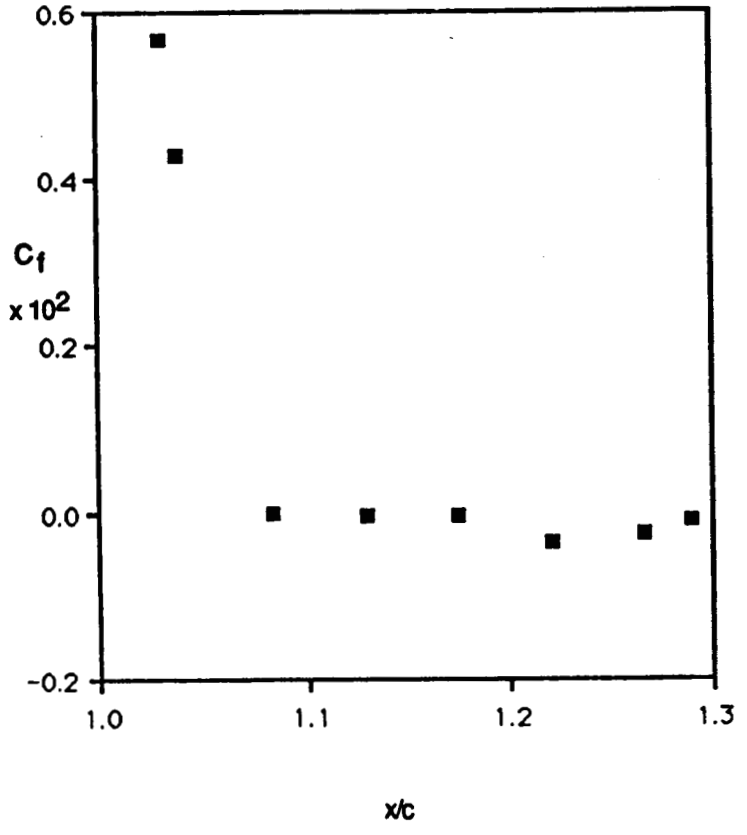

(b) On the airfoil flap.

Figure 16.- Distribution of skin friction.

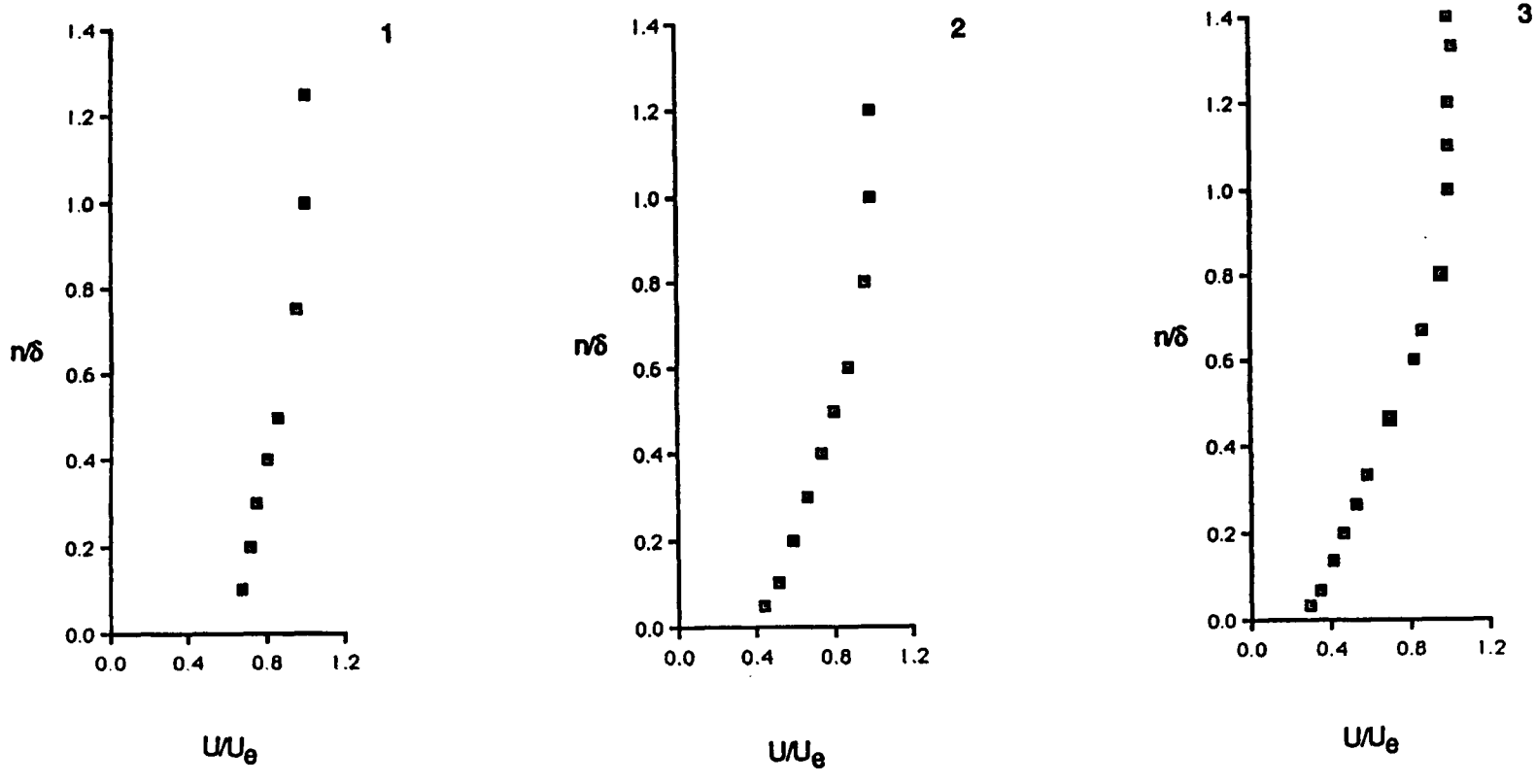

Figure 17.- Distribution of streamwise mean velocity (station numbers refer to Table 1, and Fig. 5).

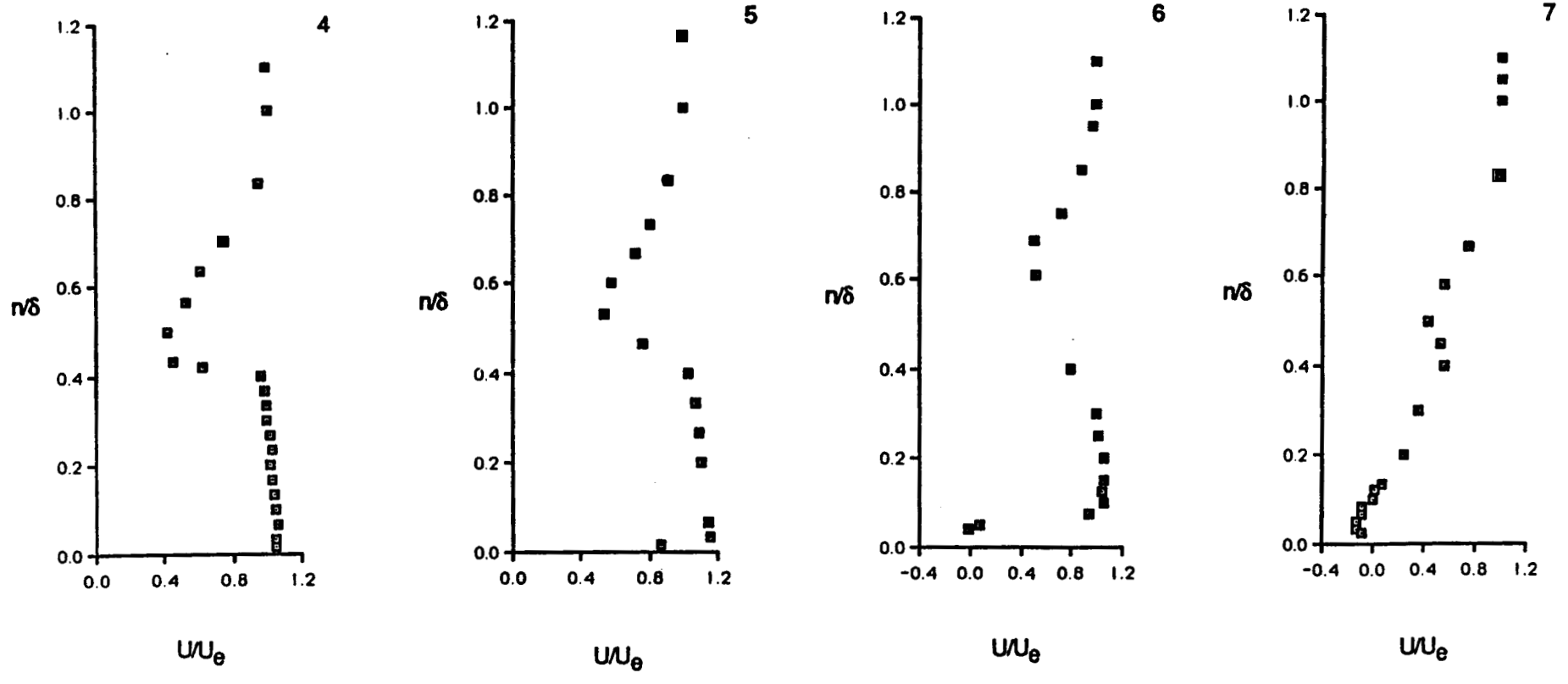

Figure 17.- Continued.

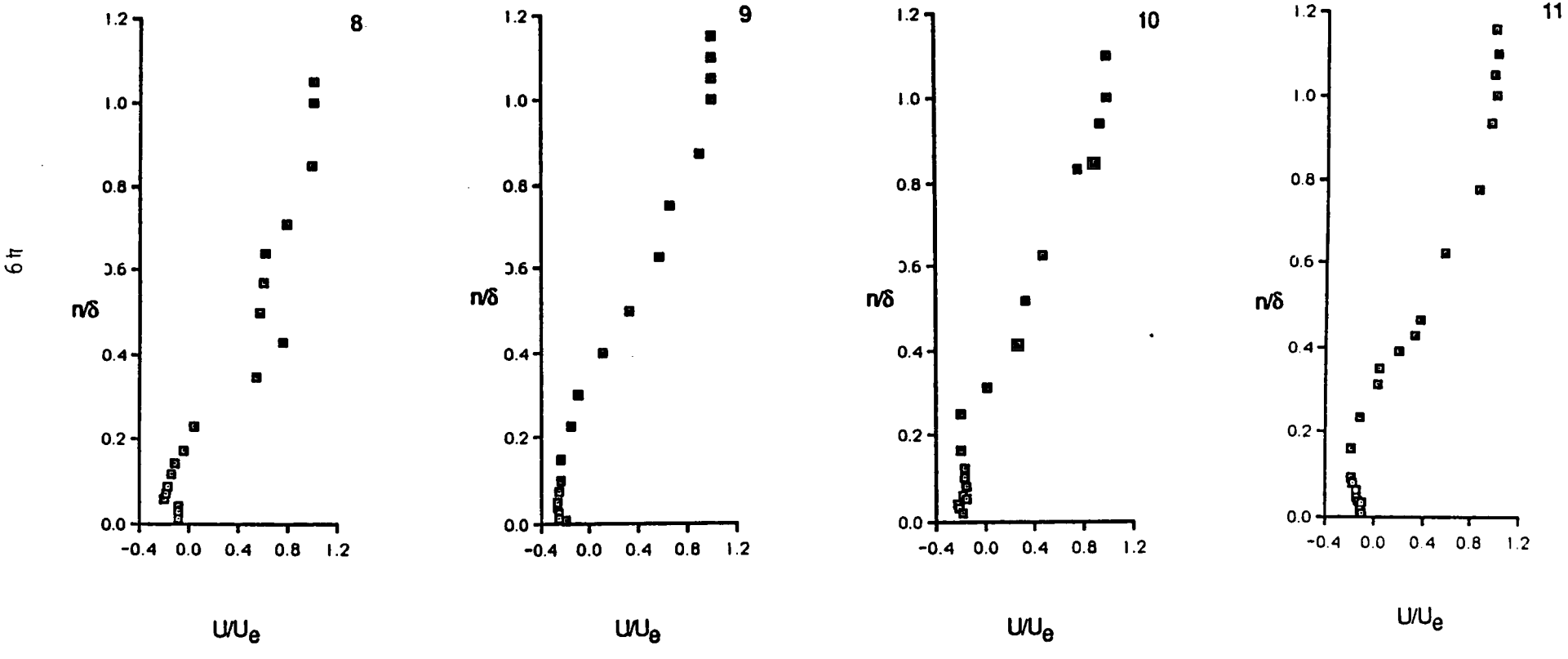

Figure 17.- Continued.

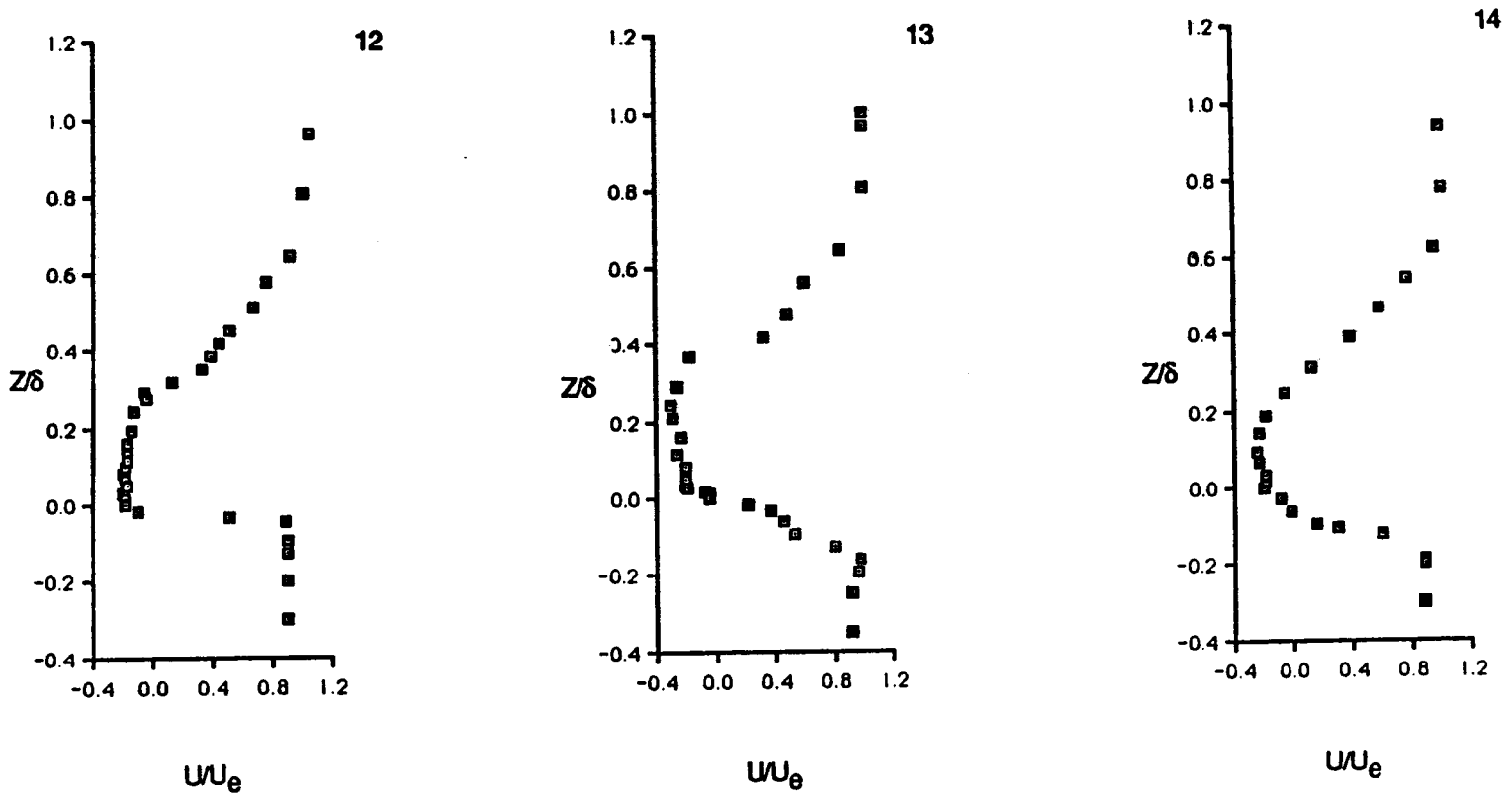

Figure 17.- Continued.

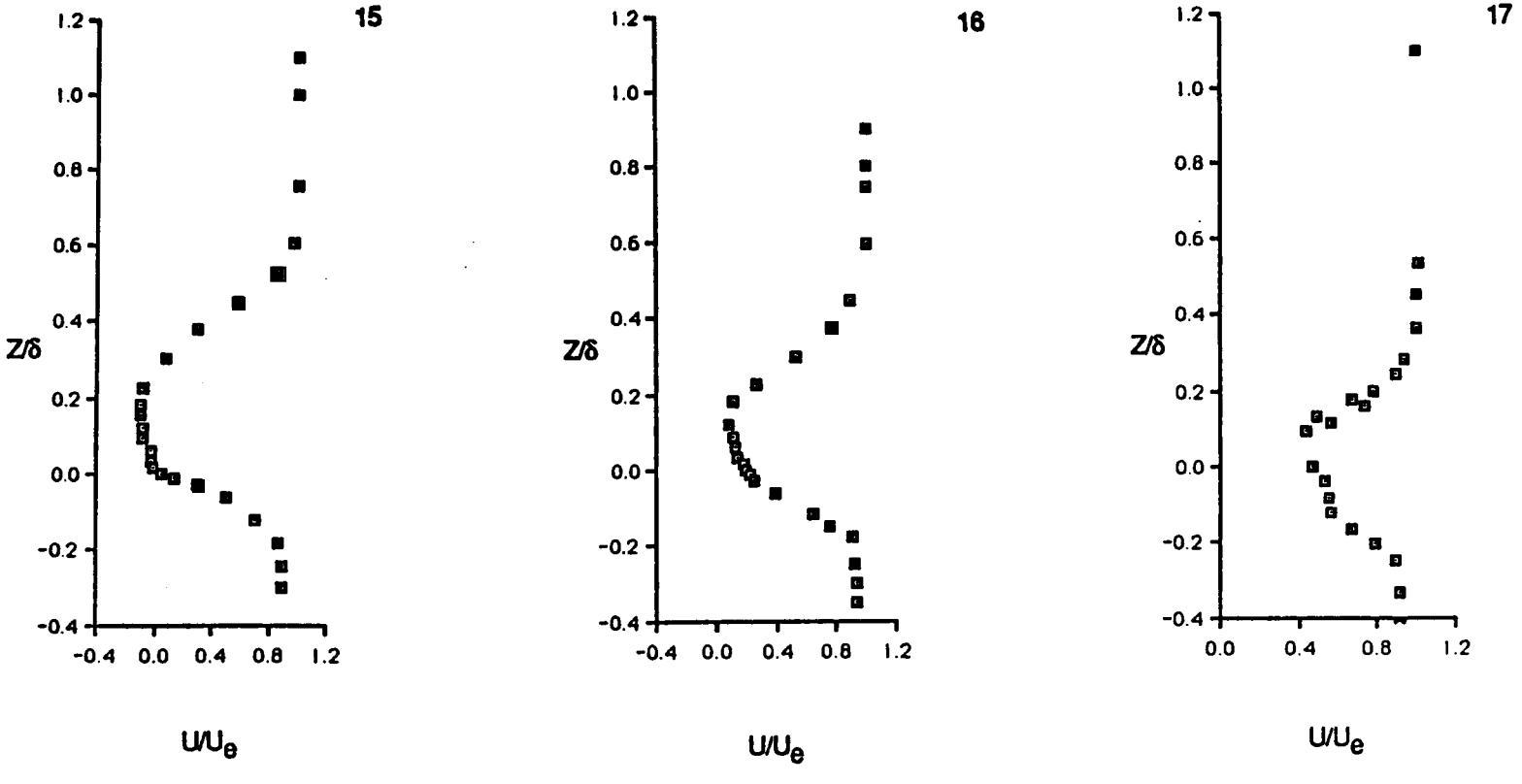

Figure 17.- Continued.

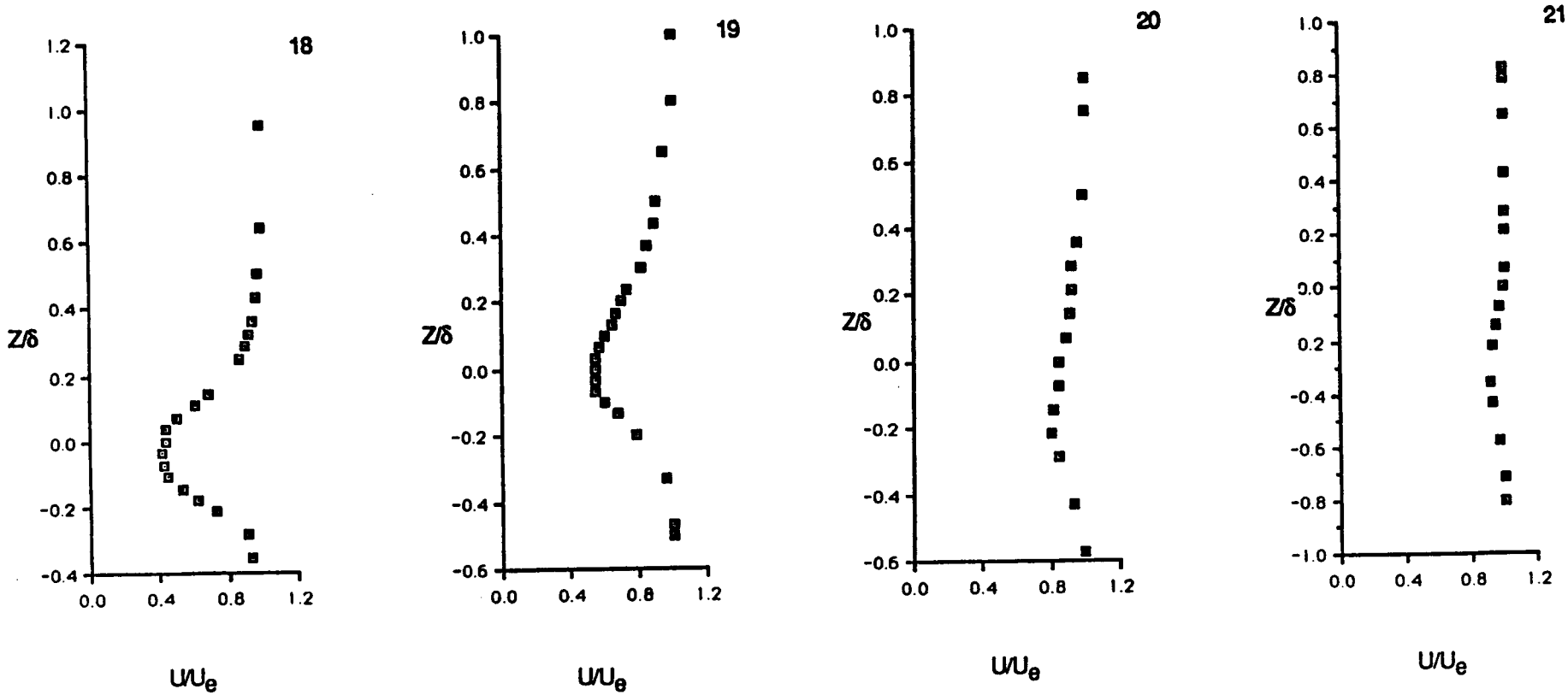

Figure 17.- Concluded.

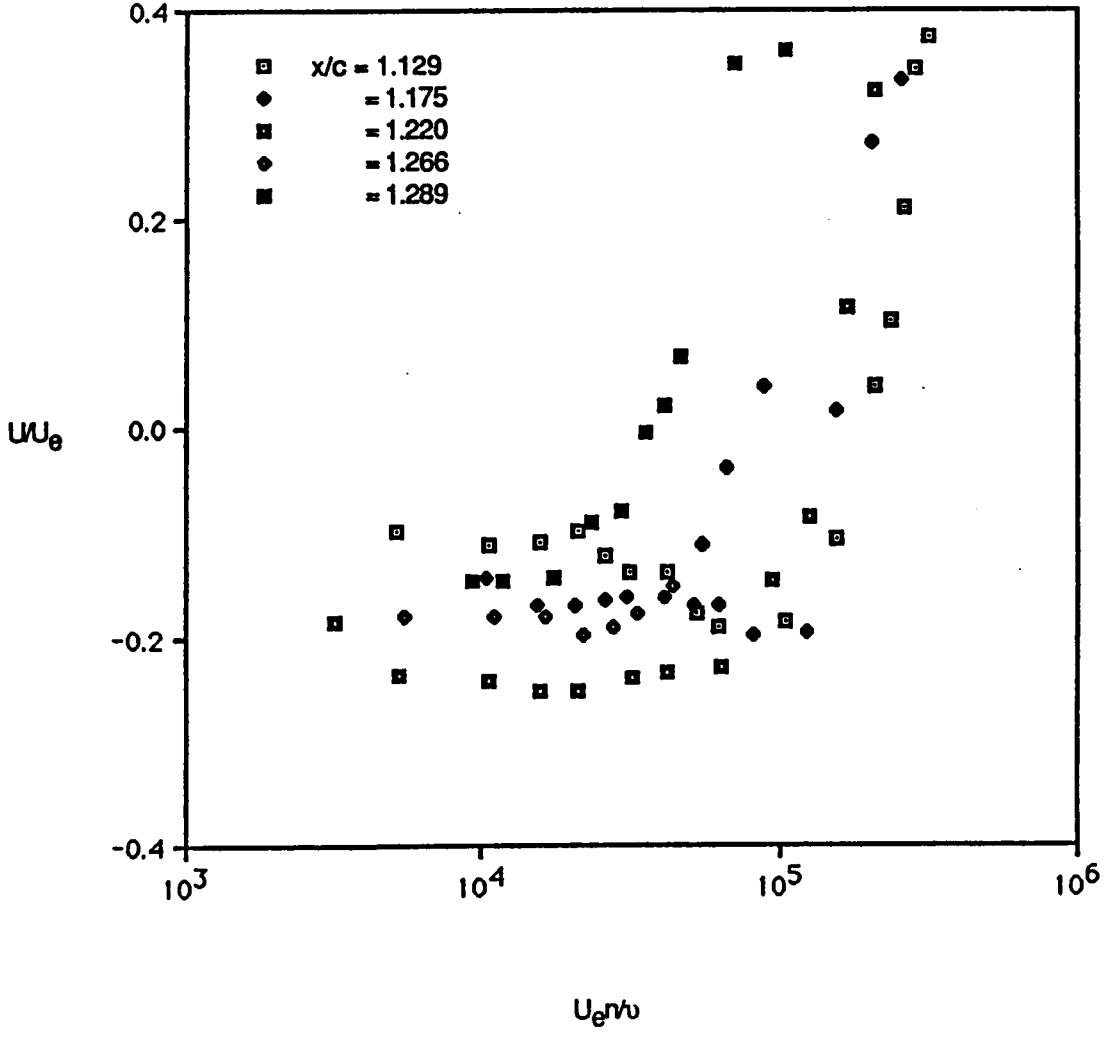

Figure 18.- Near-wall mean velocities in the vicinity of the backflow.

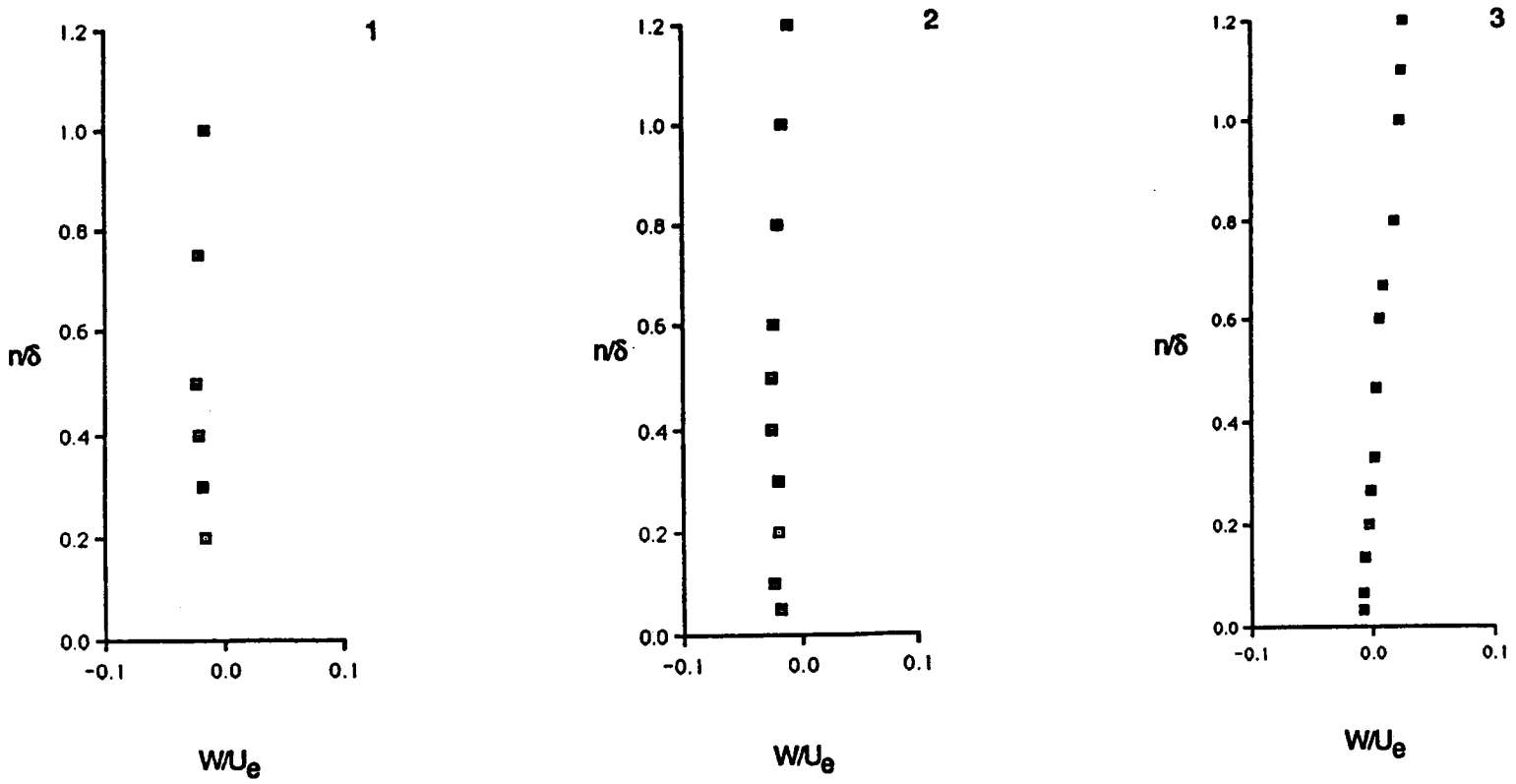

Figure 19.- Distribution of cross-flow mean velocity (station numbers refer to Table 1 and Fig. 5).

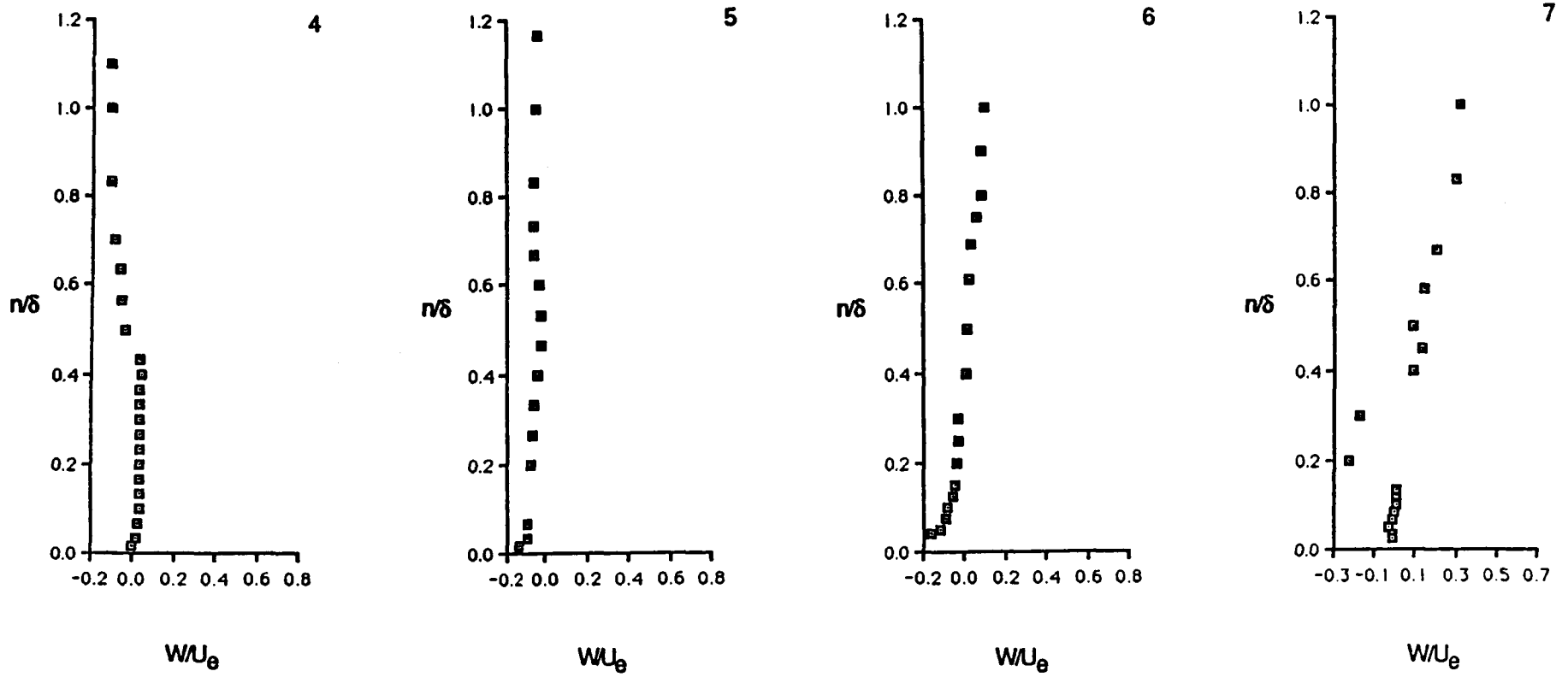

Figure 19.- Continued.

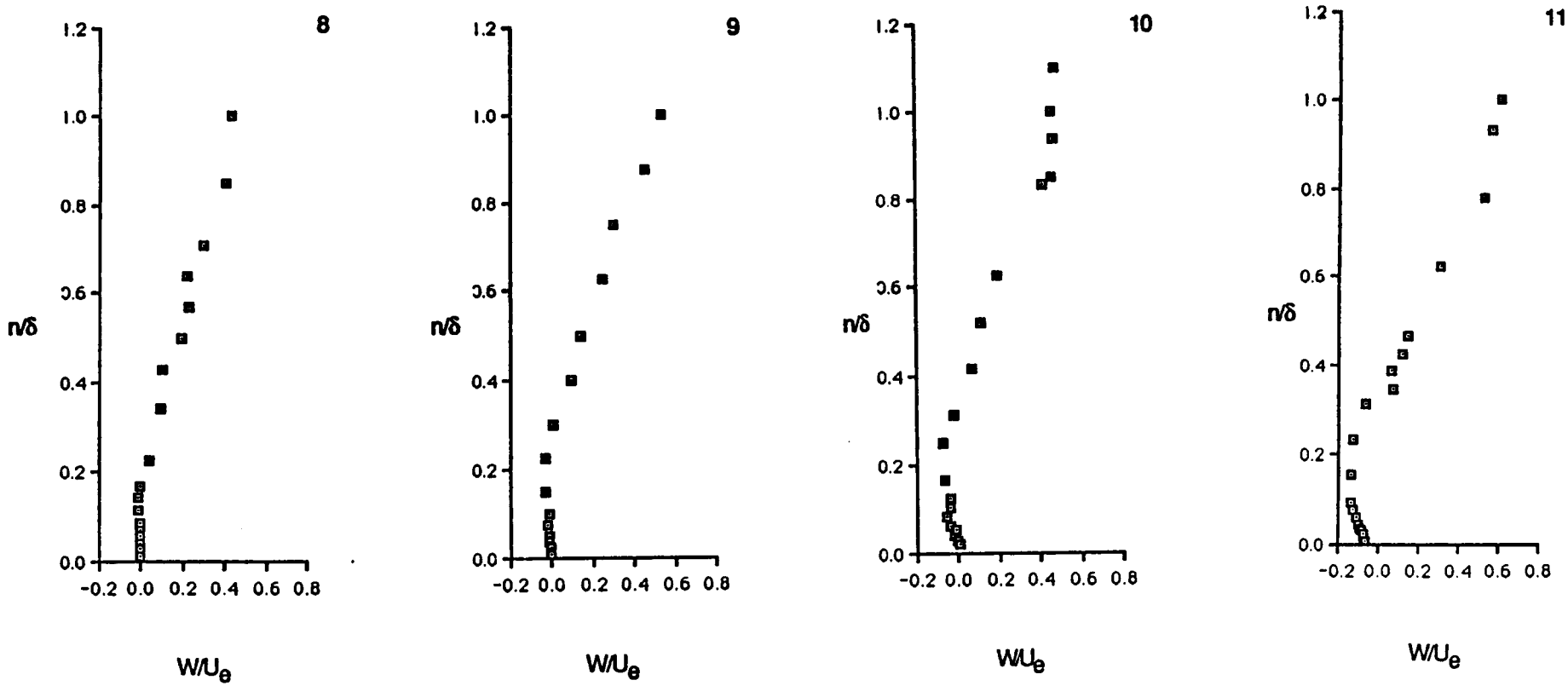

Figure 19.- Continued.

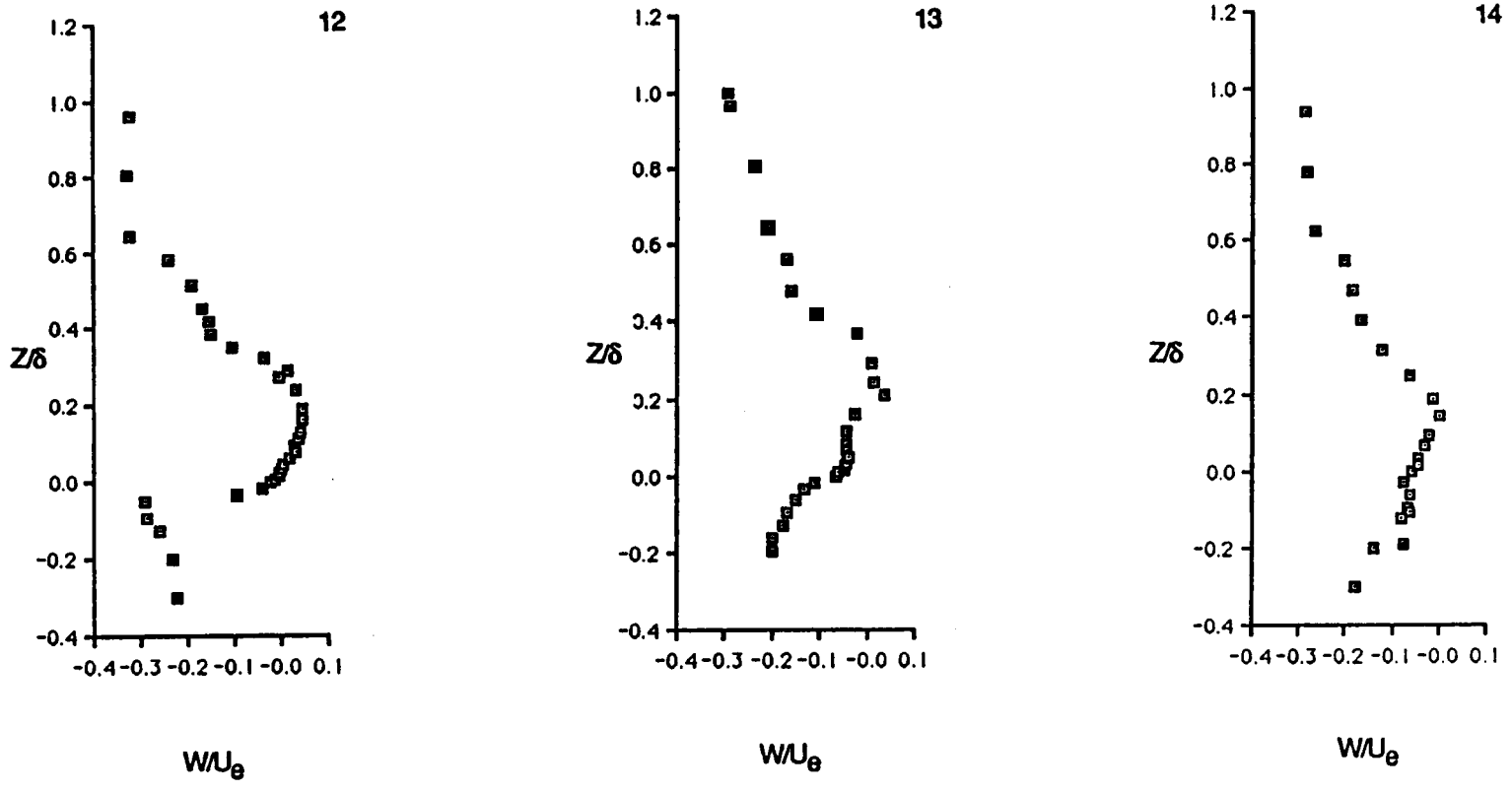

Figure 19.- Continued.

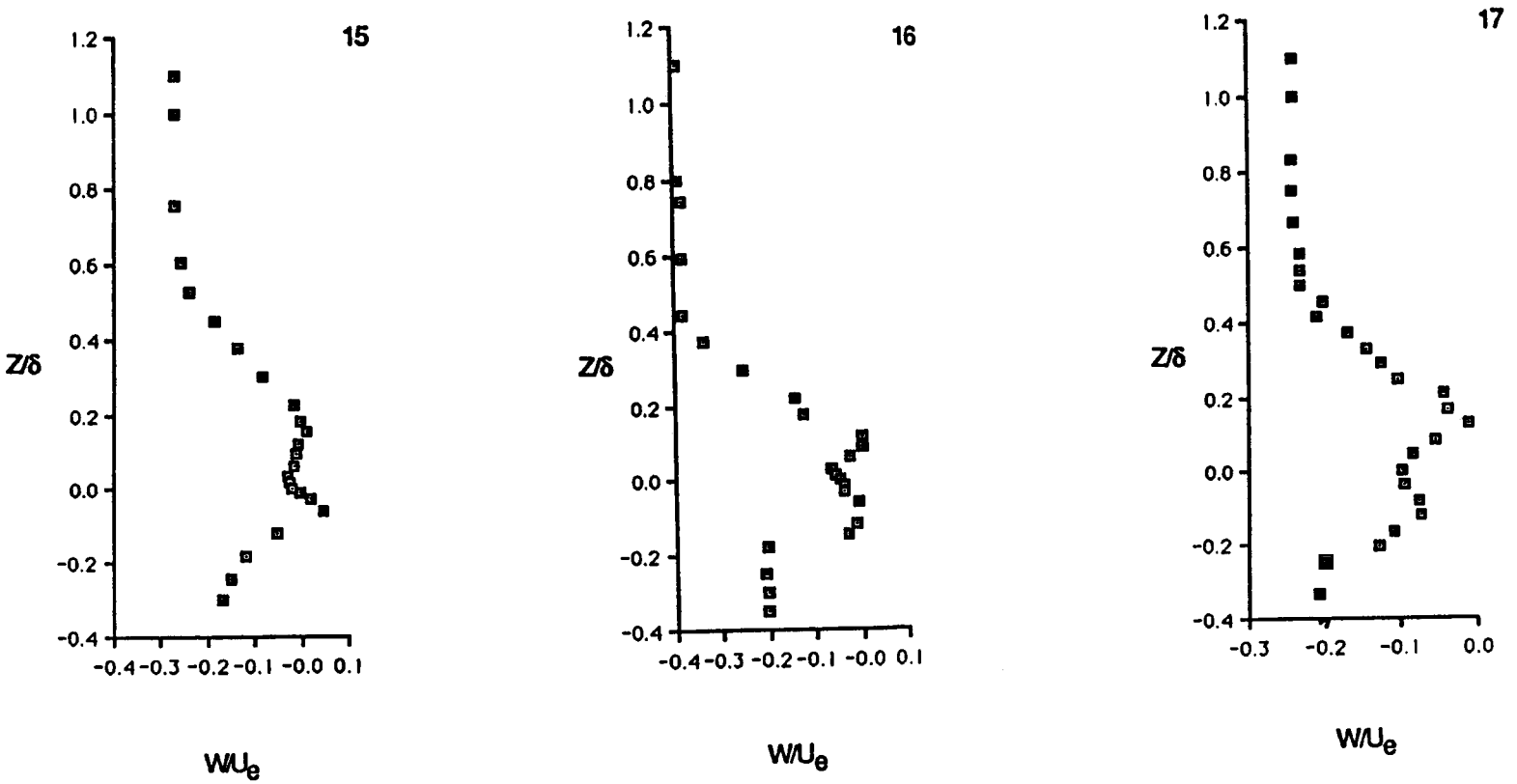

Figure 19.- Continued.

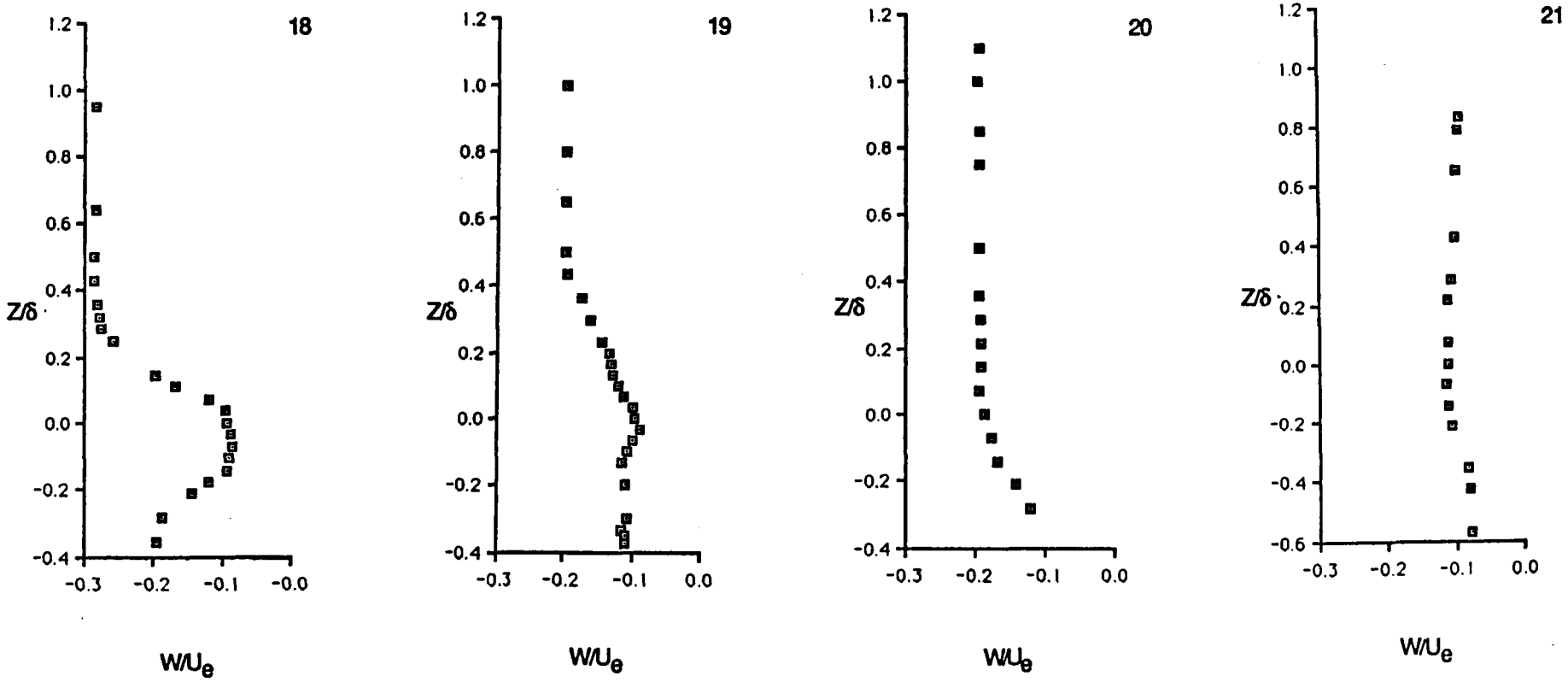

Figure 19.- Concluded.

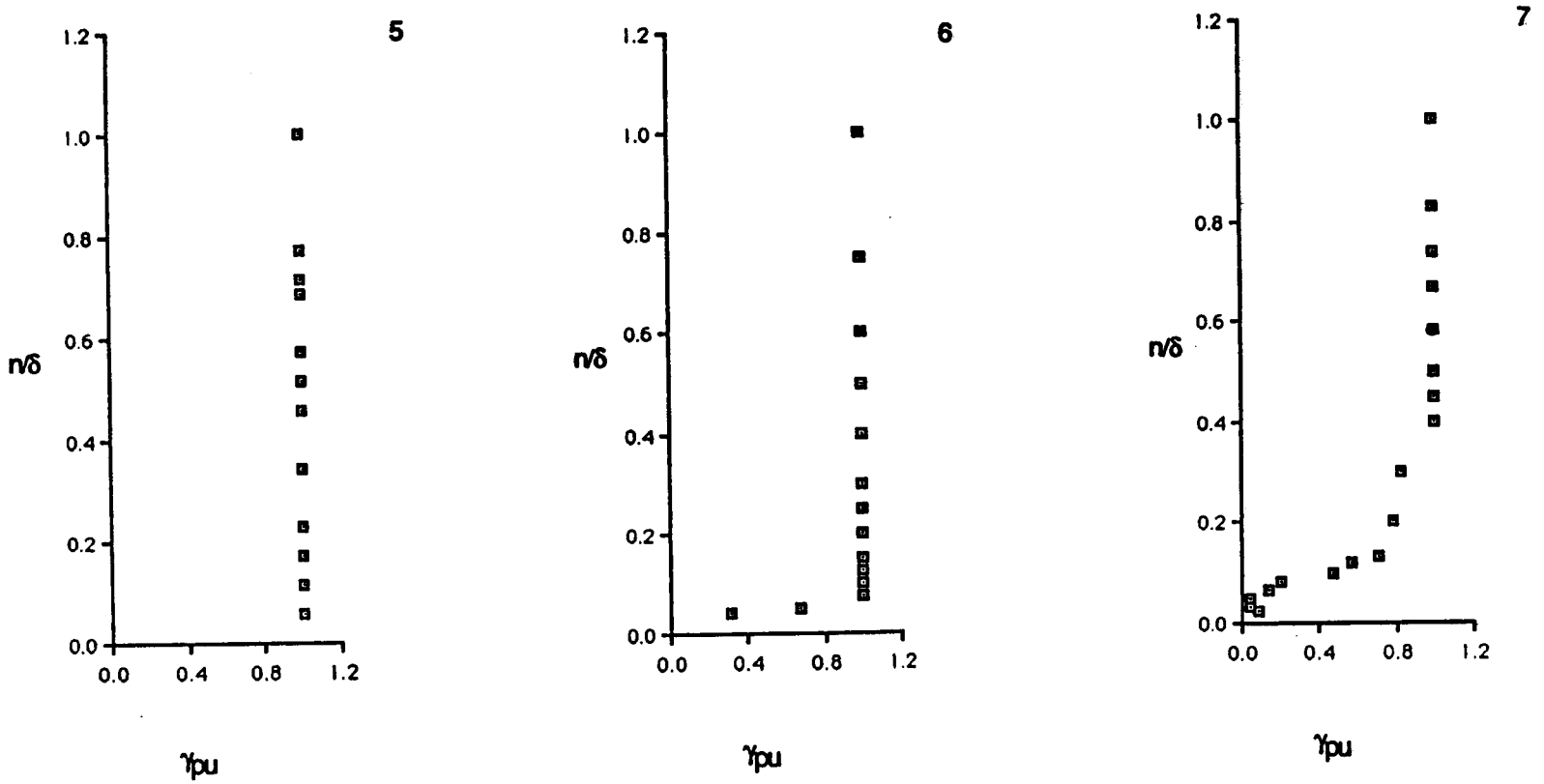

Figure 20.- Probability of positive velocity (station numbers refer to Table 1 and Fig. 5).

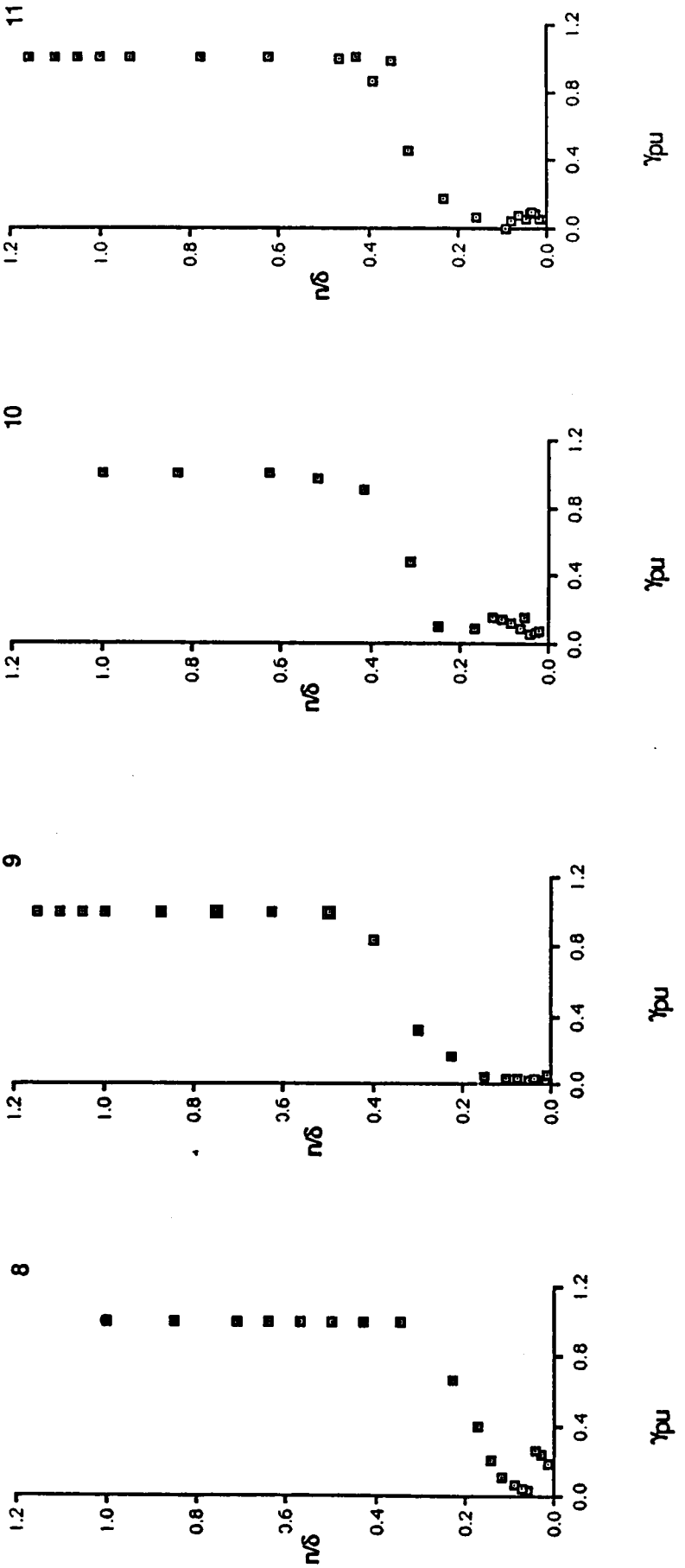

Figure 20.- Continued.

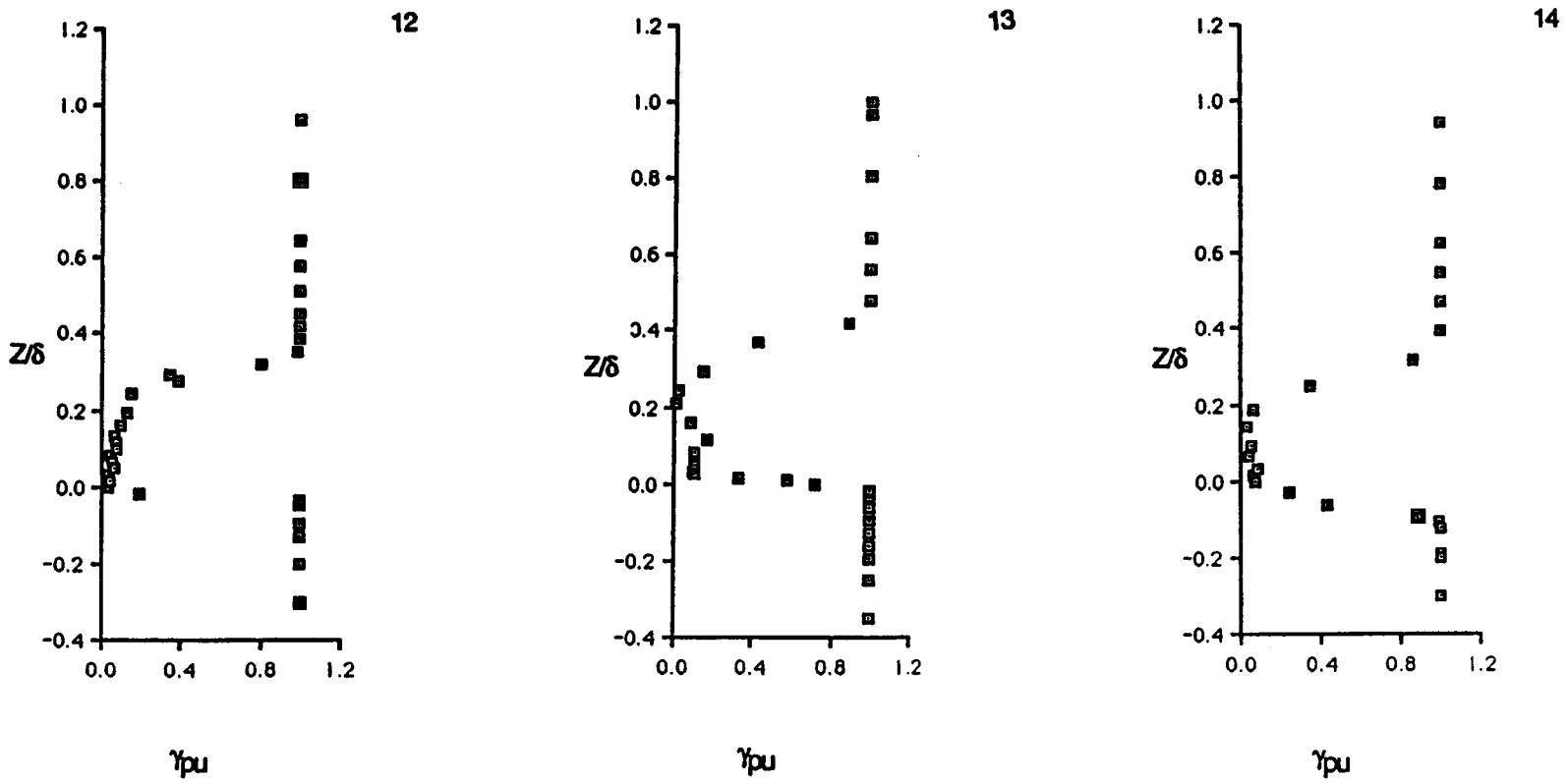

Figure 20.- Continued.

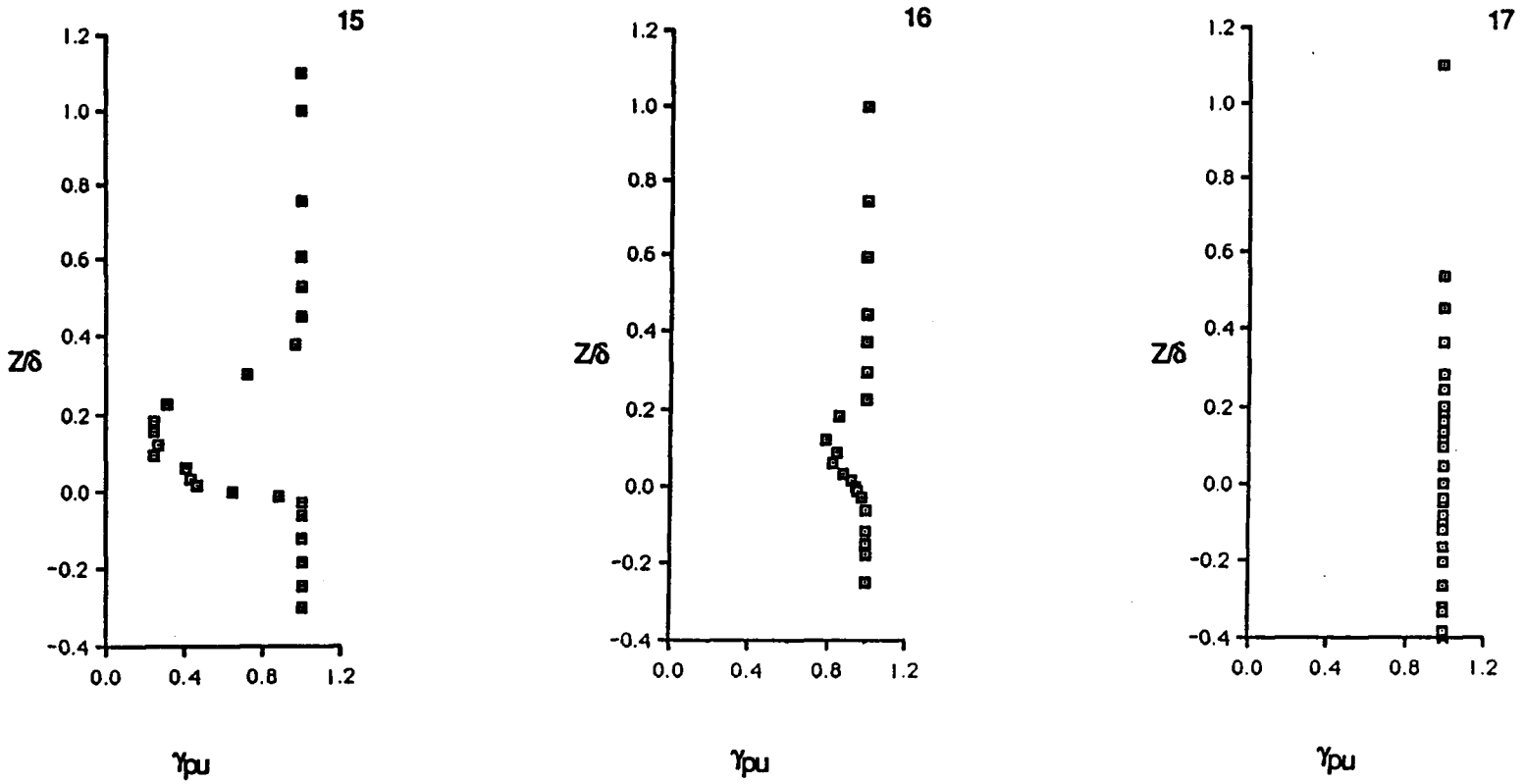

Figure 20.- Concluded.

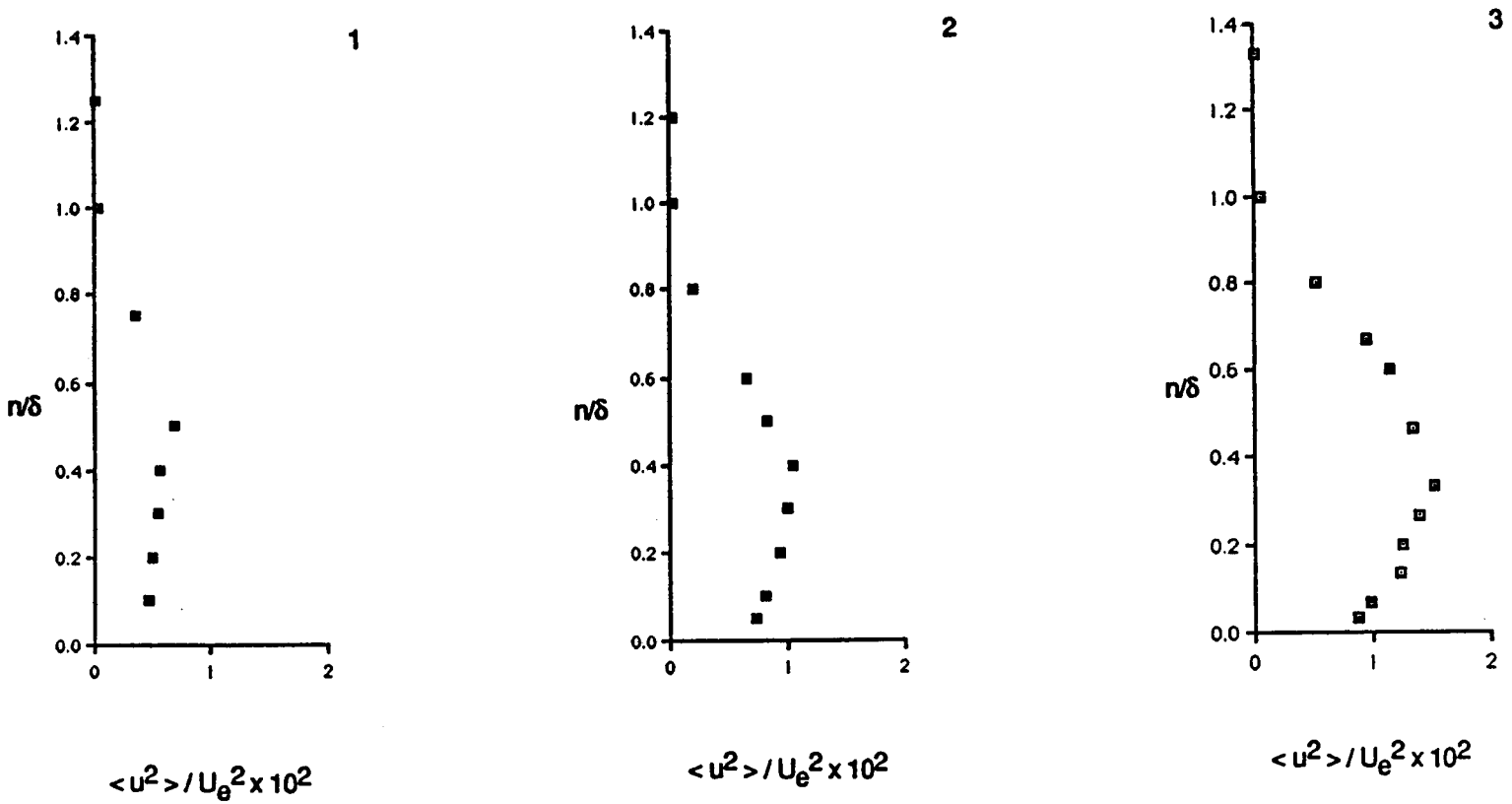

Figure 21.- Distribution of Reynolds normal stresses (station numbers refer to Table 1 and Fig. 5).

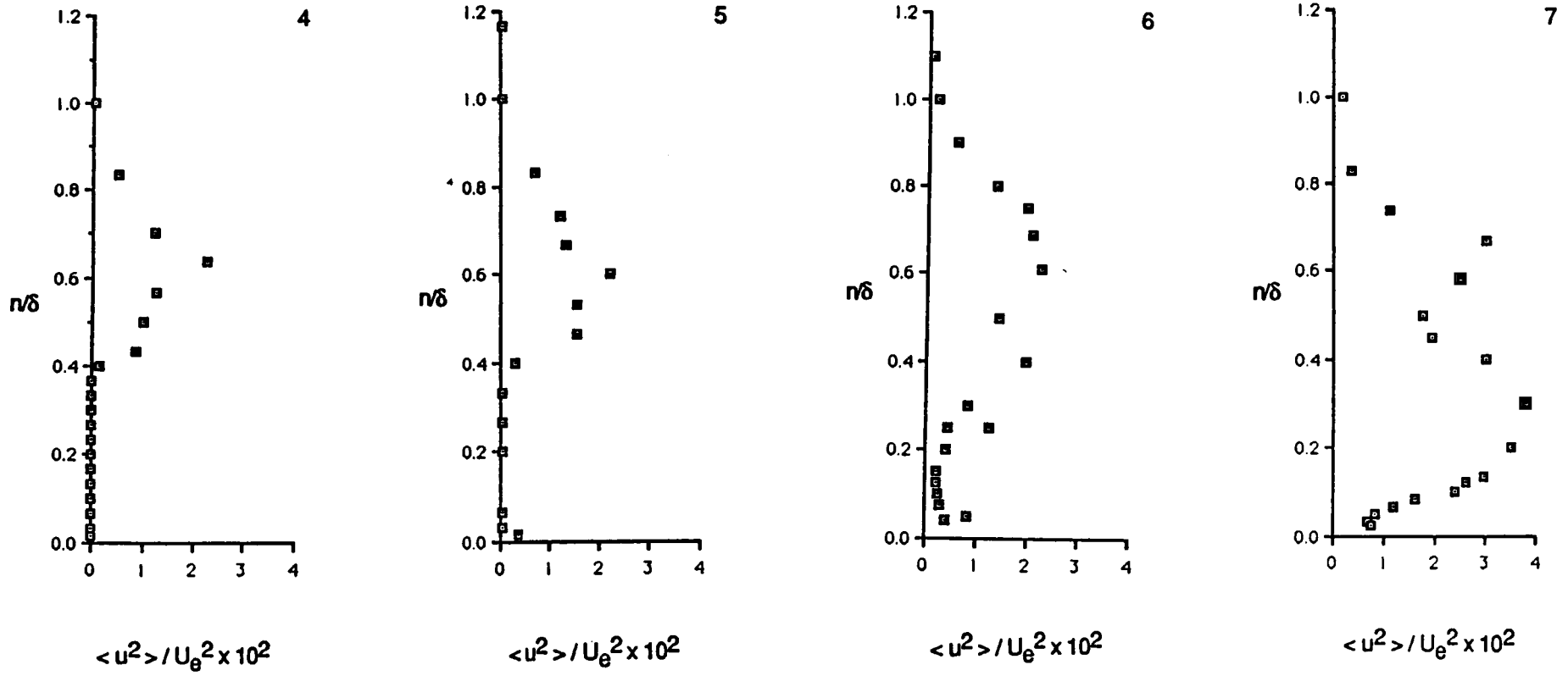

Figure 21.- Continued.

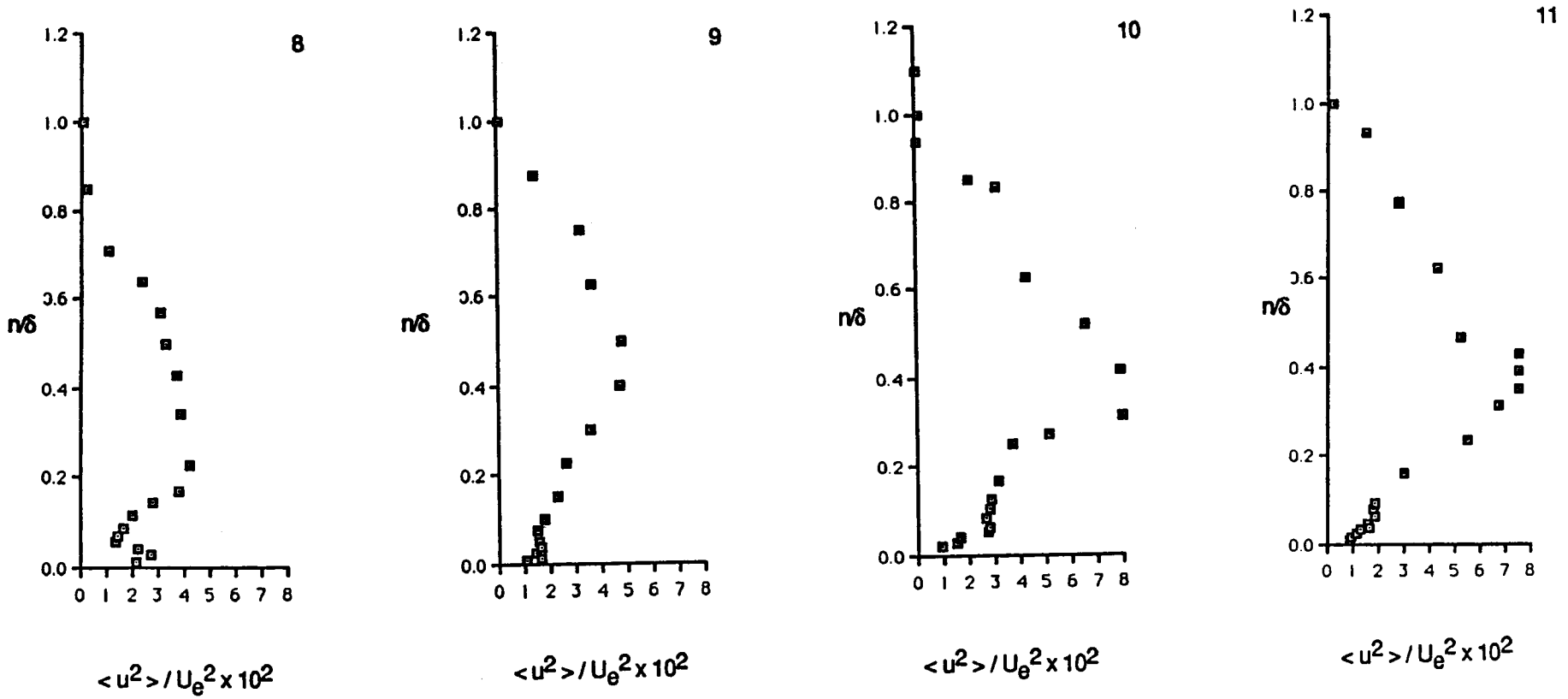

Figure 21.- Continued.

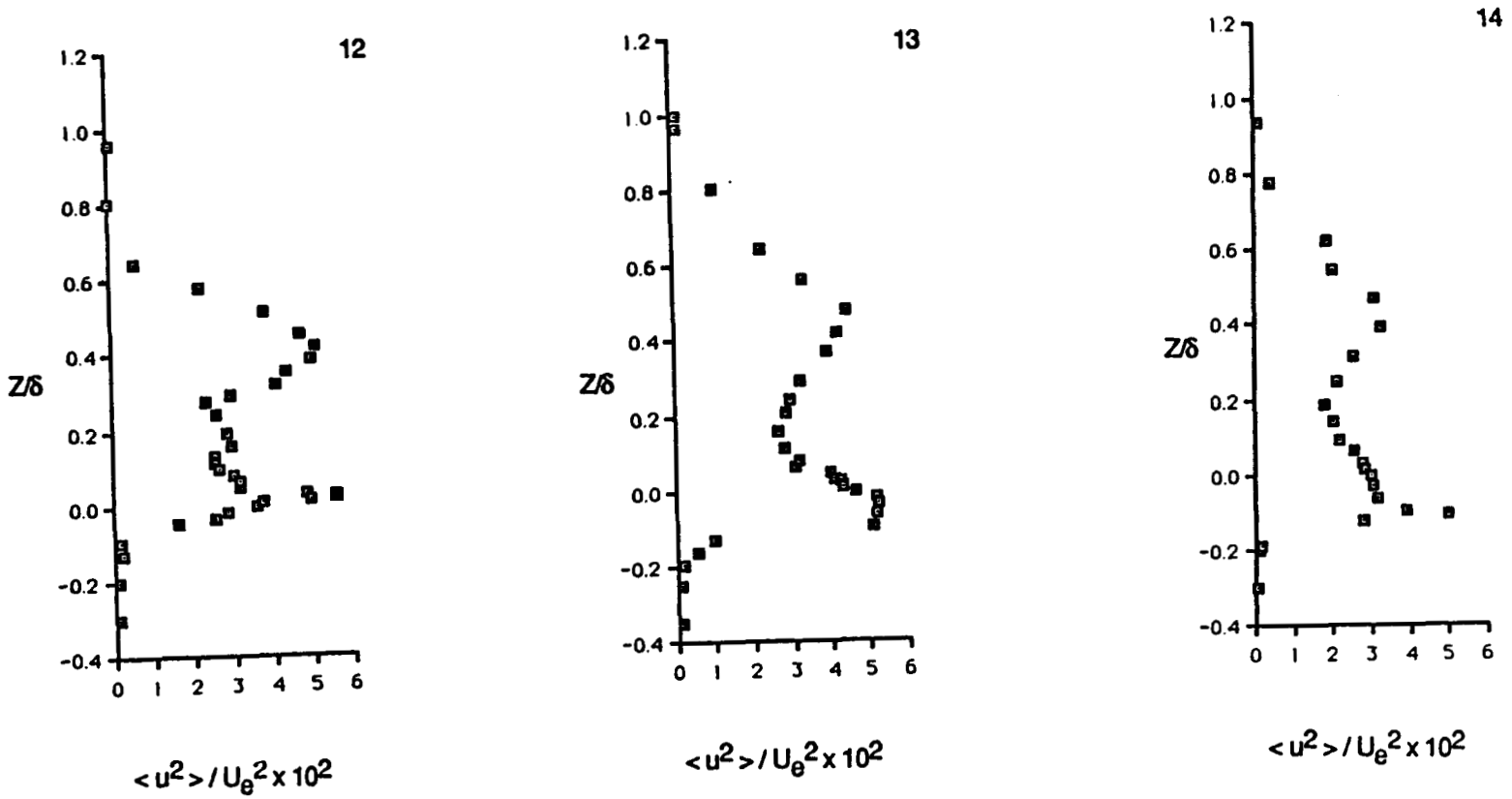

Figure 21.- Continued.

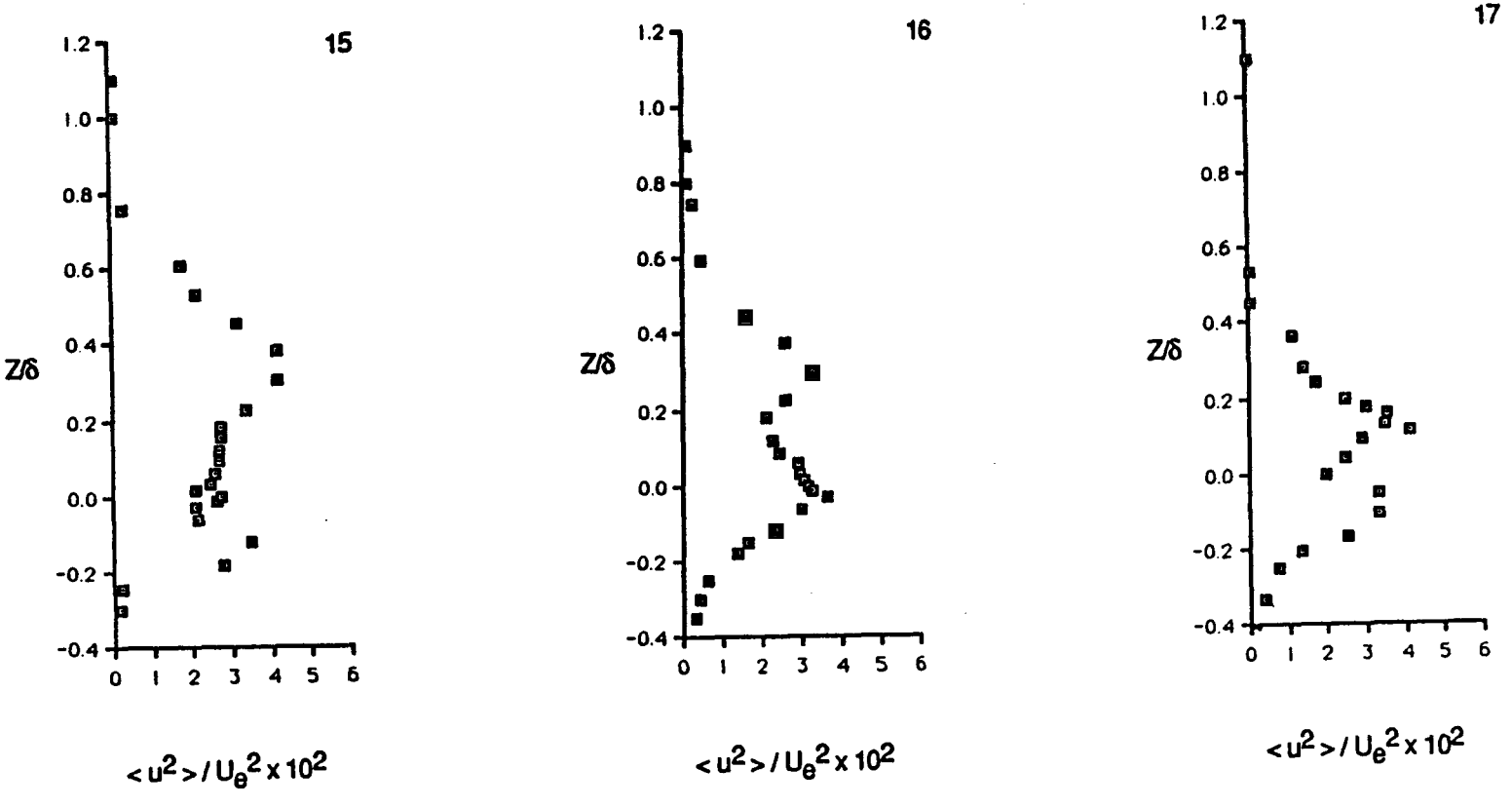

Figure 21.- Continued.

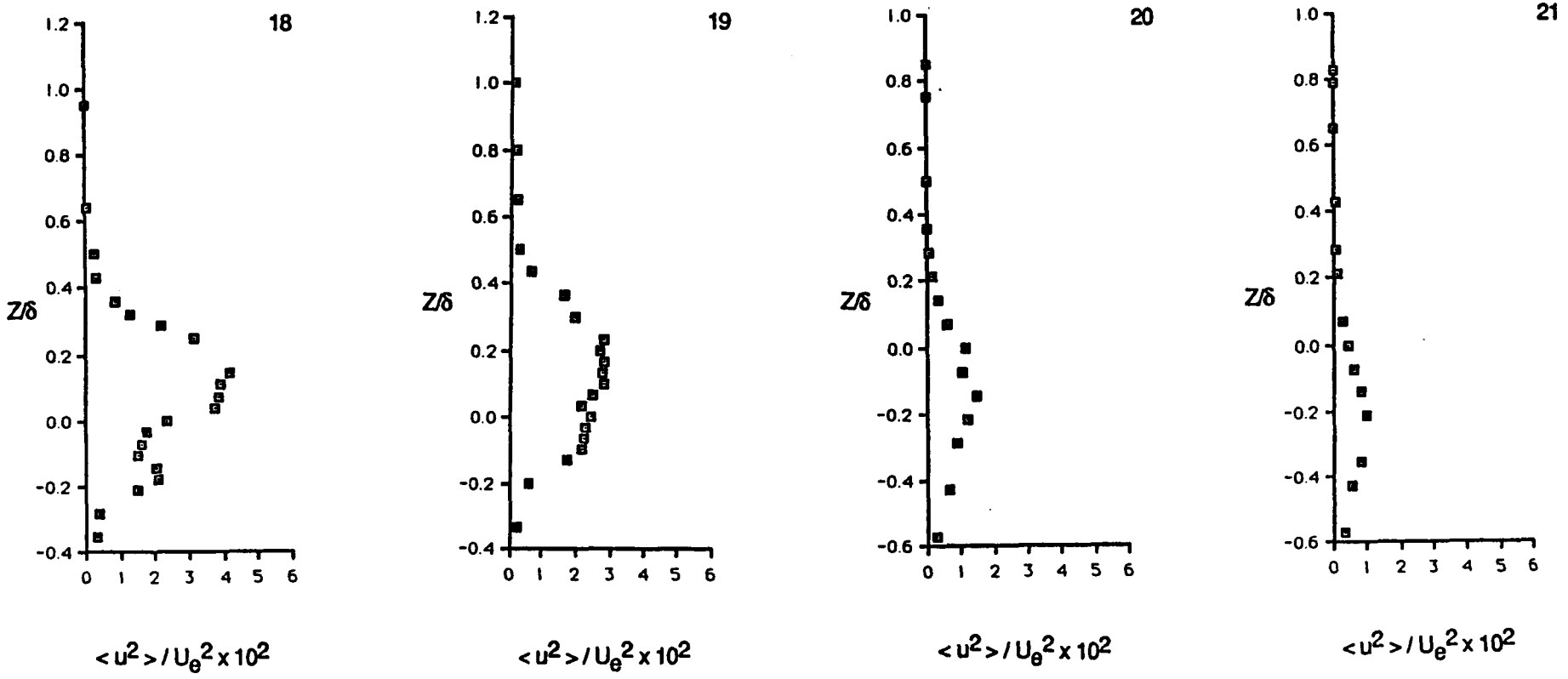

Figure 21.- Concluded.

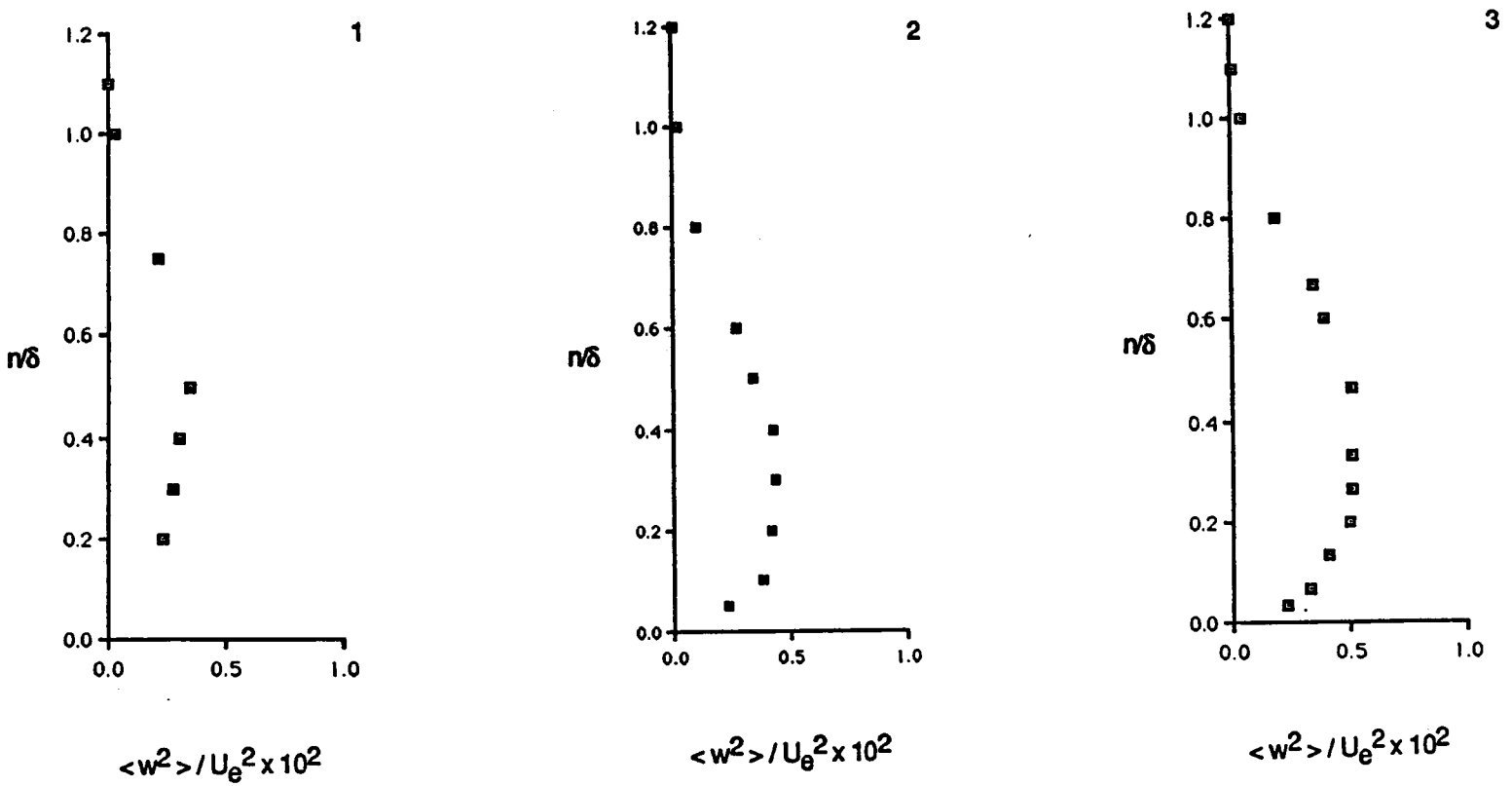

Figure 22.- Distribution of Reynolds normal stresses (station numbers refer to Table 1 and Fig. 5).

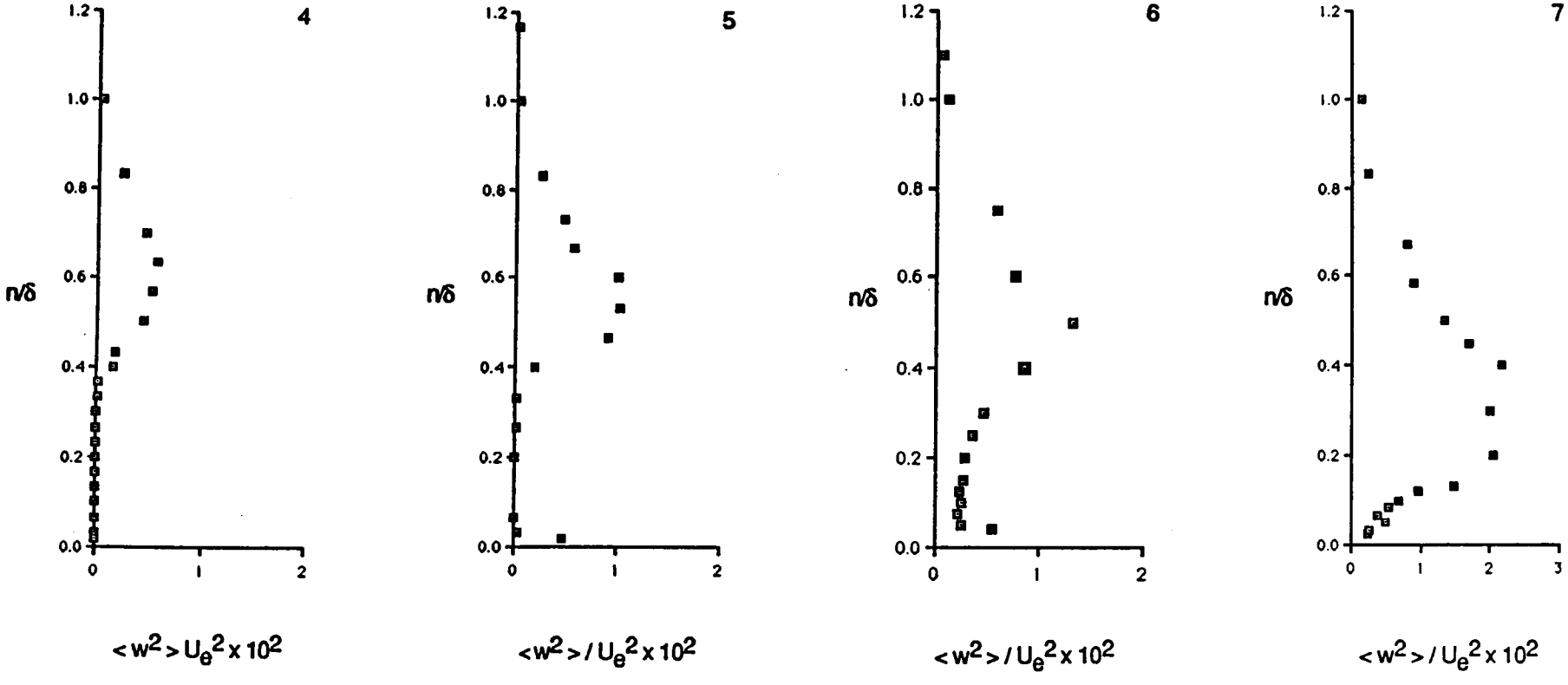

Figure 22.- Continued.

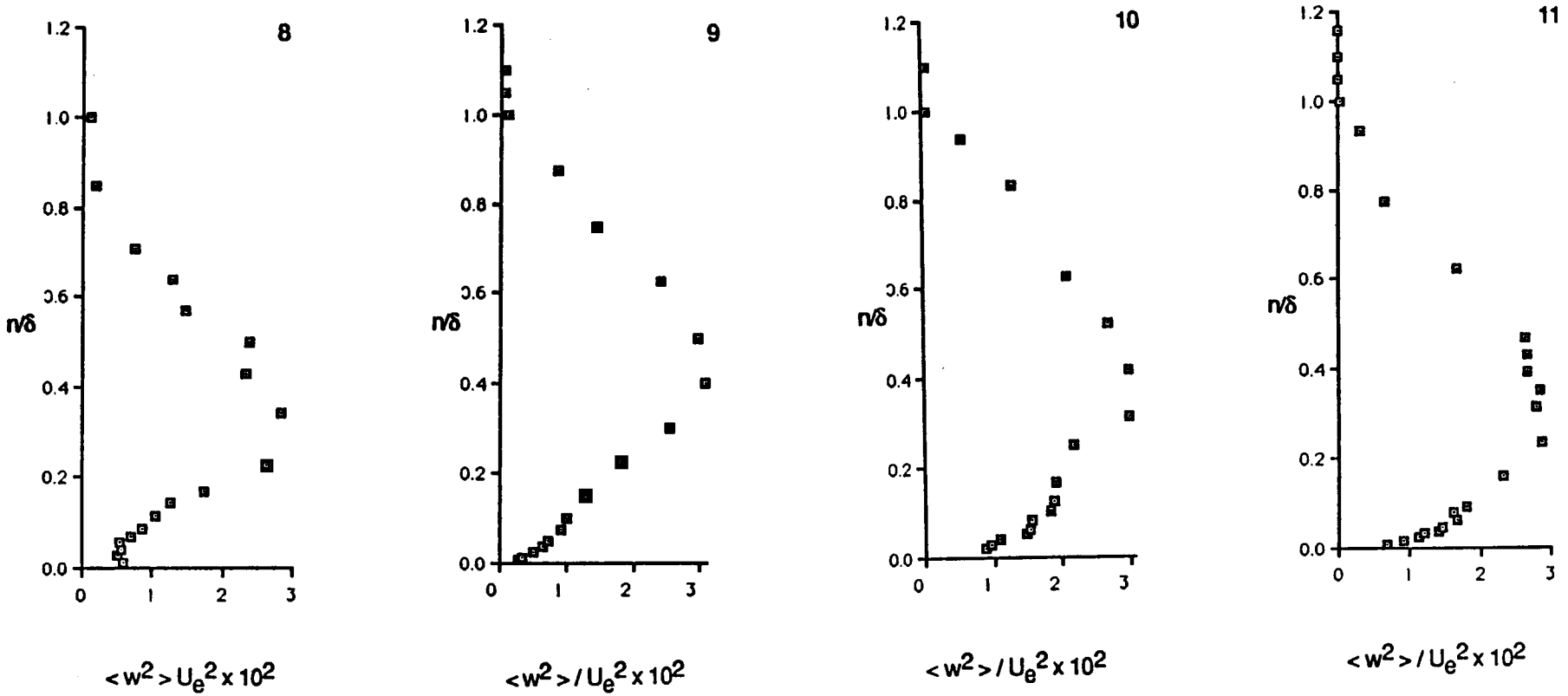

Figure 22.- Continued.

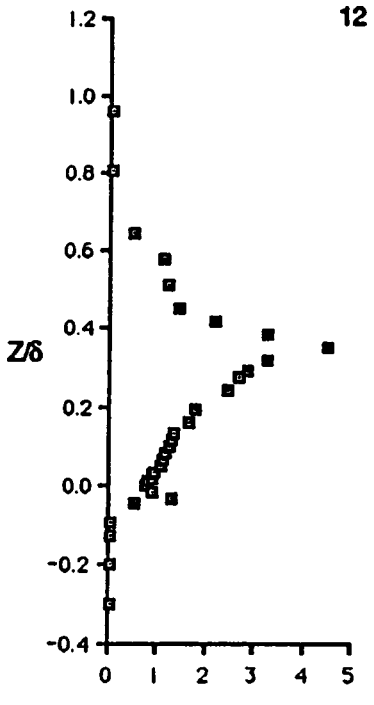

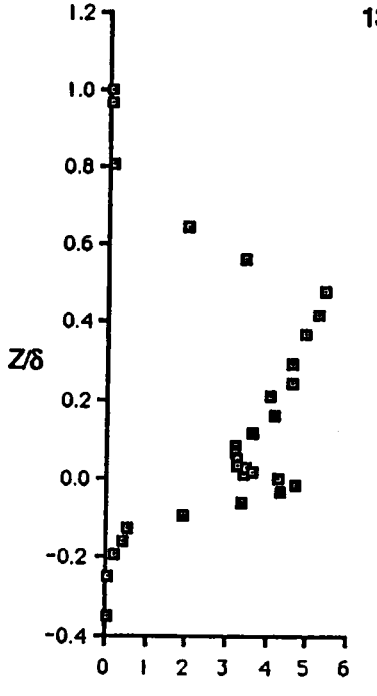

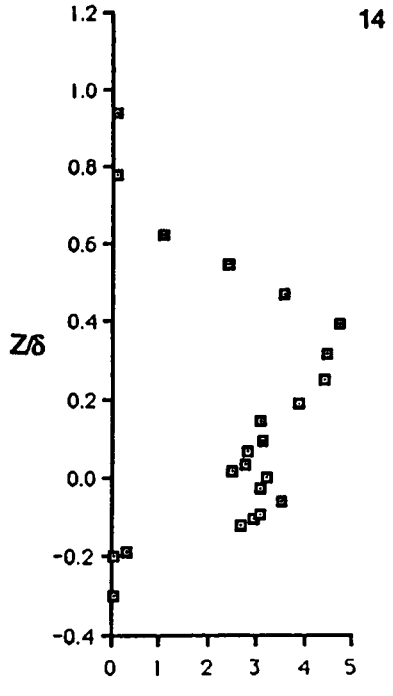

Figure 22.- Continued.

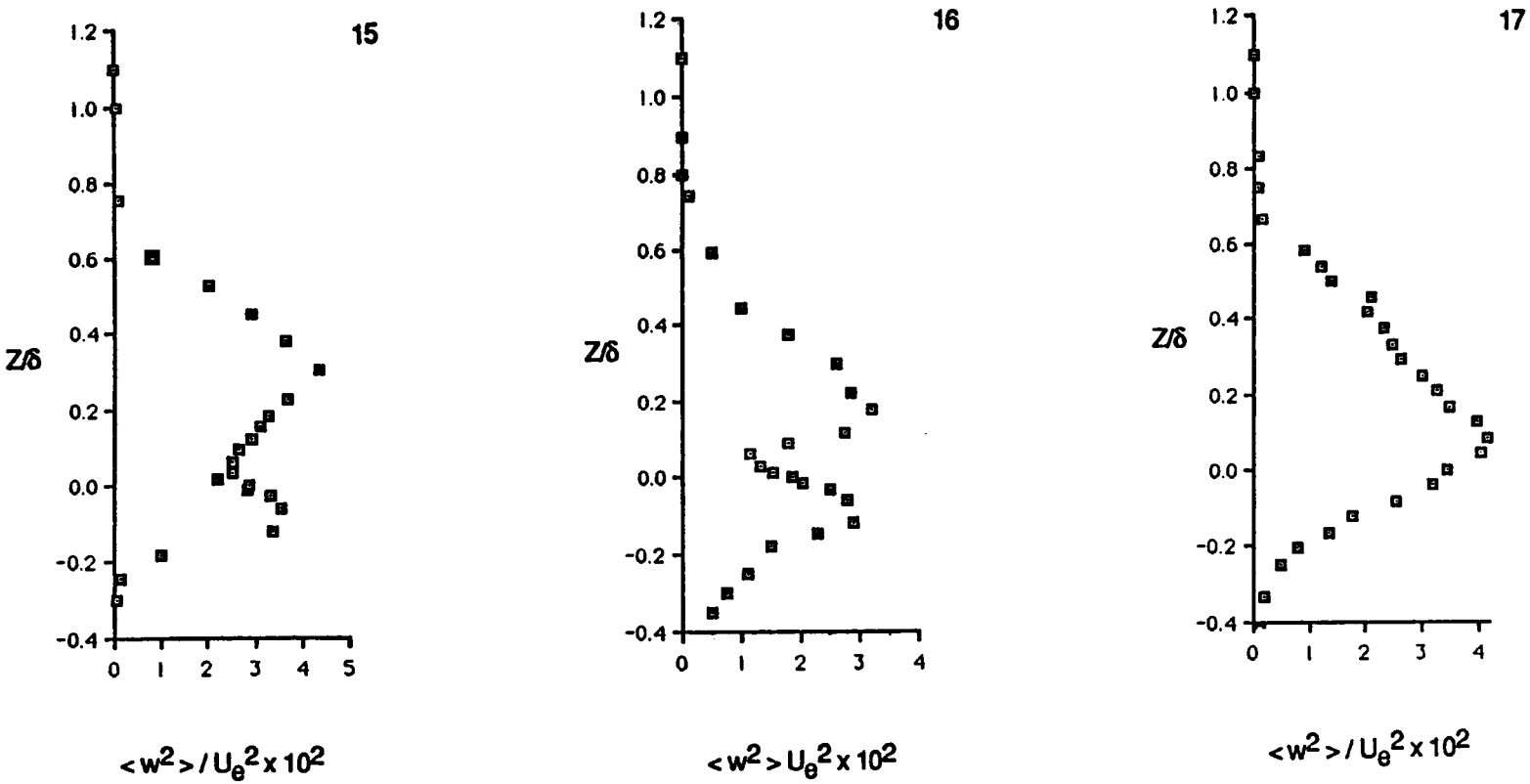

Figure 22.- Continued.

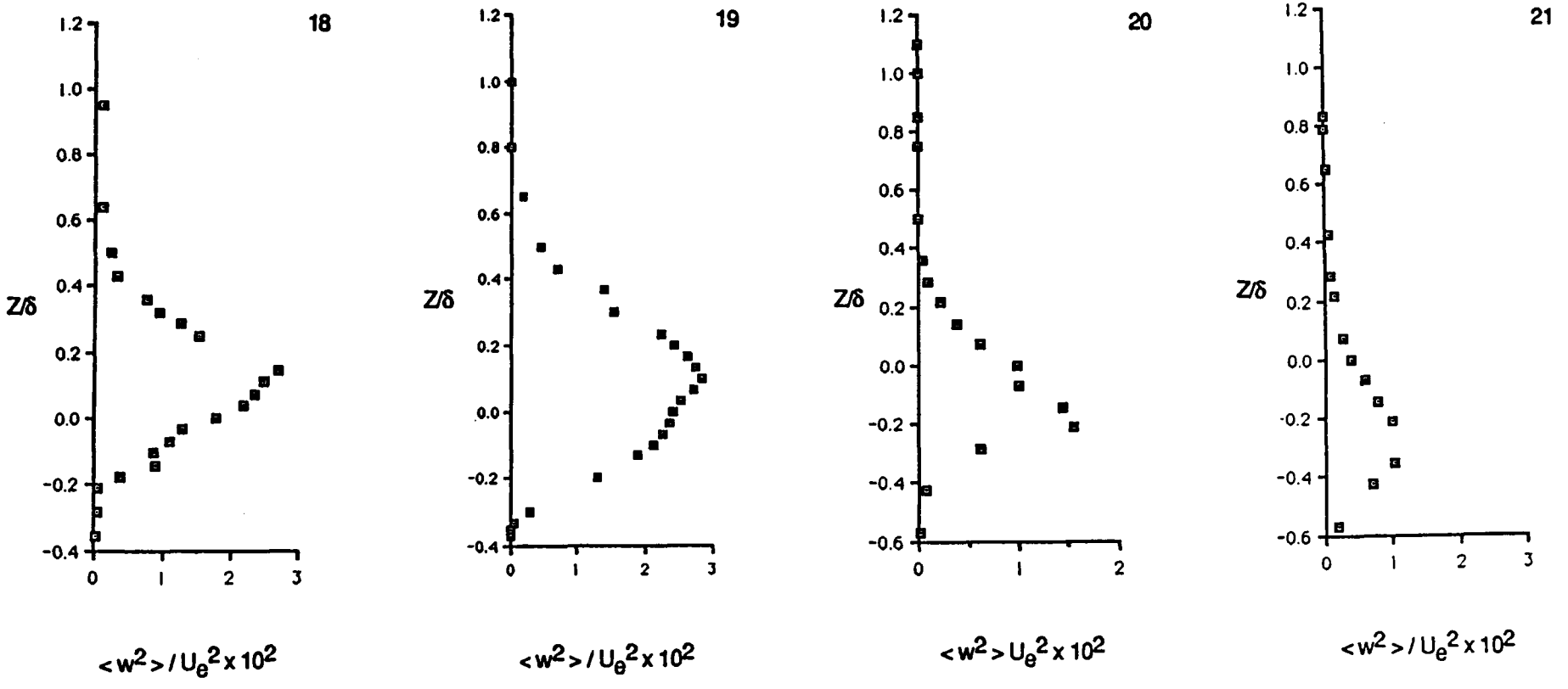

Figure 22.- Concluded.

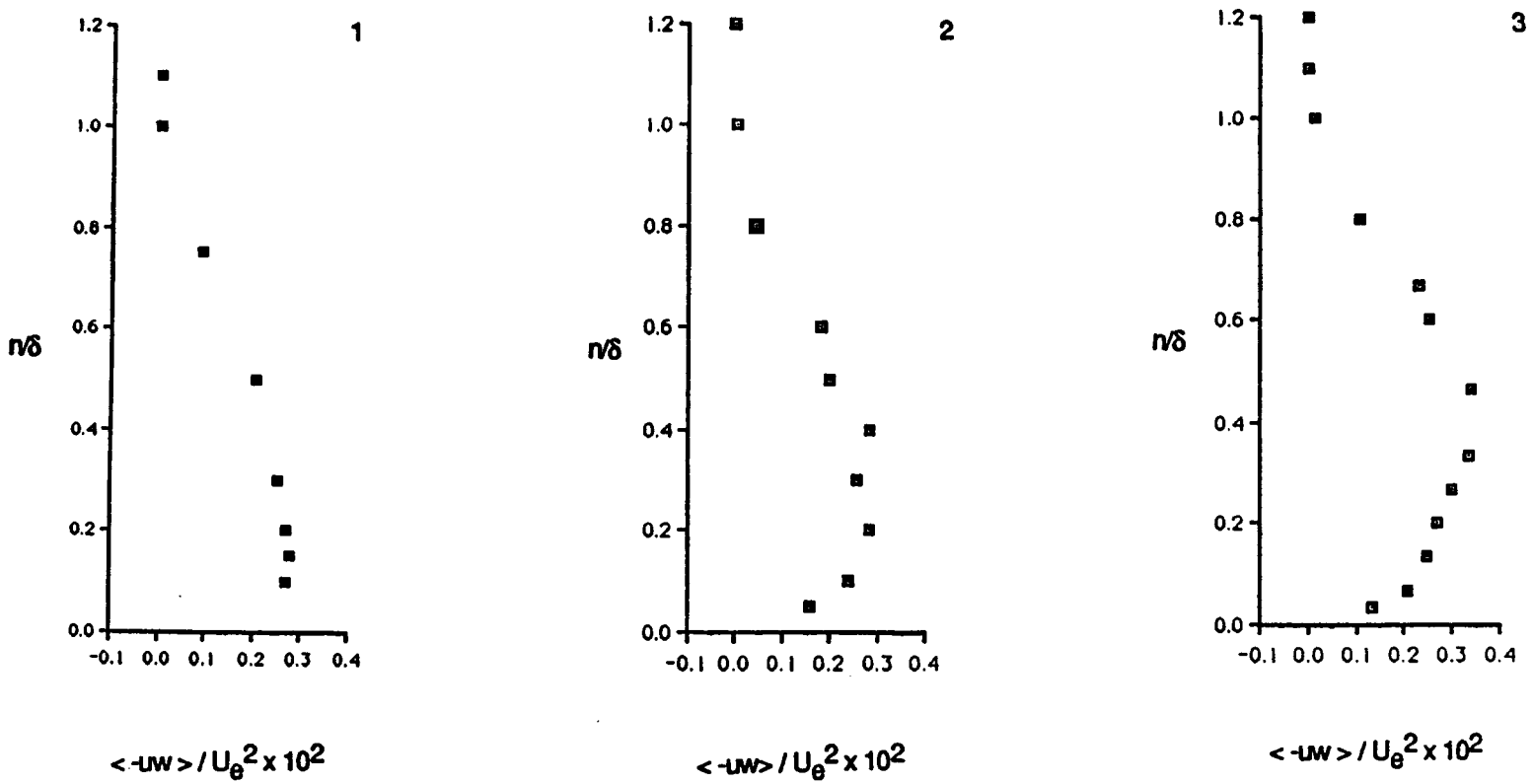

Figure 23.- Distribution of Reynolds shear stresses (station numbers refer to Table 1 and Fig. 5).

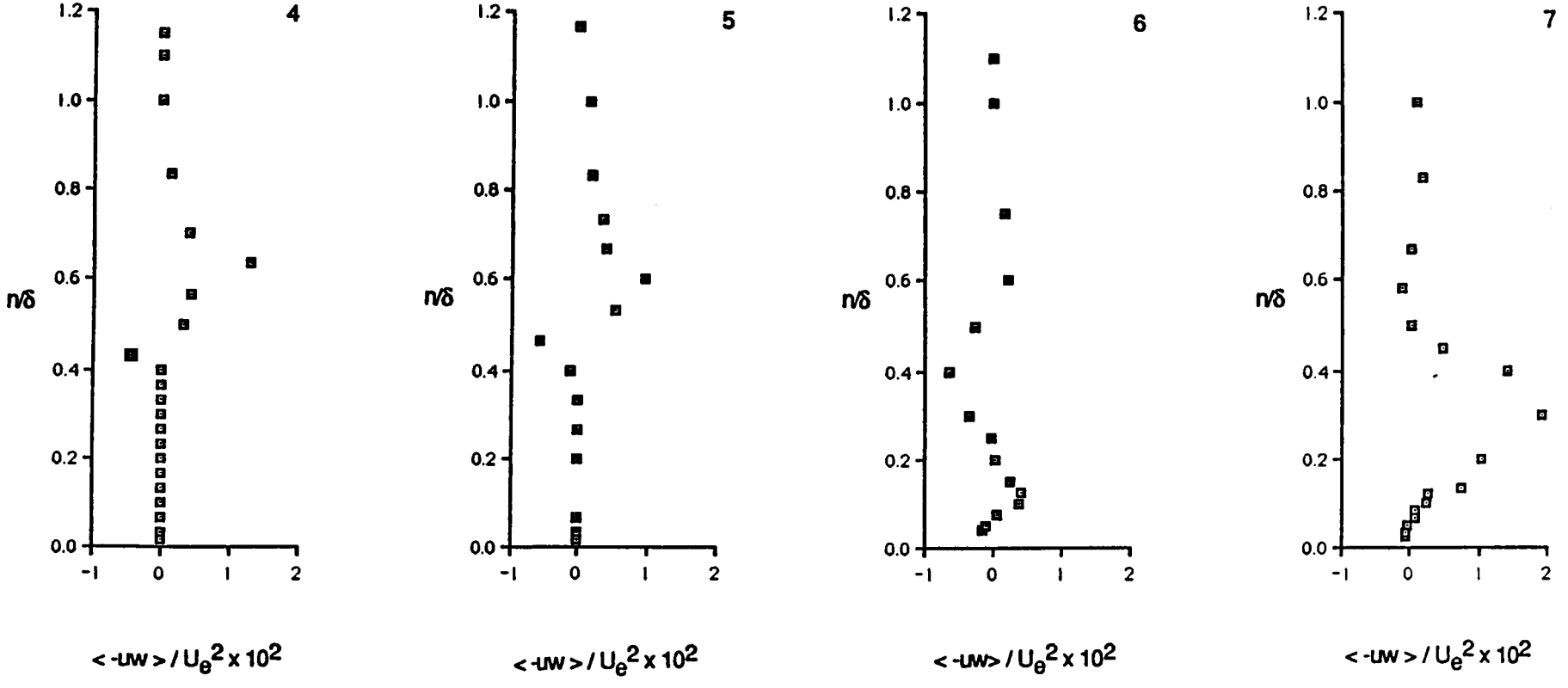

Figure 23.- Continued.

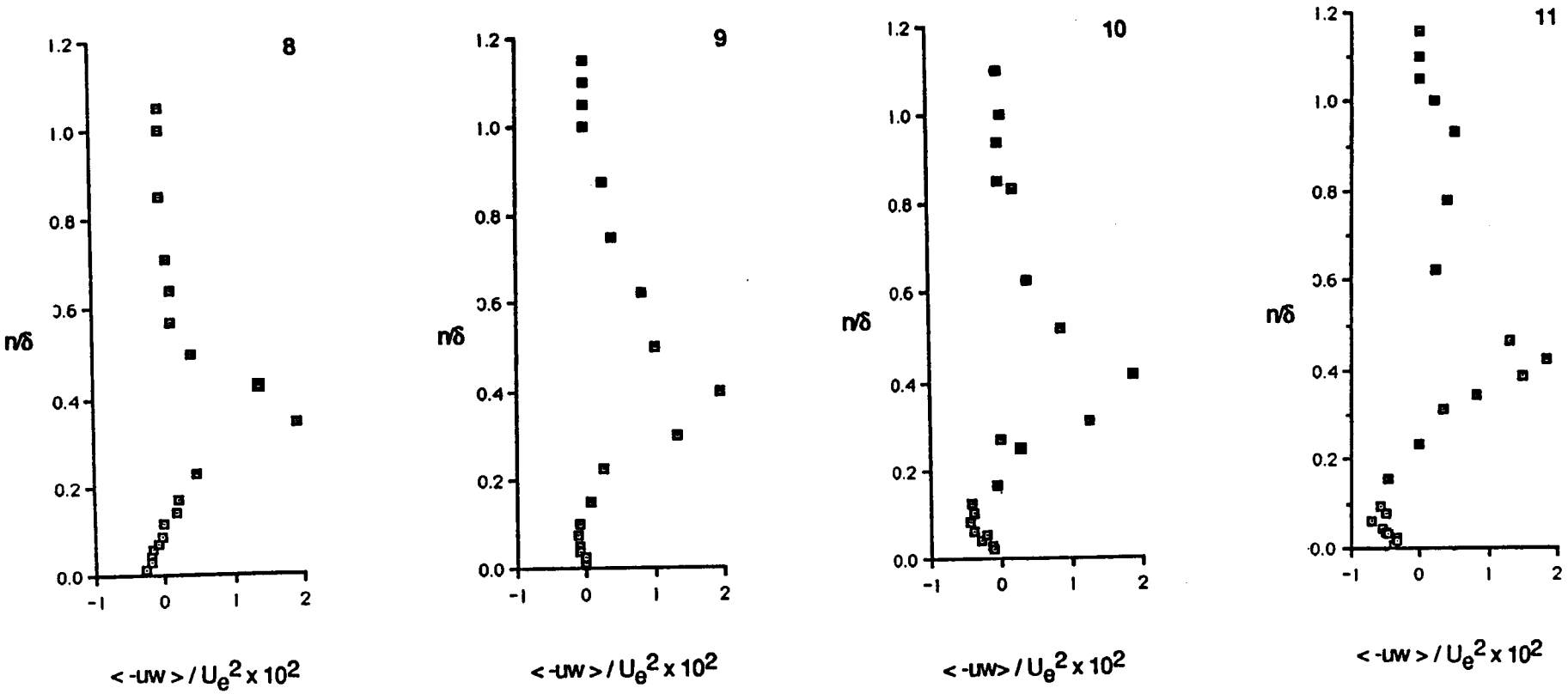

Figure 23.- Continued.

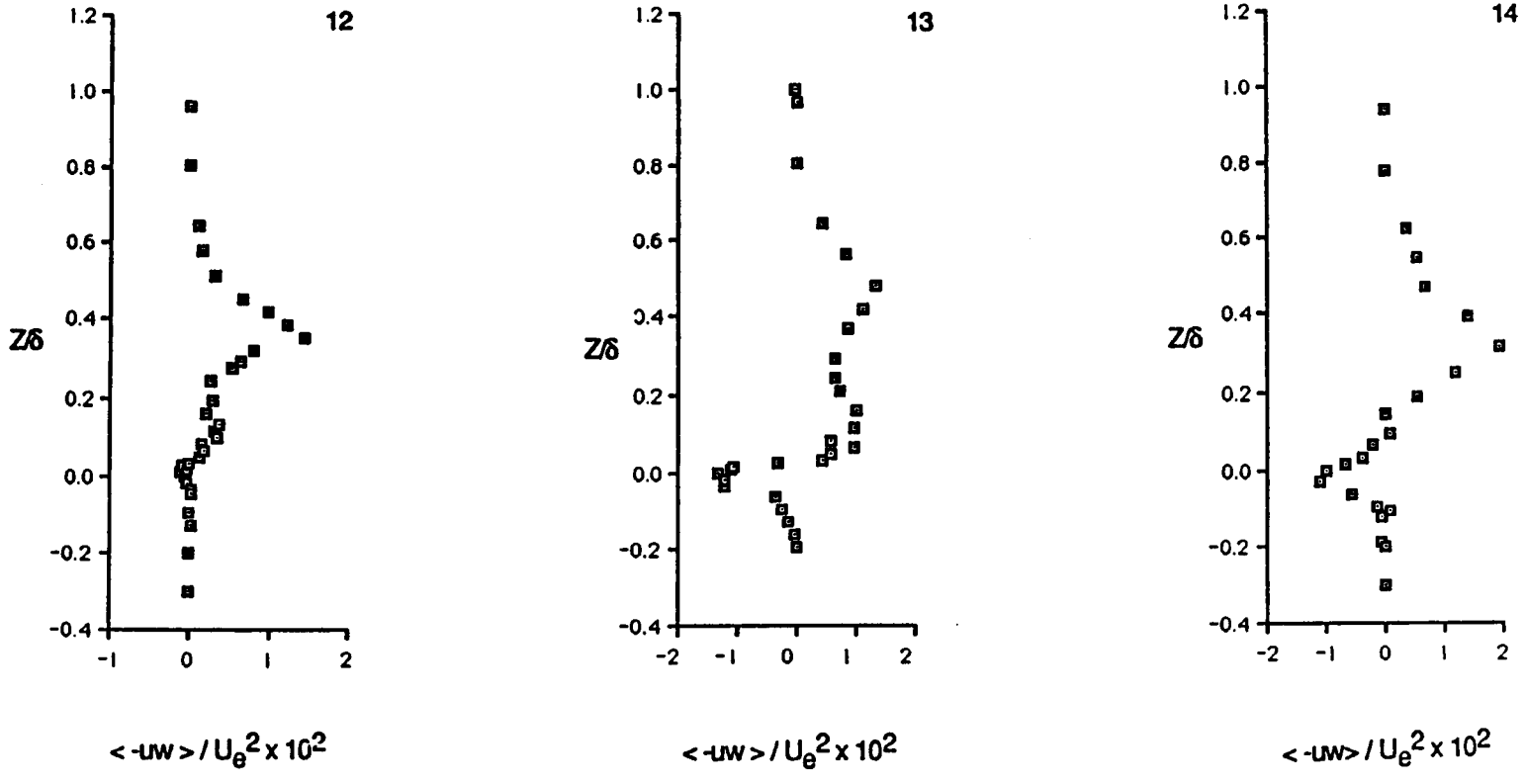

Figure 23.- Continued.

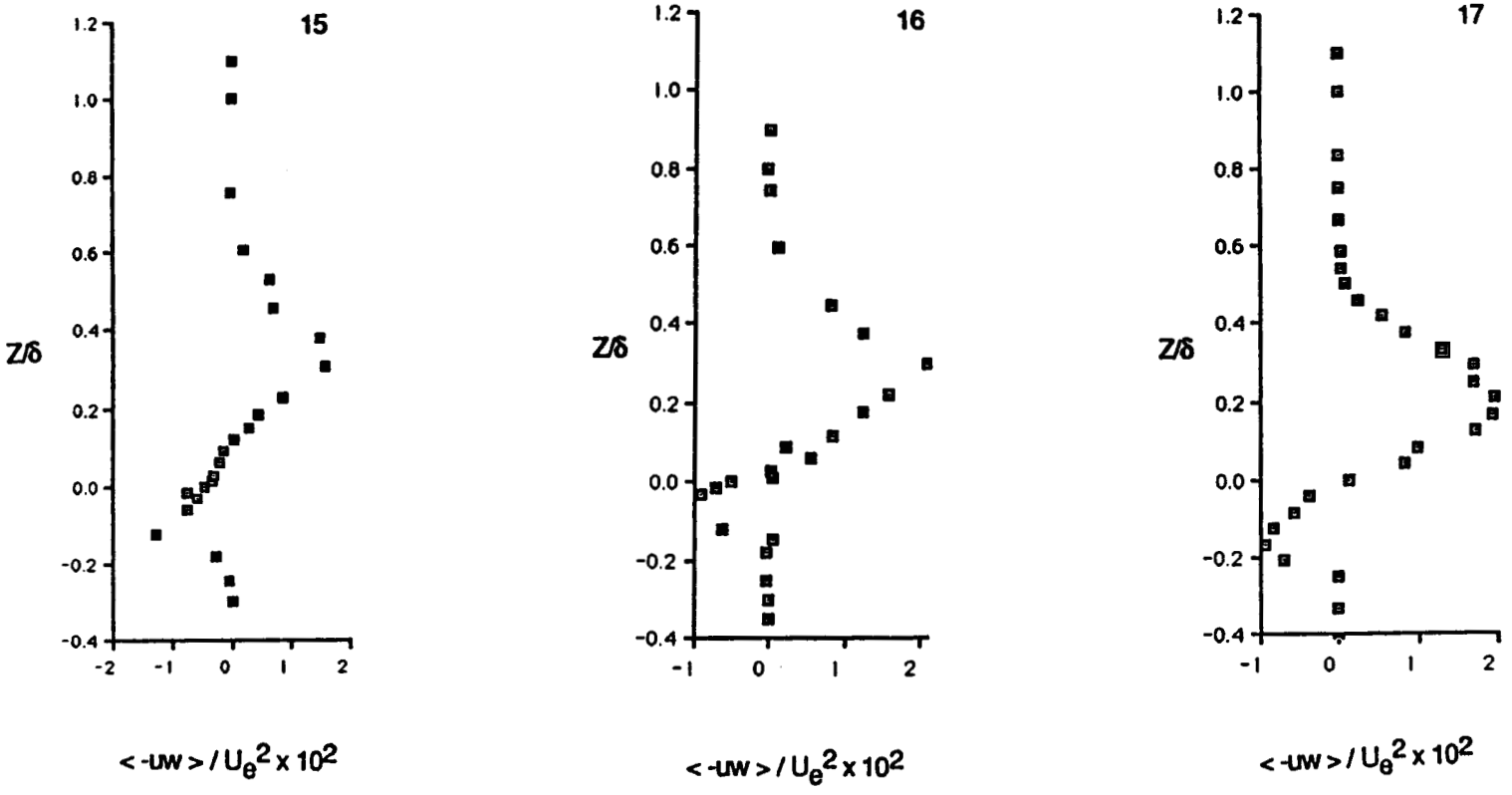

Figure 23.- Continued.

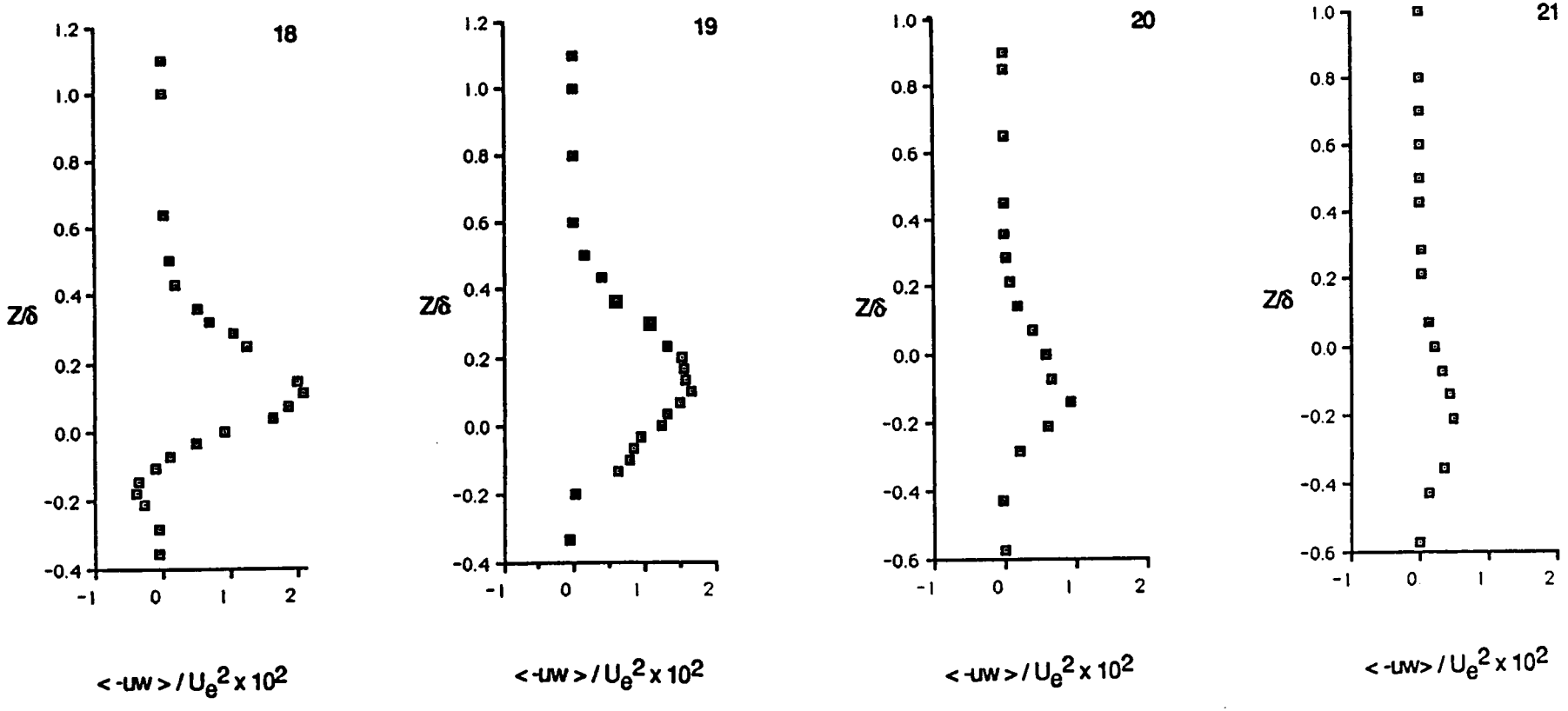

Figure 23.- Concluded.

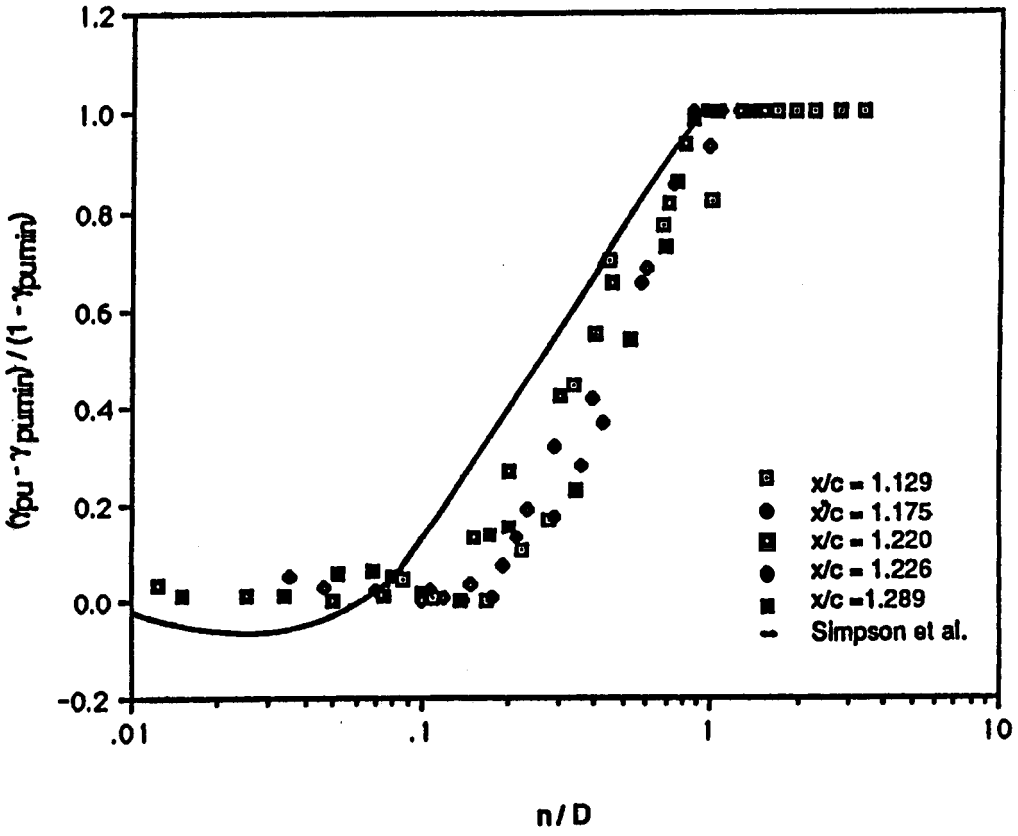

Figure 24.- $(\gamma_{pu} - \gamma_{pumin})/(1 - \gamma_{pumin})$ vs. n/D.

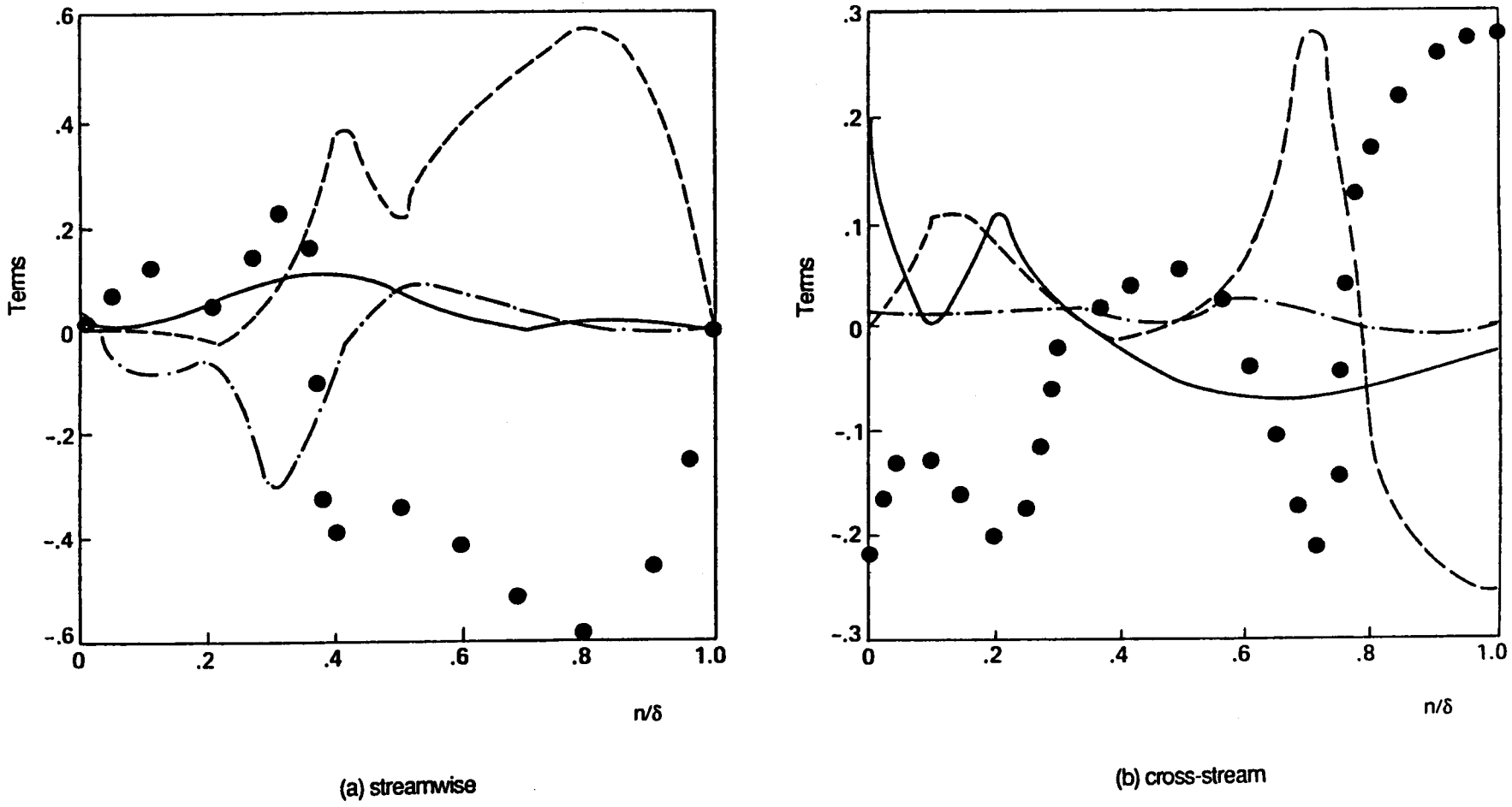

Figure 25.- Terms in the momentum equations at x/c = 1.22 (see key in Table 3).

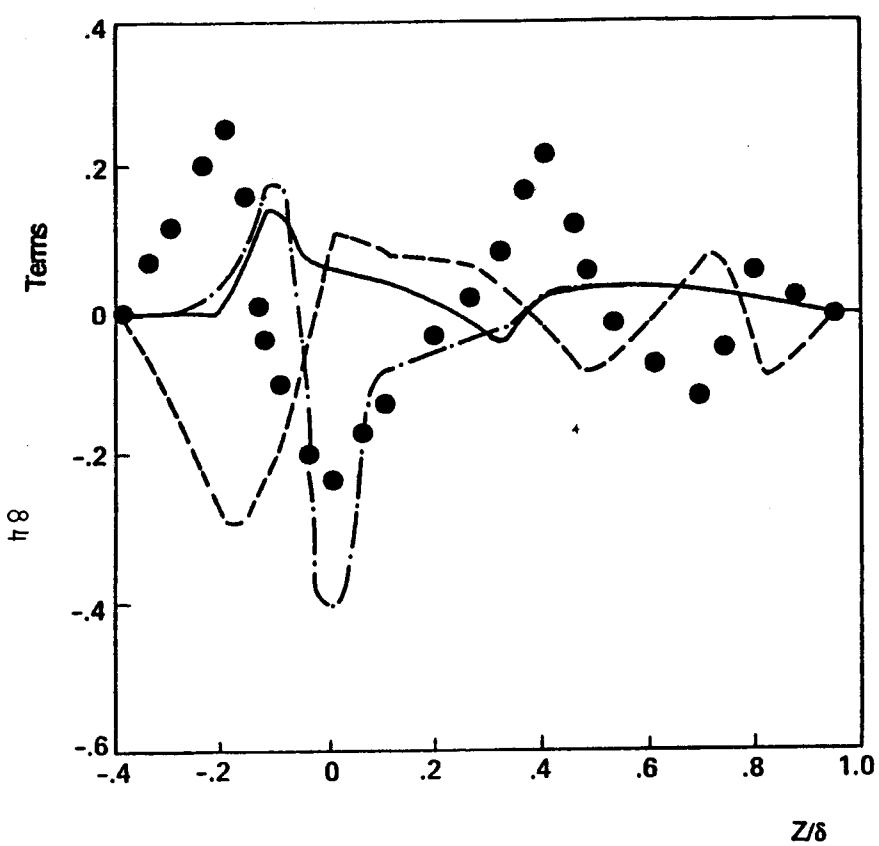

(a) streamwise

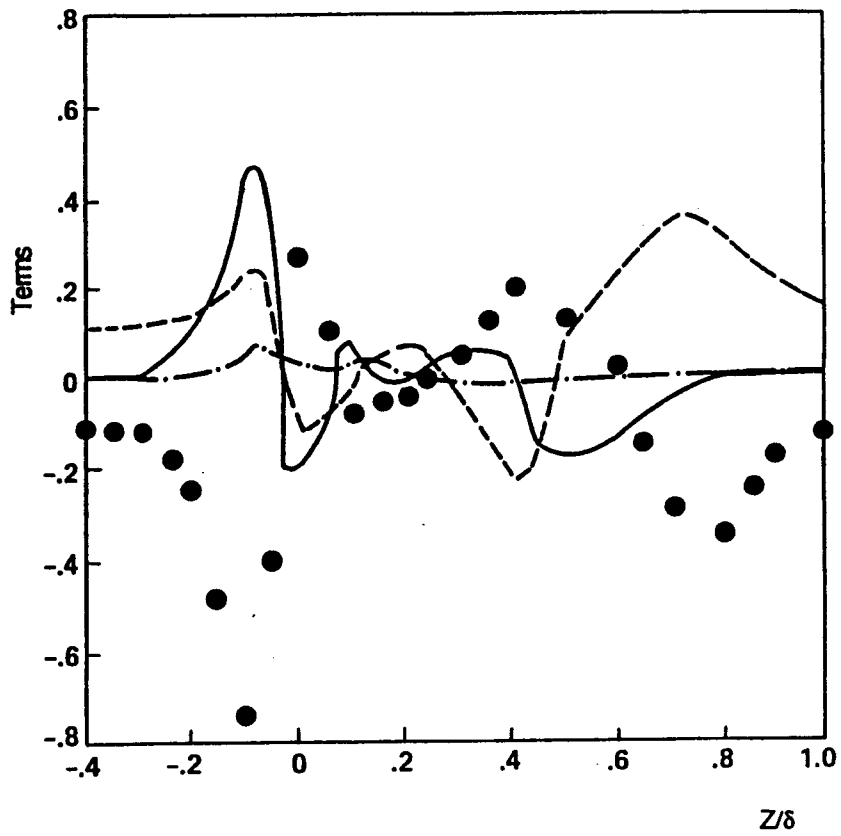

(b) cross-stream

Figure 26.- Terms in the momentum equations at x/c = 1.372 (see key in Table 3).

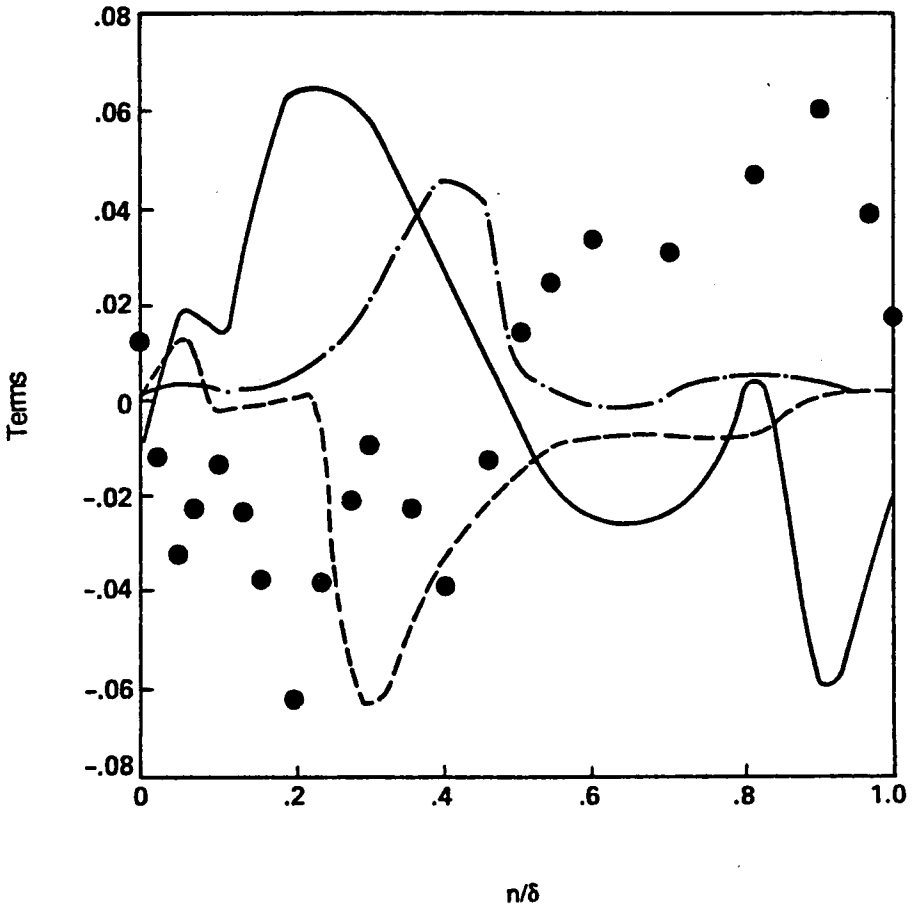

(a) x/c = 1.22.

Figure 27.- Terms in the transport equation for turbulence kinetic energy.

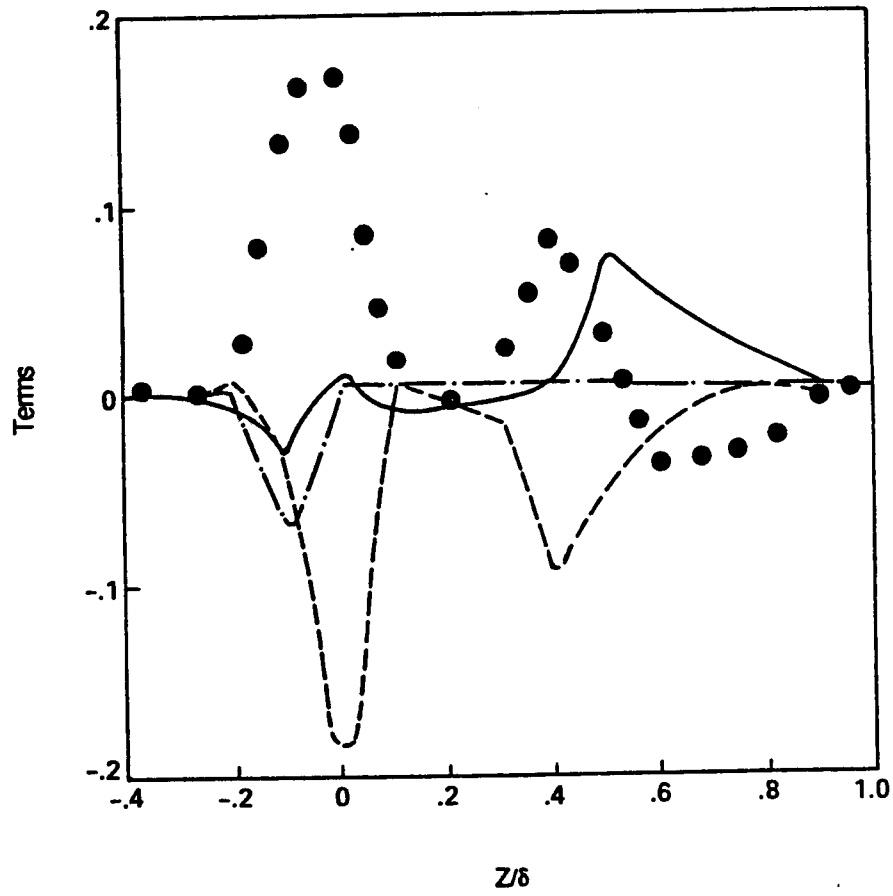

(b) x/c = 1.372.

Figure 27.- Concluded.

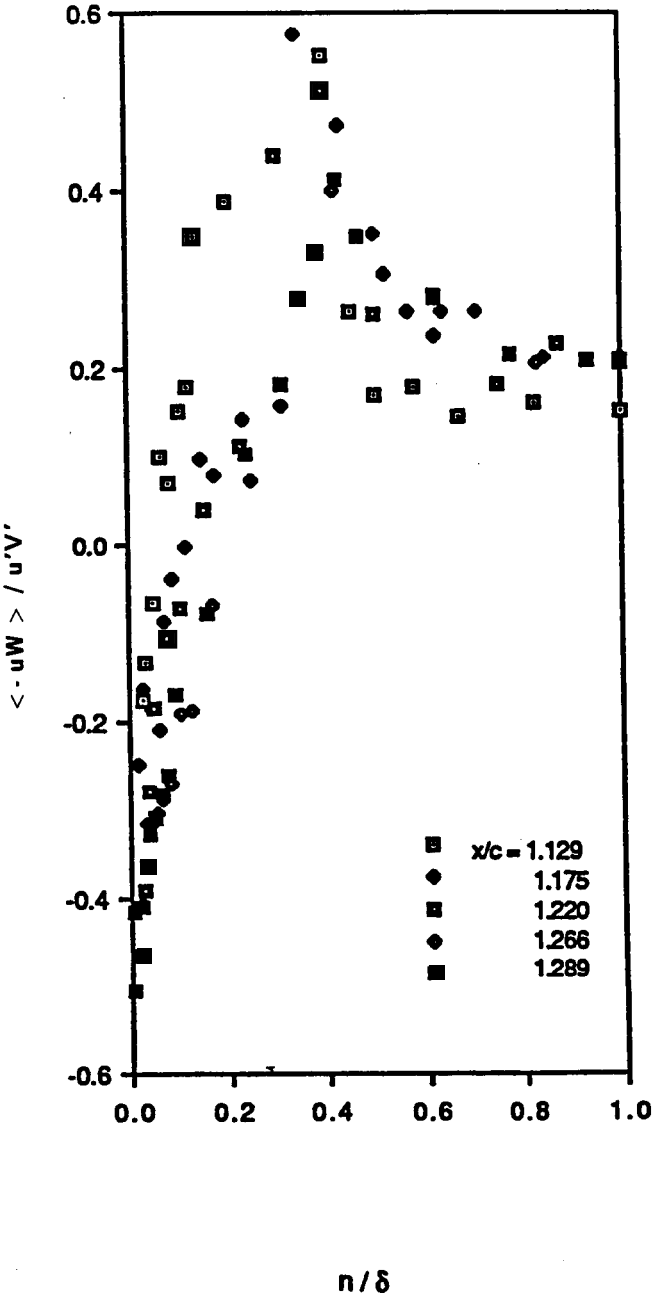

Figure 28.- Shear correlation coefficient.

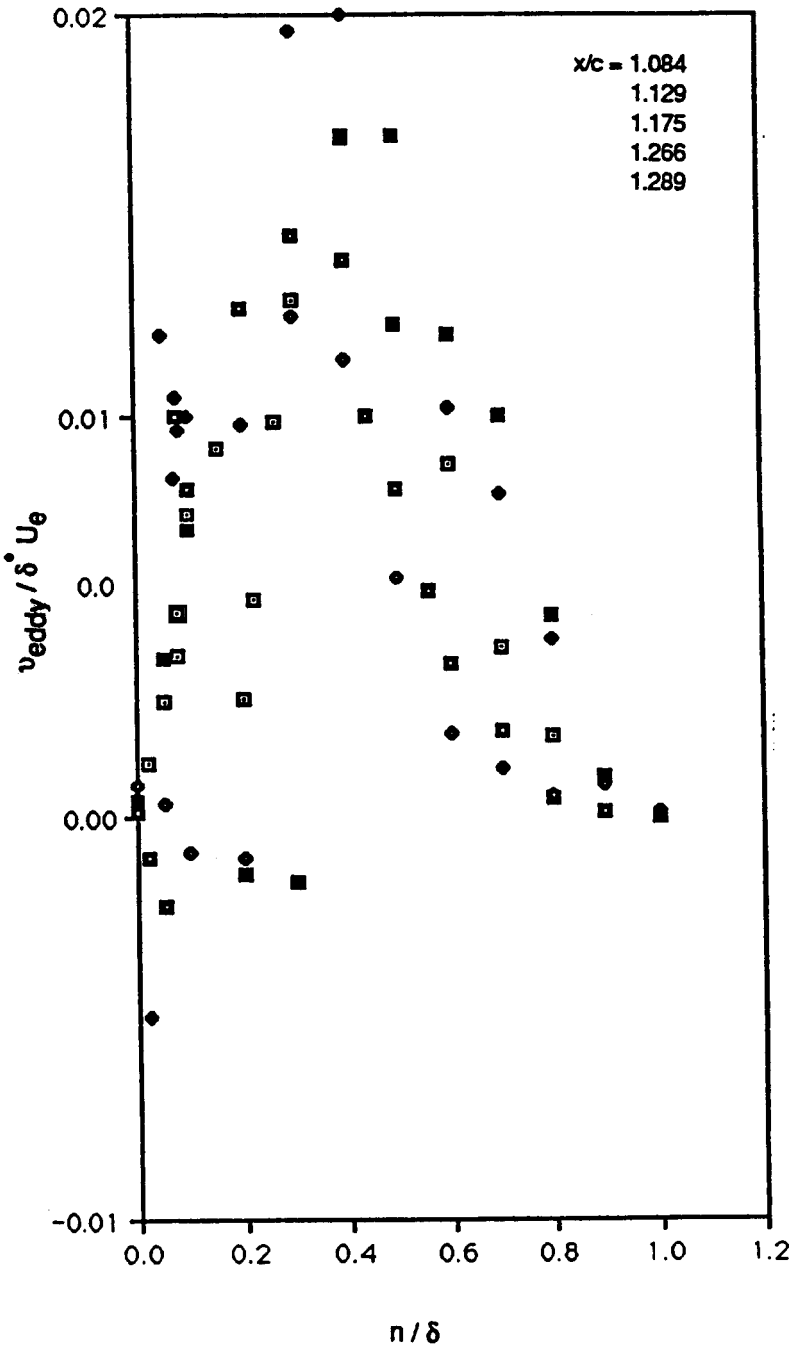

Figure 29.- Profiles of eddy viscosity.

NASA National Aeronautics and Space Administration

Report Documentation Page

1. Report No.	2. Government Accession No.	3. Recipient's Catalog No.
NASA TM-100046		

4. Title and Subtitle
Characteristics of a Separating Confluent Boundary Layer and the Downstream Wake

5. Report Date
December 1987

6. Performing Organization Code

7. Author(s)
Desmond Adair* and W. Clifton Horne

8. Performing Organization Report No.
A-88034

10. Work Unit No.
505-60-11

9. Performing Organization Name and Address
Ames Research Center
Moffett Field, CA 94035

11. Contract or Grant No.

13. Type of Report and Period Covered
Technical Memorandum

12. Sponsoring Agency Name and Address
National Aeronautics and Space Administration
Washington, DC 20546-0001

14. Sponsoring Agency Code

15. Supplementary Notes
*NRC Associate

Point of Contact: Desmond Adair, Ames Research Center, MS 247-2, Moffett Field, CA 94035
(415) 694-5038 or FTS 464-5038

16. Abstract

Detailed measurements of pressure and velocity characteristics are presented and analyzed for flow over and downstream of a NACA 4412 airfoil equipped with a NACA 4415 single-slotted flap at high angle of attack and close to maximum lift. The flow remained attached over the main element while a large region of recirculating flow occurred over the aft 61% of the flap. The airfoil configuration was tested at a Mach number of 0.09 and a chord Reynolds number of 1.8×10^6 in the NASA Ames Research Center 7- by 10-Foot Wind Tunnel. Measurements of mean and fluctuating velocities were obtained in regions of recirculation and high turbulence intensity using 3-D laser velocimetry. In regions where the flow had a preferred direction and relatively low turbulence intensity, hot-wire anemometry was used. Emphasis was placed on obtaining characteristics in the confluent boundary layer, the region of recirculating flow, and in the downstream wake. Surface pressure measurements were made on the main airfoil, flap, wind tunnel roof and wind tunnel floor. It is thought likely that because the model is large when compared to the wind tunnel cross section, the wind tunnel floor and ceiling interference should be taken into account when the flow field is calculated.

In addition to the presentation of pressure and velocity characteristics, the near-wall results inside the separated region are analyzed as are the relative importance of terms in the momentum and turbulence kinetic energy equations in the confluent separated boundary layer and the recirculating region of the near wake.

17. Key Words (Suggested by Author(s))	18. Distribution Statement
Separating confluent boundary layer Multi-element airfoil 3-D laser velocimeter	Unclassified - Unlimited Subject category - 34

19. Security Classif. (of this report)	20. Security Classif. (of this page)	21. No. of pages	22. Price
Unclassified	Unclassified	90	A05